AD-A089 520 HARVARD UNIV CAMBRIDGE MA DIV OF APPLIED SCIENCES F/G 9/3
NONEQUILIBRIUM SUPERCONDUCTIVITY IN OPTICALLY ILLUMINATED TUNNE--ETC(U)
AUG 80 A D SMITH N00014-77-C-0085
UNCLASSIFIED TR-17 NL

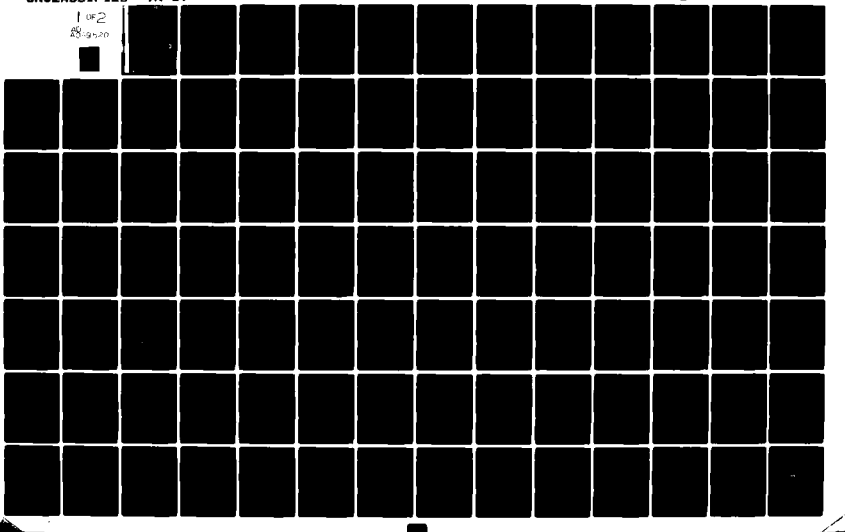

LEVEL II

B.S.

12

Office of Naval Research
Contract N00014-77-C-0085 NR-318-003
Contract N00014-75-C-0648 NR-372-012
National Science Foundation Grant DMR79-04155

NONEQUILIBRIUM SUPERCONDUCTIVITY IN OPTICALLY ILLUMINATED TUNNEL JUNCTIONS

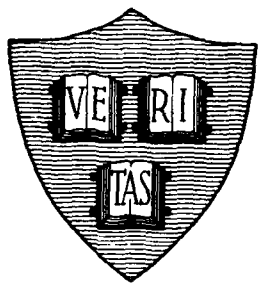

By
Andrew D. Smith

August 1980

Technical Report No. 17

Division of Applied Sciences
Harvard University Cambridge, Massachusetts

Unclassified

SECURITY CLASSIFICATION OF THIS PAGE (When Data Entered)

REPORT DOCUMENTATION PAGE		READ INSTRUCTIONS BEFORE COMPLETING FORM
1. REPORT NUMBER Technical Report No. 17	2. GOVT ACCESSION NO. AD-A089	3. RECIPIENT'S CATALOG NUMBER 520
4. TITLE (and Subtitle) NONEQUILIBRIUM SUPERCONDUCTIVITY IN OPTICALLY ILLUMINATED TUNNEL JUNCTIONS		5. TYPE OF REPORT & PERIOD COVERED Interim Report 6. PERFORMING ORG. REPORT NUMBER
7. AUTHOR(s) Andrew D. Smith		8. CONTRACT OR GRANT NUMBER(s) N00014-77-C-0085, N00014-75-C-0648, NSF DMR79-04155
9. PERFORMING ORGANIZATION NAME AND ADDRESS Division of Applied Sciences Harvard University Cambridge, Mass. 02138		10. PROGRAM ELEMENT, PROJECT, TASK AREA & WORK UNIT NUMBERS
11. CONTROLLING OFFICE NAME AND ADDRESS		12. REPORT DATE August 1980 13. NUMBER OF PAGES 139
14. MONITORING AGENCY NAME & ADDRESS(if different from Controlling Office)		15. SECURITY CLASS. (of this report) Unclassified 15a. DECLASSIFICATION/DOWNGRADING SCHEDULE

16. DISTRIBUTION STATEMENT (of this Report)

Reproduction in whole or in part is permitted for any purpose of the United States Government. Approved for public release; distribution unlimited.

17. DISTRIBUTION STATEMENT (of the abstract entered in Block 20, if different from Report)

18. SUPPLEMENTARY NOTES

19. KEY WORDS (Continue on reverse side if necessary and identify by block number)

Nonequilibrium Superconductivity
Thermoelectric Current
SQUID Circuit
Fiber Optics

20. ABSTRACT (Continue on reverse side if necessary and identify by block number)

Results of a series of experiments on optically illuminated superconducting tunnel junctions are presented. In the first chapters, the question of what non-equilibrium quasiparticle energy distribution results from optical illumination on a thin film is addressed. A new technique using tunneling current-voltage characteristics is developed which accurately measures the nonequilibrium quasiparticle occupation function, f(E). The extremly good resolution of this technique is sufficient to compare the experimental situation to contrasting theoretical models of raised temperature (T*) and shifted electro-chemical

DD FORM 1 JAN 73 1473 EDITION OF 1 NOV 65 IS OBSOLETE
S/N 0102-014-6601

Unclassified

SECURITY CLASSIFICATION OF THIS PAGE (When Data Entered)

20. Abstract continued

potential (μ^*). Data taken on the Al-PbBi tunnel junctions illuminated for this study are well described by the T^* model.

Study of illuminated tunnel junctions lead to the discovery of a new thermoelectric effect for tunneling through oxide barriers between metals at different temperatures. The final chapters are devoted to examination of this thermoelectric effect. Two types of experiments were performed to test for the existence of this effect, with positive results. A self-consistent Rothwarf-Taylor model is presented which correctly predicts the sign, magnitude, temperature dependence and laser-power dependence of the thermoelectric current. The thermoelectric effect described here appears to resolve long-standing discrepancies between experimental results and theoretical predictions for a series of point contact experiments.

Office of Naval Research

(13) Contract N00014-77-C-0085, NR-318-003
Contract N00014-75-C-0648 NR-372-012
National Science Foundation Grant DMR79-04155

(6)

NONEQUILIBRIUM SUPERCONDUCTIVITY IN OPTICALLY ILLUMINATED TUNNEL JUNCTIONS,

By

(10) Andrew D. Smith

(12) 139

(9) Technical Report, No. 17

(14) TR-17

(11) August 1980

The research reported in this document was made possible through support extended the Division of Applied Sciences, Harvard University, by the Office of Naval Research, under Contract N00014-77-C-0085, Contract N00014-75-C-0648 and by the National Science Foundation under Grant DMR79-04155.

Division of Applied Sciences

Harvard University · Cambridge, Massachusetts

ABSTRACT

Results of a series of experiments on optically illuminated superconducting tunnel junctions are presented. In the first chapters, the question of what nonequilibrium quasiparticle energy distribution results from optical illumination on a thin film is addressed. A new technique using tunneling current-voltage characteristics is developed which accurately measures the nonequilibrium quasiparticle occupation function, f(E). The extremely good resolution of this technique is sufficient to compare the experimental situation to contrasting theoretical models of raised temperature (T^*) and shifted electro-chemical potential (μ^*). Data taken on the Al-PbBi tunnel junctions illuminated for this study are well described by the T^* model.

Study of illuminated tunnel junctions lead to the discovery of a new thermoelectric effect for tunneling through oxide barriers between metals at different temperatures. The final chapters are devoted to examination of this thermoelectric effect. Two types of experiments were performed to test for the existence of this effect, with positive results. A self-consistent Rothwarf-Taylor model is presented which correctly predicts the sign, magnitude, temperature dependence and laser-power dependence of the thermoelectric current. The thermoelectric effect described here appears to resolve long-standing discrepencies between experimental results and theoretical predictions for a series of point contact experiments.

TABLE OF CONTENTS

LIST OF FIGURES

LIST OF TABLES

I. INTRODUCTION

Considerable experimental and theoretical effort has been spent studying the nonequilibrium quasiparticle state produced by an external pair breaking mechanism (Aronov and Spivak, 1978; Langenberg, 1974; Langenberg, 1975). Energy externally applied to a superconducting film, such as by optical illumination, perturbs the occupation of quasiparticle states from the equilibrium values set by the Fermi function $f(E) = (1 + e^{E/kT})^{-1}$. Although the actual distribution may be arbitrarily complex, it is tempting to see whether it can be described by a limited number of easily interpreted parameters. In an early attempt to describe nonequilibrium states, Owen and Scalapino (1972) introduced a μ^* model. They argued that emission and absorption of low energy phonons eventually would allow the quasiparticle distribution to acquire the temperature of the phonon bath, while a slower recombination rate would pose a bottleneck, causing a buildup in number of quasiparticles which could be taken into account by a shift in the effective chemical potential: $f(E) = (1 + e^{(E-\mu^*)/kT})^{-1}$. The μ^* model is most applicable for weak perturbation at low temperatures, where very few quasiparticles are excited and hence recombination is slow. Parker (1975) subsequently showed that several nonequilibrium effects could be explained with a T^* model. This model should be valid for those cases where thermalization by the low energy phonons is the slowest step, so that recombination and pair breaking by recombination phonons dominate the energy relaxation. The relatively poor phonon coupling to the low energy phonons may allow

the quasiparticles and high energy phonons to reach some new effective temperature T^* significantly different from the bath temperature. In this case the quasiparticle occupations could be approximated by $f(E) = (1 + e^{E/kT^*})^{-1}$. Of course, one can combine these approaches, using both μ^* and T^* to give a 2-parameter fit to the distribution function. In a less simplistic approach to the problem Chang and Scalapino (1978) succeeded in solving the linearized kinetic equations for different degrees of phonon-to-bath coupling and several special cases of excitation, including one which resembled optical illumination. For poor coupling to the bath, they found their results closely resembled T^*-like distributions.

Quasiparticle tunneling has been used in much of the detailed examination of the validity of the theoretical models. (See Fig. 1.1.) Pioneer work by Parker and Williams (1972) measured the gap reduction under optical illumination, which they interpreted in terms of μ^*. Hu et al. (1974) were able to actually observe the dynamic relaxation in the number of quasiparticles by observing the time dependence of the quasiparticle tunneling current after pulsing a film with a laser. They succeeded in measuring the quasiparticle relaxation time for tin but did not find evidence of a first-order phase transition to the normal state as was predicted within the μ^* model.

This work will discuss two topics related to illuminated superconducting tunnel junctions. A new method for using asymmetric

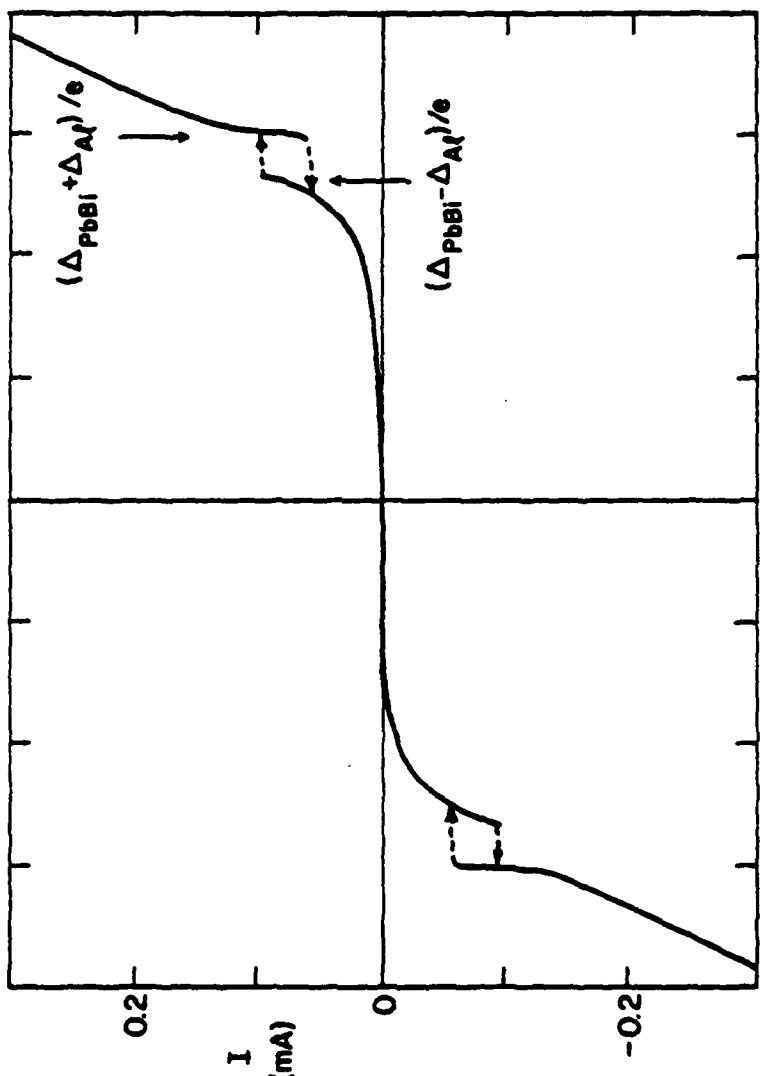

FIGURE 1.1. I(V) for an Al-PbBi tunnel junction at 2.08 K. Dashed lines indicate hysteretic voltage jumps. The current is roughly exponential at small voltages.

tunnel junctions as a sensitive and accurate probe of the superconducting state will be presented and will be applied to experimental results for optically illuminated aluminum-aluminum oxide-lead bismuth (Al-PbBi) tunnel junctions. Results tend to confirm the validity of the T^* model to describe the nonequilibrium quasiparticle occupation function in the system.

Also presented will be the discovery of a new thermoelectric effect in tunnel junctions. Experimental observations confirm the existence of a thermoelectric current present through tunneling barriers between metals at different temperatures. The existence of this thermoelectric effect can explain puzzling discrepencies between experimental results and theoretical predictions in several earlier superconducting thermopower experiments.

II. EXPERIMENTAL TECHNIQUES

Accurate unfolding of quasiparticle I(V) curves to obtain occupation numbers required development of a number of techniques new to our laboratory. First, a method for successfully making tunnel junctions had to be found which would work with the available equipment. The tunnel junctions had to display very sharp gap structures and have reasonable resistances. Sections A and B describe the methods I used to fabricate high quality tunnel junctions reproducably. Second, the I(V) characteristics must be taken with sufficiently high accuracy that input noise would not make the output occupation numbers meaningless. It was quickly determined that taking data from XY plots of I(V) was both tedious and insufficiently accurate. Sections C and D describe a microcomputer-based system I designed and built to control and monitor the laser illumination experiments. Finally, section E provides details on thermometry techniques.

A. Substrate Cleaning Procedure

For the results reported here, polished single crystal sapphire substrates 1 X 1/4 X 0.025" in size were obtained from Adolph Meller Co. The substrates were each recycled many times. Careful cleaning of the substrates was found to be essential for making uniform metal films. The substrate cleaning procedure given below evolved from a trial-and-many-errors search for a method of obtaining consistent film

quality.

1. Used substrates were placed in a beaker of distilled water. Potassium hydroxide (KOH) flakes were added to just cover the substrates. The KOH dissolved away metal films and loosened indium dots from earlier sample junctions. Stirring once or twice over a half hour period usually was sufficient to clean off the substrates, otherwise this step was repeated.

2. The substrates were rinsed thoroughly with distilled water.

3. The substrates were put in a 2 percent solution of "Micro" cleaner (manufactured by International Products Corp.) which was then brought to a boil over a Bunsen burner. Heating the solution served to speed up the degreasing action. The hot mixture was then ultrasonically agitated for a minute.

4. The samples were again thoroughly rinsed in distilled water, this time with ultrasonic agitation.

5. The substrates were allowed to dry in air under a Tensor lamp. The substrates could then be stored until needed.

B. Tunnel Junction Fabrication

Three substrates at a time were mounted on the bottom of a copper block within the evaporator. The substrates were held in position with small dabs of Apiezon M high vacuum grease. The substrates were then covered with a masking plate which defined an exposure pattern for the bottom metal layer. The evaporator was next sealed and evacuated to $< 10^{-5}$ Torr. To prevent diffusion pump oil backstreaming into the evaporator, care was taken to be sure that the liquid nitrogen coldtrap was always filled.

To make the dirty aluminum layer, it was necessary to incorporate large amounts of oxygen into the aluminum during evaporation. Following a suggestion by Kaplan, evaporation boats of Mo overcoated with alumina (Al_2O_3) were used to hold the aluminum pellets to be evaporated. As the boat was heated, it outgassed oxygen in addition to evaporating aluminum from the pellets. The chamber pressure, as measured by an ion gauge above the coldtrap, would rise to $3\text{-}9 \times 10^{-5}$ Torr during evaporation. T_c's of the films made in this manner ranged from 1.6 to 2.3 K.

The next step in making the tunnel junctions was to grow an oxide barrier layer on the aluminum. Barriers formed in air at one atmosphere pressure formed junctions with resistance too high to be useable ($1\ k\Omega\ mm^2$). To obtain lower resistance junctions, a small dead space in

the air release line was backfilled with oxygen gas to 3 psig (980 Torr). When this controlled volume of gas was released into the chamber, a pressure of 0.1 Torr resulted. This gas was subsequently pumped out after a period of 15 seconds to 2 minutes.

The masks were changed without breaking vacuum by using a mechanical feedthrough to slide the masking plate, aligning a second set of masks. After evacuation of the chamber to 10^{-5} Torr again, a $Pb_{0.95}Bi_{0.05}$ layer was evaporated to complete the tunnel junctions. Figure 2.1 shows the metal pattern of a completed junction. Each substrate contained three cross-strip tunnel junctions. The bottom aluminum strip was common to all three junctions. A total of eight contacts were made at the edge of the substrate to be able to make four-terminal I(V) measurements on the tunnel junctions.

For optical illumination studies, it was desirable to be able to illuminate the tunnel junction from both sides of the substrate. The design of the subtrate holder used to accomplish this is shown in Fig. 2.2. The substrate was held by a tight fitting recessed area in the bottom block of the substrate holder. A top block was then fastened to the bottom block, completing the holder assembly. Both pieces were made of phenolic. Large central cutout slots permitted optical access. Electrical contacts were made by compressing indium dots (actually cylinders of indium 0.25 mm X 1. mm dia. made by cutting indium wire) between the substrate lead pads and tinned flat posts epoxied into the

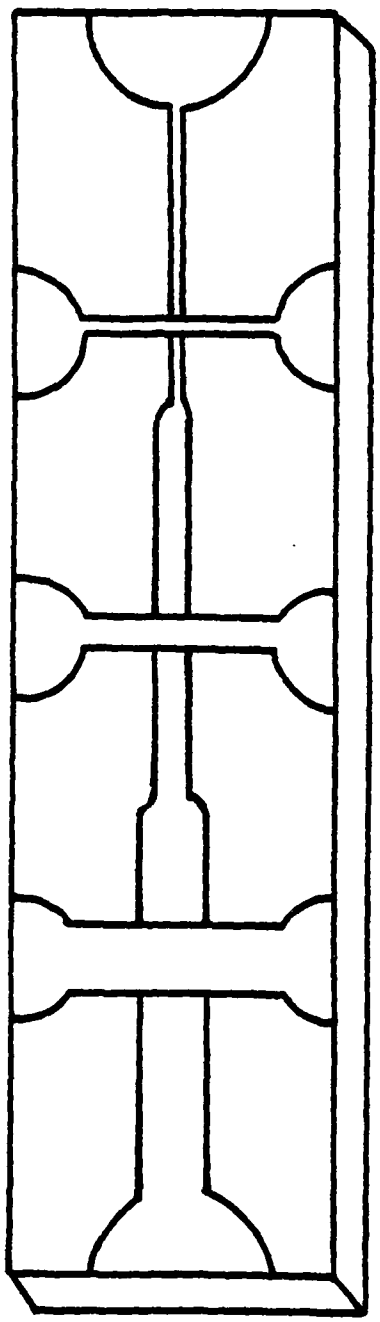

FIGURE 2.1. Tunnel junction layout.

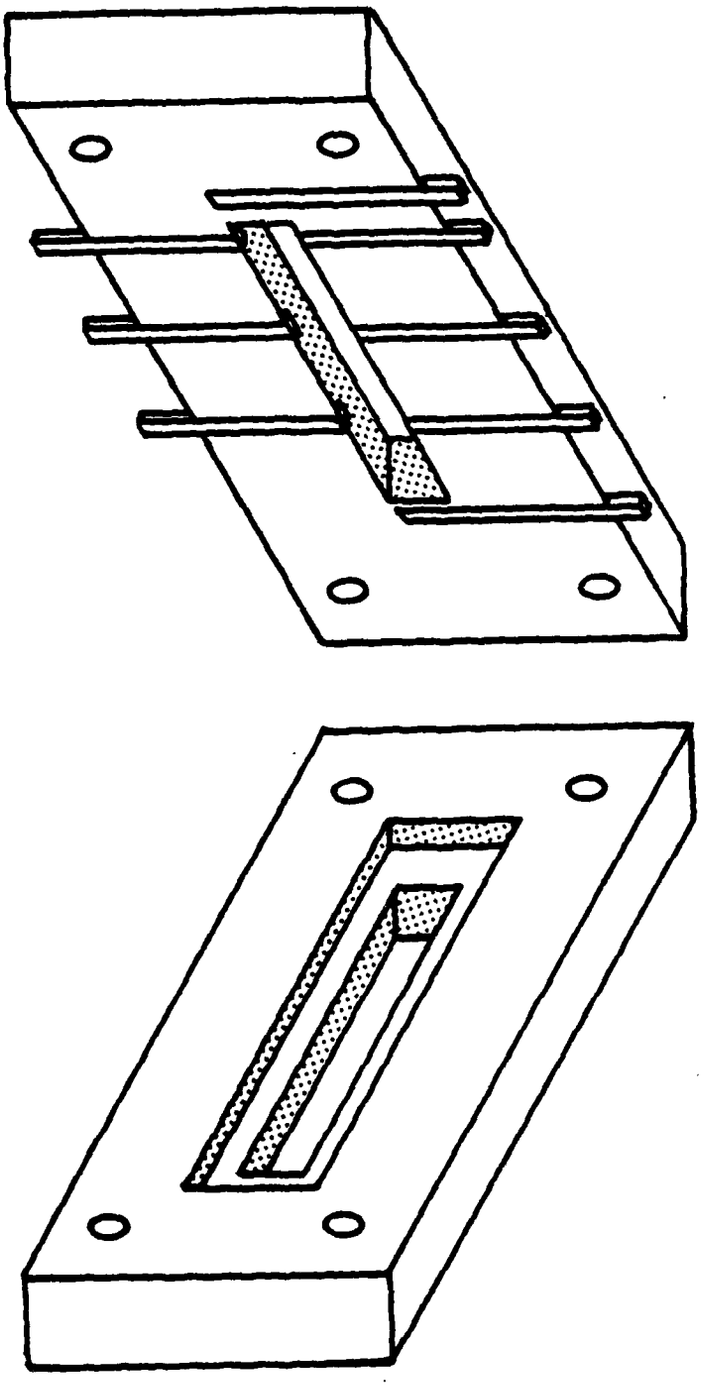

FIGURE 2.2. Substrate holder showing electrical contacts in upper block.

top block of the substrate holder. The indium dot method of making electrical contacts worked without a single failure at low temperatures. An obvious additional advantage of this method over soldering is that heating of the substrate, which can easily damage the junction, is avoided altogether.

C. The Data Acquisition System

After mastering the black arts of tunnel junction fabrication, it quickly became apparent that taking data would be no simple matter. In order to achieve the highest possible sensitivity, a phase synchronous (lock-in) measurement scheme was employed. The laser beam was chopped at 25 or 337 Hz, and the synchronous signal was detected and recorded. For constant current biasing the observed shift in voltage would typically amount to only a few μV. It was necessary to accurately record I(V) and dV(V). The dV(V) measurements had to be converted back to dI(V) by dividing by the dynamic impedance of the tunnel junction. Carrying out all of these calculations for the hundred or so data points needed to do inversion turned out to be very difficult to do by hand.

To improve upon our conventional XY recorder, pen-and-paper data recording, digital technology was called upon. The main objective was to build a data acquisition machine which could record data with high accuracy, good resolution, and very low noise. The system had to

simultaneously monitor and record voltage signals from voltage amplifiers, lock-in amplifiers, ammeters and thermometers. In addition, it was desirable that the system adapt readily to modifications in the design of the experiments.

After studying the available prepackaged data acquisition systems, it was decided that the most cost effective and versatile data acquisition system could be built by designing around a microcomputer.

The microcomputer system built centers around the Digital Equipment Corporation (DEC) LSI-11/2 family of components. The microcomputer consisted of a backplane, CPU, memory, disk system, and serial input/output, shown schematically in Fig 2.3. The backplane is the chassis which electrically connects the various individual printed circuit boards. In order to allow maximum room for additions and adaptations, an especially large backplane (DEC DDV11-B) was modified to conform to the LSI-11/2 wiring scheme. The backplane has room for 18 cards connected onto the central data bus, plus additional space for 9 more cards which can be wired individually.

The microcomputer is controlled by a central processing unit (CPU) capable of manipulating 16 bit long "words" of data or instructions. The CPU card handles memory access and manipulates the available data coming from teletype units and other input/output devices. The main memory storage is supplied on a 28K (1K = 1024) word semiconductor memory card.

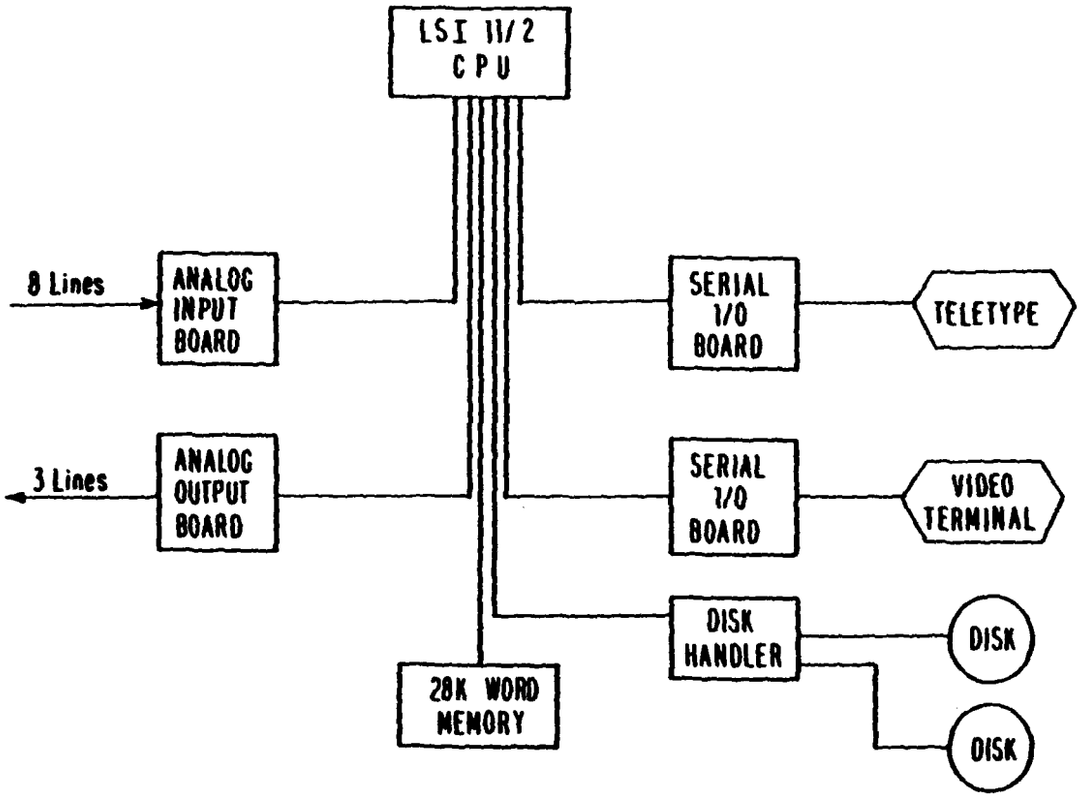

FIGURE 2.3. Block diagram of LSI-11/2 microcomputer system.

More permanent storage of data and programs is done on double density floppy magnetic disks, each capable of holding 1/4 million words of data or program information. The Charles River dual drive disk unit consists of two separate read/write stations, plus its own dedicated microprocessor which maintains an orderly file structure and checks for read errors. The computer can edit, compile and run standard FORTRAN language programs, as well as use its own, somewhat more efficient MACRO assembly language. The versatility and ease of use of the computer is best evidenced by the number of group members who compete for time on the machine to take data, run time-consuming theoretical calculations, or edit manuscripts.

The ability for the microprocessor to read analog signals from amplifiers, DVMs, lock-ins, etc. is provided by incorporation of an Analog Devices RTI-1250S analog-to-digital (A/D) input board. The computer accesses the board as if it were a memory location. Under program control, the A/D board selects any of eight input lines, samples the voltage on that line, converts the -10 V to 10 V input to a 12 bit integer, and presents that digital information to the CPU. For added resolution for small signals, a programmable gain amplifier (PGA), with computer selectable gains of 1,2,4, or 8, is included in the A/D circuit. The PGA can be used to increase the sensitivity of the A/D, at the cost of decreasing the input voltage range. Although the maximum accuracy of the converter remains fixed at 2^{-11} (0.05 percent) of the full scale

reading, the resolution can be set as low as 0.5 mV by using the PGA. In order to increase the sensitivity still further, two of the analog input lines are connected to special low drift, high impedance amplifiers (Analog Devices 522B) which are wired to provide a switch-selectable gain of 1, 10, 100, or 1000. All of the analog inputs are differential-input, so that "ground" connections for analog lines coming to the computer are actually measured as separate voltages and are automatically subtracted from the signal. In this manner potential ground loops through the computer are avoided and line pickup along the cables is eliminated as a problem.

Complementing the A/D board, an Analog Devices RTI-1252 digital-to-analog (D/A) board provides analog output from the computer. Each of three memory locations can be used to set a corresponding D/A converter to any voltage between -10 V and 10 V with ~5 mV resolution. The D/A features are useful in controlling repetitive tasks during the course of the experiment, such as adjusting the current through the tunnel junction.

To reduce 60 Hz noise, the dc power for the computer and support circuitry is regulated to have very low line ripple (measured as 0.001 V which is quite small compared to the 0.5 V ripple typical of DEC power supplies). The power supply was shielded and located away from the sensitive analog circuits.

D. Experimental Setup

The overall system schematic is shown in Fig. 2.4. The current was set by applying a known voltage through a large resistance (10 kΩ to 10 MΩ depending on the junction resistance and the desired bias point). The current was measured by sensing the voltage across the standard resistor with a high impedance isolation amplifier, which then fed into one of the computer A/D inputs. The voltage across the illuminated tunnel junction was amplified with a PAR 113 preamplifier and then sent to another A/D input. The recorded current voltage characteristics for an Al-PbBi tunnel junction is shown plotted in Fig. 2.5. The large range in measured currents (which reflects the exponential voltage dependent conductance) was obtained by changing the bias resistor and taking the curve piecewise. Resolution of the current measurements is better than one nanoampere.

Two lock-in amplifiers were used to record both phases of the laser-induced voltage shifts across the current biased tunnel junction. Junction capacitance introduced some phase shift and attenuation into measurements of the laser-induced dV. Fig 2.6 shows a simple electrical model for the tunnel junction and measuring circuitry. The effect of laser illumination is similar to that of an external current generator which would add a current, $dI^{L}(V)$, to the junction. For dynamic junction

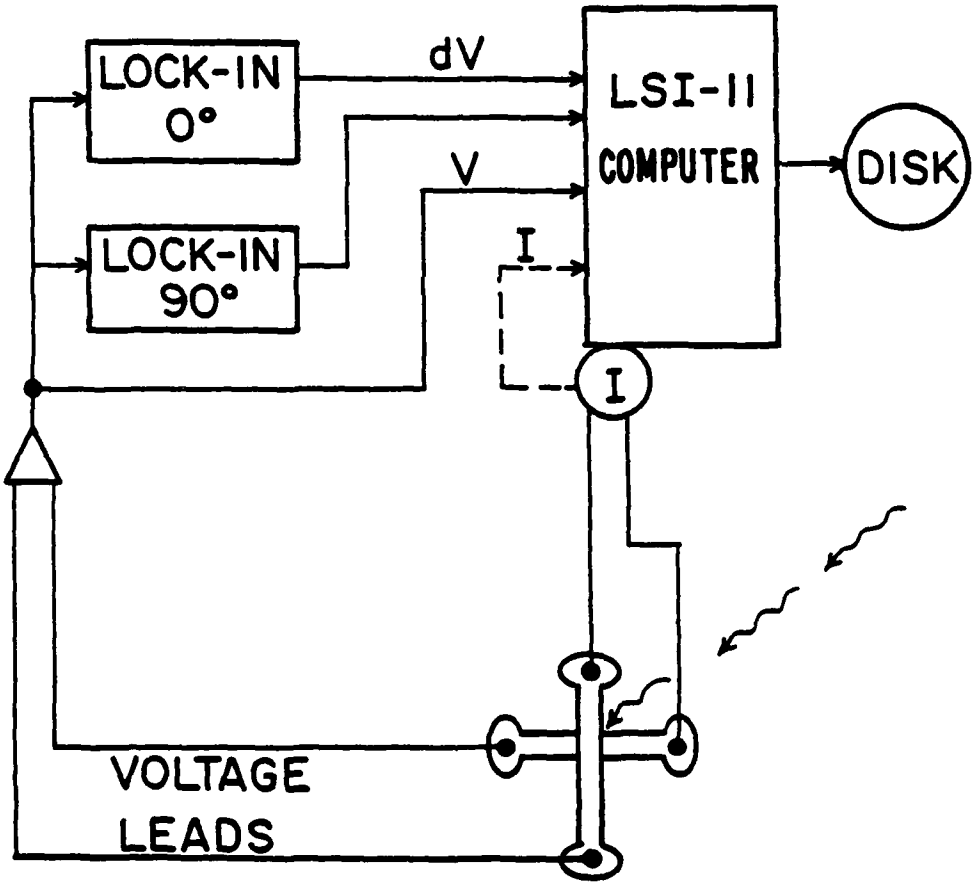

FIGURE 2.4. Schematic diagram of voltage measurement circuit.

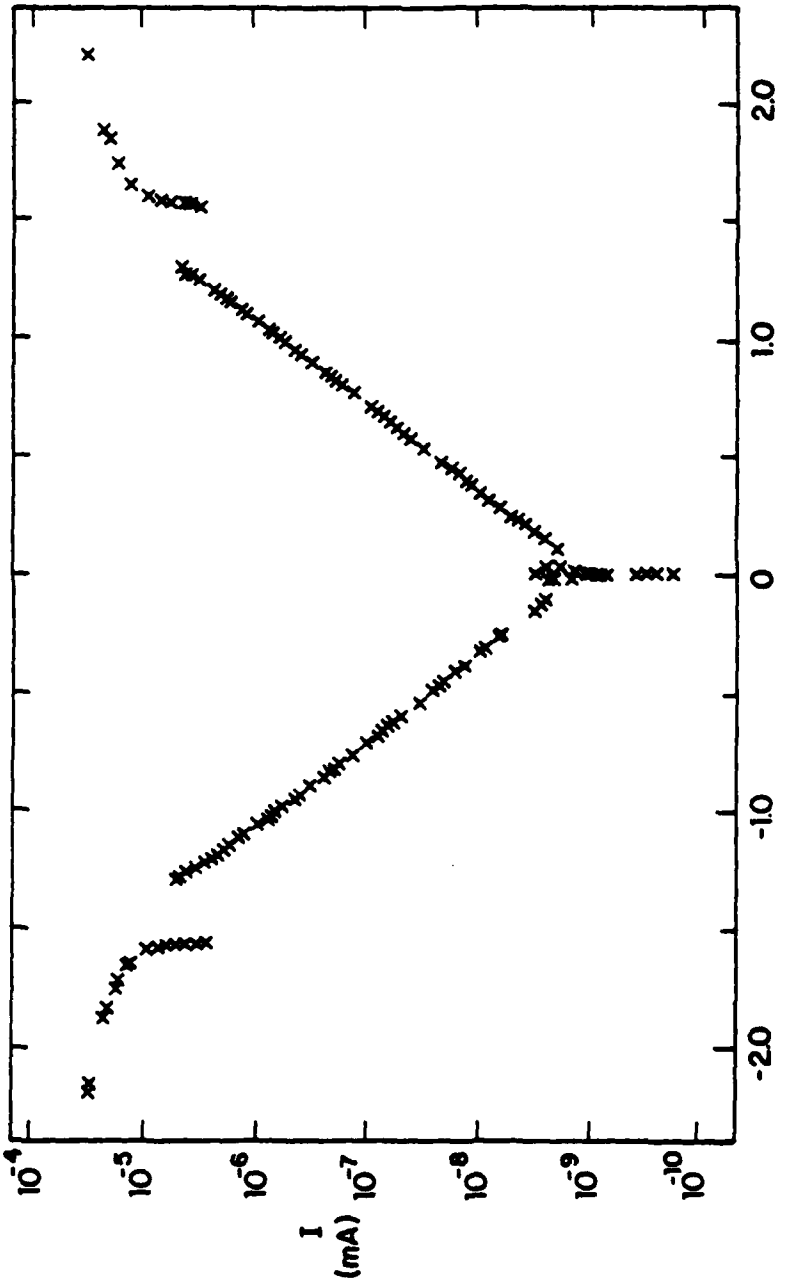

FIGURE 2.5. Measured I(V) curve for an Al-PbBi tunnel junction at 1.815 K. The data at zero voltage is supercurrent.

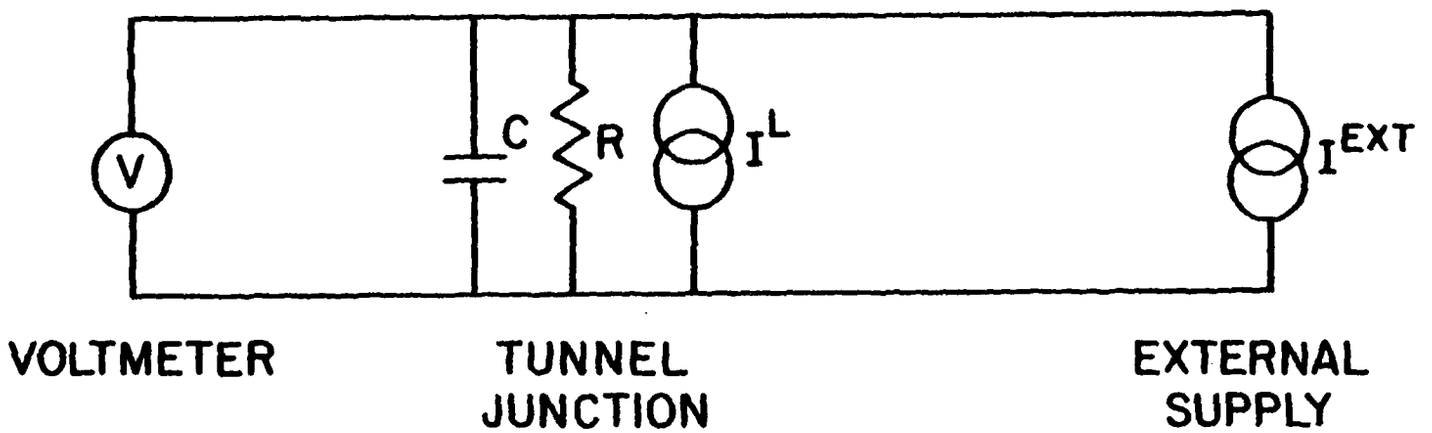

FIGURE 2.6. Electrical model of the tunnel junction including junction capacitance (C) and laser-induced current I^L.

resistance R (voltage dependent), the observed output voltage dV(V) is given by

$$dV = dI^{L} R / (1 + i\omega RC) \qquad (2.1)$$

where ω is the 2π times the chop frequency and C is the junction capacitance. The junction capacitance decreases the observed dV signal, especially for large dynamic resistances.

Corrections can be made for capacitive losses if the capacitance is known. Inspecting Eq. (2.1) it can be seen that the observed phase shift angle is given by

$$\tan(\theta) = -\omega RC \qquad (2.2)$$

Fig. 2.7 shows the tangent of the measured phase shift as a function of the dynamic resistance of the tunnel junction for a single tunnel junction at three different temperatures. The straight line fit implies a junction capacitance of 2.4×10^{-8} F. The fit value of the capacitance could then be used with the dynamic resistance computed from the I(V) curve to give a complex impedance, which would finally give the correct dI(V) for a measured dV(V) using Eq. (2.1).

During my sample runs, a FORTRAN program handled signal sampling and setting of parameters. One of the computer's D/A outputs was used to

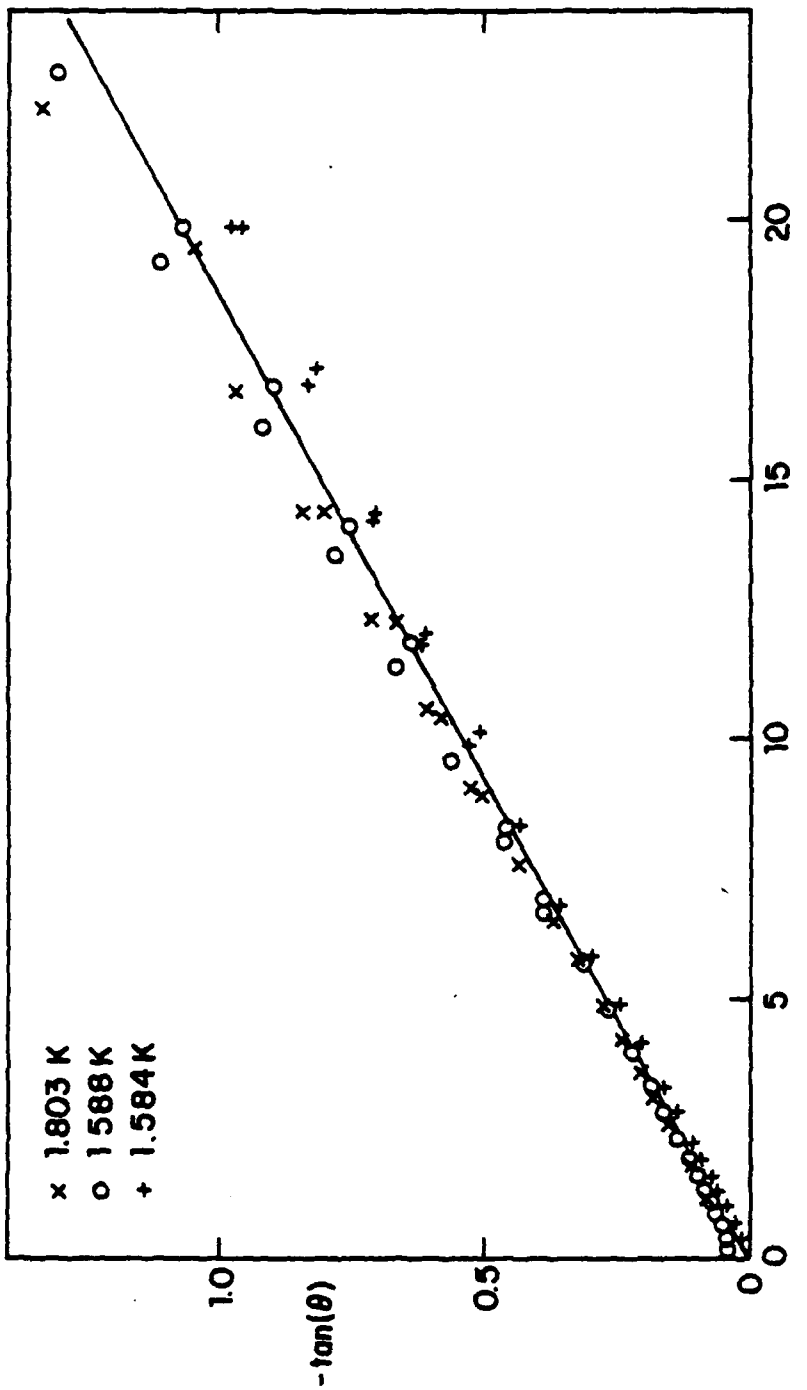

FIGURE 2.7. Observed tangent of the phase shift vs. dV/dI for one tunnel junction at three different temperatures. The straight-line fit is for a capacitance of 2.4×10^{-8} F.

sweep out the I(V) tunneling curves in steps. For each data point, the computer set the current, paused 1/2 second to allow for relaxation of transients in the lock-in amplifiers, and then accumulated and averaged separately measurements of the current, voltage, and dV for the tunnel junction over an averaging period of a second. For each current value, two data points were taken on the upsweep, and another two were taken on the downsweep in order to check for reproducibility (no problem) and hysteresis.

E. Thermometry

To monitor temperatures during precooling of the rig, simple silicon diodes (type 1N4004) proved to be convenient and inexpensive (8 cents apiece) thermometers. Biased in the forward direction at 10 μA, the voltage drop across the diodes were measured with a digital voltmeter (DVM). At room temperature the voltage drop was typically 0.40 V. The voltage increased quite linearly with decreasing temperature, at least down to liquid nitrogen temperature. At liquid nitrogen temperature the voltage drop was typically 1.00 V. The diodes cycled to liquid helium temperatures without failures, and had temperature-voltage characteristics which were quite reproducible.

At liquid helium temperatures the voltage across the diodes would rise to roughly 2.6 V. The 20 μW dissipated by the diode was sufficient

to prevent effective vapor cooling by helium vapors alone. During transfer, only when the diode was covered by liquid helium would the voltage on the diode remain steady. Thus it was a simple matter to use the diodes as level detectors as well as precooling monitors. An added advantage of use of the silicon diodes was that the voltage drops across the diodes were much larger than characteristic thermal emf's or ohmic voltage drops along the leads, so null measurements and four-terminal measurements were both unnecessary.

To measure the exact temperature during data-taking runs, later experiments used a commercial Cryocal CR-1000 calibrated doped germanium resistance thermometer. Care was taken to have the thermometer at the same height as the tunnel junctions and as close as possible to the samples. The bath temperature could be monitored to within a few mK using a Keithley 160 DVM to measure the voltage across the constant current biased germanium element. The DVM analog output was then sampled by the computer, which could convert the measured voltage into a temperature using a lookup table stored in memory.

III. UNFOLDING PROCEDURE

The potential usefulness of tunneling data to determine nonequilibrium occupations was demonstrated by Chang and Scalapino (1976), who calculated tunneling curves for occupation functions which might result from several forms of perturbation. Kaplan et al. (1977), Chang (1977), and Kirtley et al. (1978) subsequently studied hole-like and electron-like injection of quasiparticles in tunnel junctions and compared the observed current to models of branch imbalance to extract relaxation times. In a series of experiments using a double tunnel junction structure, Gray and Willemsen (1978, 1979a, 1979b) unfolded I(V) data to observe significantly nonthermal distributions induced by intense quasiparticle injection. Studying pair breaking tunneling, Balkashin et al. (1979) found non-T* behavior for low intensity illumination of lead tunnel junctions.

Most recently Jaworski and Parker (1979) reported results from optically illuminated symmetric tin tunnel junctions, using a matrix unfolding technique to extract occupation numbers. They were unsuccessful in directly calculating the occupation function, but did perform a multi-parameter fit in powers of 1/E.

This chapter presents an improved method (Smith et al., 1980) for using asymmetric tunnel junctions as a sensitive and accurate probe of the superconducting state.

A. Derivation of Unfolding Technique

Figure 3.1 shows the semiconductor model picture of quasiparticle tunneling in an asymmetric tunnel junction biased at voltage V. For a particular aluminum quasiparticle state with energy E_o, the voltage has been chosen just less than $(\Delta_1 - E_o)/e$. No tunneling from this state is allowed because the quasiparticle would fall into the gap of the other superconductor. (The same is true for the complementary hole-like quasiparticle state on the lower branch with the same energy.) If the voltage is increased just slightly, as shown in figure 3.1b, tunneling will be allowed for the upper branch states.

Algebraically the semiconductor model can be written:

$$I(V) = (1/eR) \int_{-\infty}^{\infty} N_1(E)\, N_2(E+eV)\, [f_1(E) - f_2(E+eV)]\, dE \quad (3.1)$$

(s script 1 referring to the lead bismuth; subscript 2 referring to the aluminum). The effect of the gap in the density of states $N_1(E)$ is such that aluminum quasiparticles of a given energy E will not contribute to the observed current if $eV < \Delta_1 - E$. The sharp onset of tunneling from these states at the voltage $(\Delta_1 - E)/e$ provides the means to recognize the extent to which quasiparticle states of energy E are occupied. Analysis becomes more complex for high energies $(E > \Delta_1)$ because tunneling from these states does not have the same sort of sharp onset as

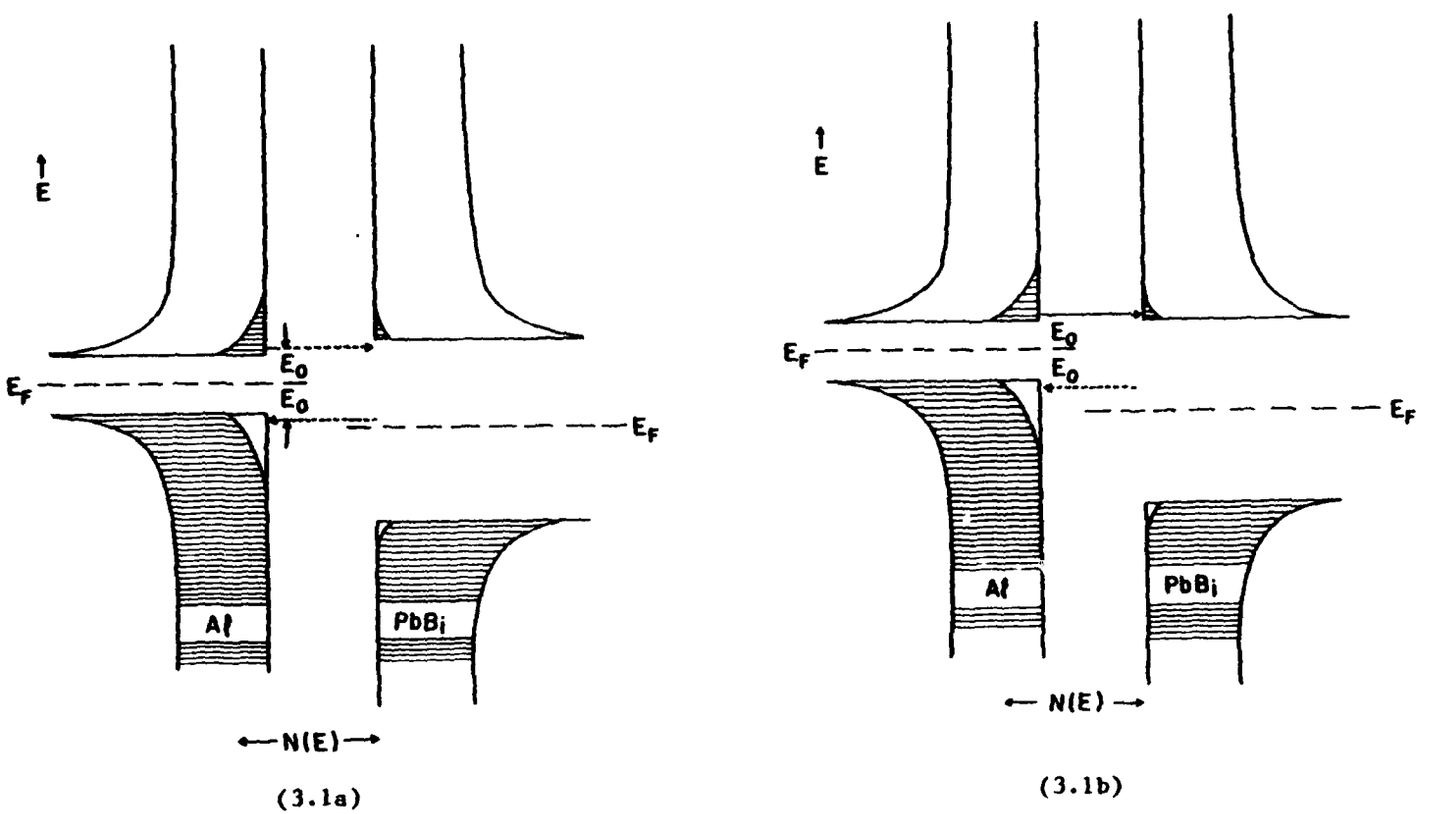

FIGURE 3.1. Semiconductor-model picture of disallowed (3.1a) and allowed (3.1b) tunneling from a state with energy E_o for two slightly different voltages V.

is the case with the lower energy states. Fortunately these highest energy states are sparsely populated at the temperatures of interest and therefore contribute little to observed currents. It is convenient, therefore, to restrict unfolding analysis to calculation of aluminum quasiparticle occupations of states with energy less than Δ_1.

The tunneling equation may be manipulated into a more convenient form for inversion. Since lead bismuth states with $E < \Delta_1$ are nonexistant, it is possible to set $f_1(E) = f_2(E)$ for low energies and to define their common value as $f(E)$. Because the contribution of high energy quasiparticles to the current is insignificant within the stated constraints, it is possible to extend the occupation equality requirement to include higher energies also, with no noticeable error. Tunneling effects due to branch imbalance (Gray and Willemsen, 1979) should be negligible because the optical pair breaking creates essentially the same number of electron-like and hole-like excitations. This allows use of the identity

$$f(E) + f(-E) = 1 \qquad (3.2)$$

to eliminate the dependence on negative energies. Writing equation (3.1) in terms of positive energies, and regrouping, yields:

$$I(V) = (1/eR) \int_0^\infty [N_1(E)N_2(E-eV) - N_1(E-eV)N_2(E) + N_1(E+eV)N_2(E) - N_1(E)N_2(E+eV)]\, f(E)\, dE \quad (3.3)$$

where $N_i(E)$ is defined to be zero for $E < \Delta_i$. Note that for $E < \Delta_1$, and $eV < \Delta_1 - \Delta_2$, only the third term is nonzero. (In order to avoid pair-breaking tunneling, data should be taken only for $V < (\Delta_1 + \Delta_2)/e$. Because biasing problems made measurements for voltages in the negative resistance region $(\Delta_1 - \Delta_2)/e < V < (\Delta_1 + \Delta_2)/e$ impractical, the tighter restriction that $V < (\Delta_1 - \Delta_2)/e$ was actually imposed for the data used for unfolding.) Following the notation of *Jaworski and Parker* (1979), the convolution function G(E,V) may be defined such that

$$I(V) = \int_0^\infty G(E,V)\ f(E)\ dE \quad (3.4)$$

In theory the linear expression for I(V) in terms of f(E) may be inverted to give f(E) from observed I(V). The objective is to accomplish the unfolding with high accuracy in f(E) with sufficient energy resolution to study departures from equilibrium. For energies $E < \Delta_1 - \Delta_2$, the inversion process is well behaved, i.e. I(V) is very sensitive to fractional changes in f(E) and vice versa. Figure 3.2 shows the behavior of the convolution function G(E,V) for a set of different values of E. The sharp cutoff for $eV < \Delta_1 - E$ suggests that I(V)

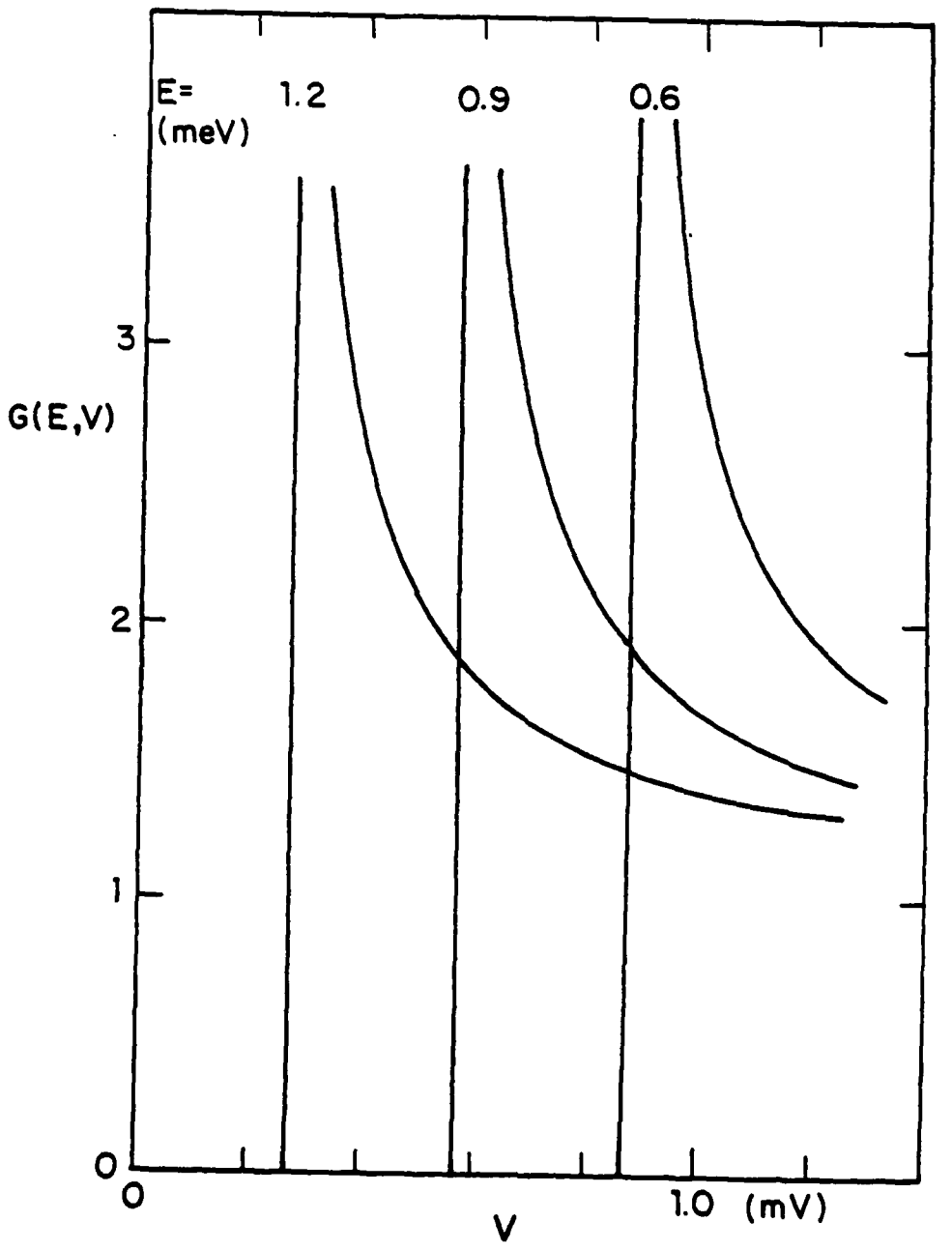

FIGURE 3.2. G(E,V) dE: The contribution a quasiparticle in the energy range E to E + dE makes to the tunneling current I(V). Parameters Δ_1 and Δ_2 are taken as 1.475 and 0.259 meV respectively.

measurements for voltages near $(\Delta_1 - E)/e$ will be most important in determining the occupation number f(E).

In practice it is convenient to remove the strongest energy dependence of f(E) by incorporating the assumed Fermi function $f^o(E)$ into a new normalized occupation function $\tilde{f}$ defined by:

$$\tilde{f}(E) = f(E)/f^o(E) \tag{3.5}$$

A corresponding $\tilde{G}(E,V)$ is defined:

$$\tilde{G}(E) = G(E)\ f^o(E) \tag{3.6}$$

which preserves the form of the convolution

$$I(V) = \int_o^\infty \tilde{G}(E,V)\ \tilde{f}(E)\ dE \tag{3.7}$$

The inversion process is made tractable by taking measurements $I(V_j)$, $(j=1,\ldots,n)$ and dividing the energy spectrum into "bins" $[E_i,E_{i+1}]$, $(i=1,\ldots,m)$. For a given energy bin $\tilde{f}(E)$ may be replaced by a mean value and $\tilde{G}(E,V)$ may be integrated to produce a form convenient for applying discrete matrix methods.

$$\tilde{f}_i = \langle \tilde{f}(E) \rangle_{\text{Averaged over } [E_i, E_{i+1}]} \tag{3.8}$$

$$\tilde{G}_{ji} = \int_{E_i}^{E_{i+1}} \tilde{G}(E, V_j)\, dE \tag{3.9}$$

Incorporating matrix notation gives:

$$I(V_j) = \sum_i \tilde{G}_{ji} \quad \tilde{f}_i \quad = \quad (\quad \underline{\tilde{G}} \quad \underline{\tilde{f}} \quad)_j \tag{3.10}$$

or more compactly:

$$\underline{I} = \underline{\tilde{G}} \quad \underline{\tilde{f}} \tag{3.11}$$

If the number of data observations n exactly equals the number of unfolding bins m, then equation (10) represents the n independent linear equations which can be solved by matrix inversion to obtain the $\tilde{f}$ values. However if more data points are taken, the inversion becomes overdetermined, which allows the advantageous use of a least squares unfolding procedure with resultant noise averaging. For the unfoldings reported, typically 45 data points were used to calculate 20 $\tilde{f}$ values, so the unfolding was well overdetermined.

To solve the set of overdetermined equations, a least squares formula was developed. The mathematical criterion that the choice of the 20 $\tilde{f}$ values must minimize

$$\chi^2 = \sum_j [(I(V_j) - \sum_i \tilde{G}_{ji} \tilde{f}_i)/ \sigma_j]^2 \qquad (3.12)$$

was used to specifiy the unfolding. The measurement uncertainty for each data point σ has been introduced to correctly weight the data points. For given input currents and uncertainties, and computed $\tilde{G}$ values, the χ^2 function describes a simple paraboloid in 20-space, and hence has only one minimum. Standard procedures (Bevington, 1969) solve for the least squares fit values:

$$\underline{\tilde{f}} = [(\underline{\tilde{G}}^T \underline{W} \underline{\tilde{G}}) \underline{\tilde{G}}^T \underline{W}] \underline{I} = \underline{D} \underline{I} \qquad (3.13)$$

$$W_{ij} = \delta_{ij} (1/ \sigma_j)^2 \qquad (3.14)$$

where $\underline{W}$ is a diagonal weighting matrix to account for instrument resolution σ_j, and $\underline{D}$ is the resultant deconvolution matrix. Of course for the inversion not to be undefined the number of data points n must at least equal the number of bins m.

A coefficient may be constructed from $\underline{D}$ to help understand which current measurements contribute most highly in determining occupation of a given energy range. The normalized element $D_{ij}I_j/\bar{f}_i$ indicates the fractional contribution of the j^{th} current measurement to the calculation of the i^{th} occupation number. Figure 3.3 shows the deconvolution fractions $D_{ij} I_j /\bar{f}_i$ for an experimental equilibrium set of data. As expected, the current measurements which are most significant in determining f(E) are those taken at voltages near $(\Delta_1 - E)/e$.

The accuracy and sensitivity inherent in the unequal gap unfolding procedure is illustrated in figures 3.4 and 3.5, which show unfolding results for a set of equilibrium data. The parameters Δ_1, Δ_2 and T have been adjusted to obtain the best fit consistent with the location of the $\Delta_1 + \Delta_2$ current step; it was not found to be necessary to include a gap smearing parameter to describe departures from the BCS density of states. However it did slightly improve the fit to correct for a small parallel constant leakage conductance typically 4000 times smaller than that of the normal state. Mean deviation relative tc the Fermi distribution is less than two percent over three orders of magnitude in f(E), while the absolute resolution for equilibrium quasiparticle occupation is in the 10^{-6} range for the higher energy states.

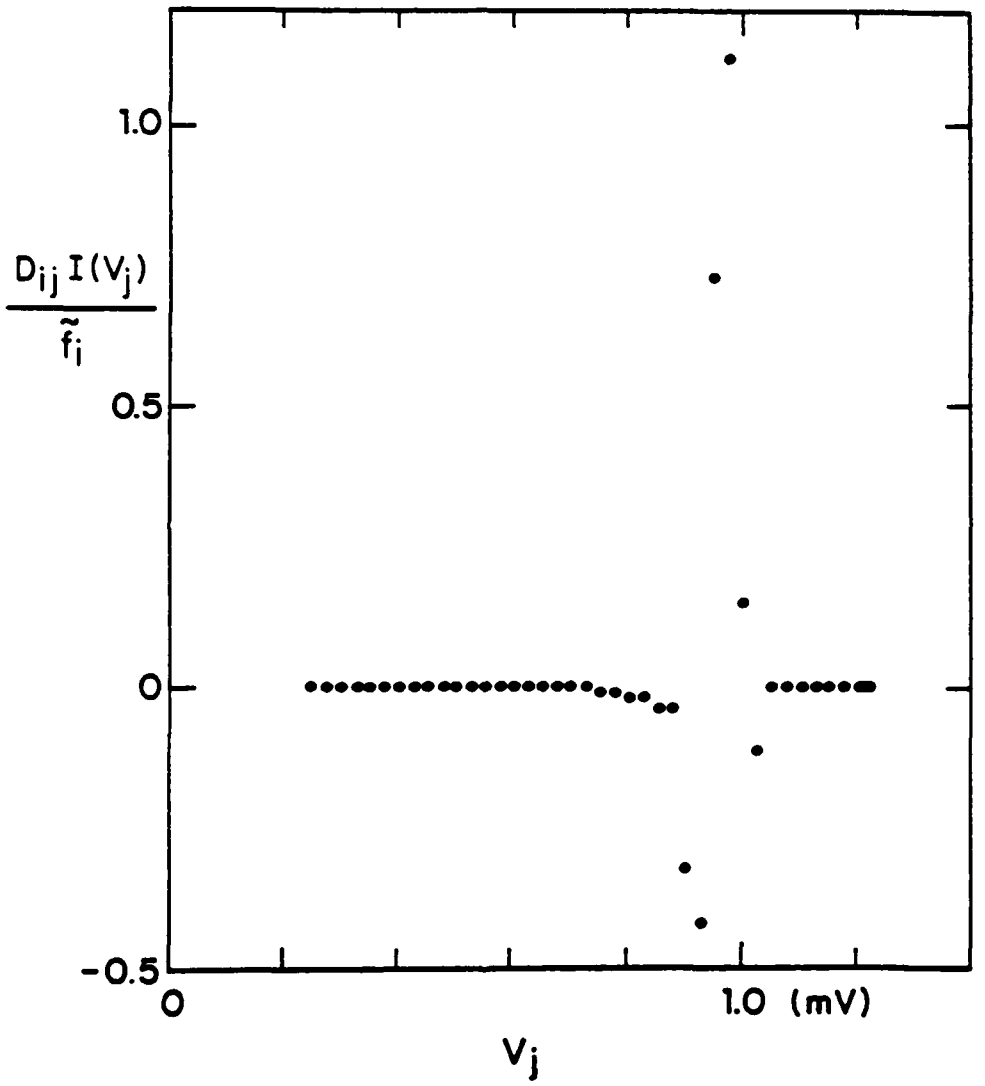

FIGURE 3.3. Experimental normalized deconvolution elements $D_{ij}I_j/f_i$ vs. V for one particular bin "i". The temperature is assumed T = 1.586 K, Δ_1 = 1.475 meV, and Δ_2 = 0.259 meV. The energy bin is [0.50, 0.55] meV.

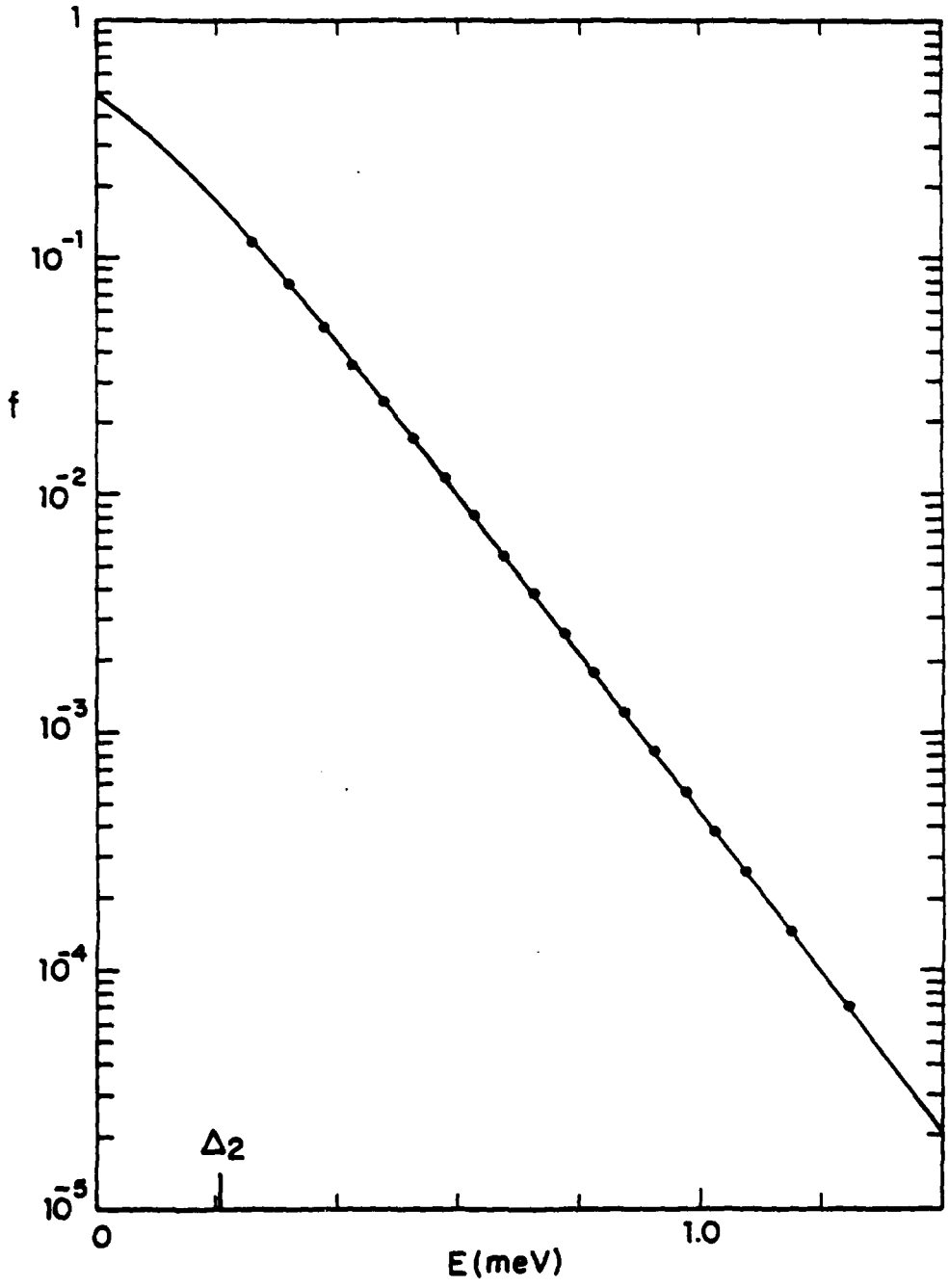

FIGURE 3.4. Unfolded equilibrium values of f(E) vs. E. The solid line is a fit to the Fermi distribution with T = 1.506 K. Unfolding parameters are Δ_1 = 1.442 meV, Δ_2 = 0.2053 meV, T = 1.506 K, R = 51.3 Ω, and g = 1/200 kΩ.

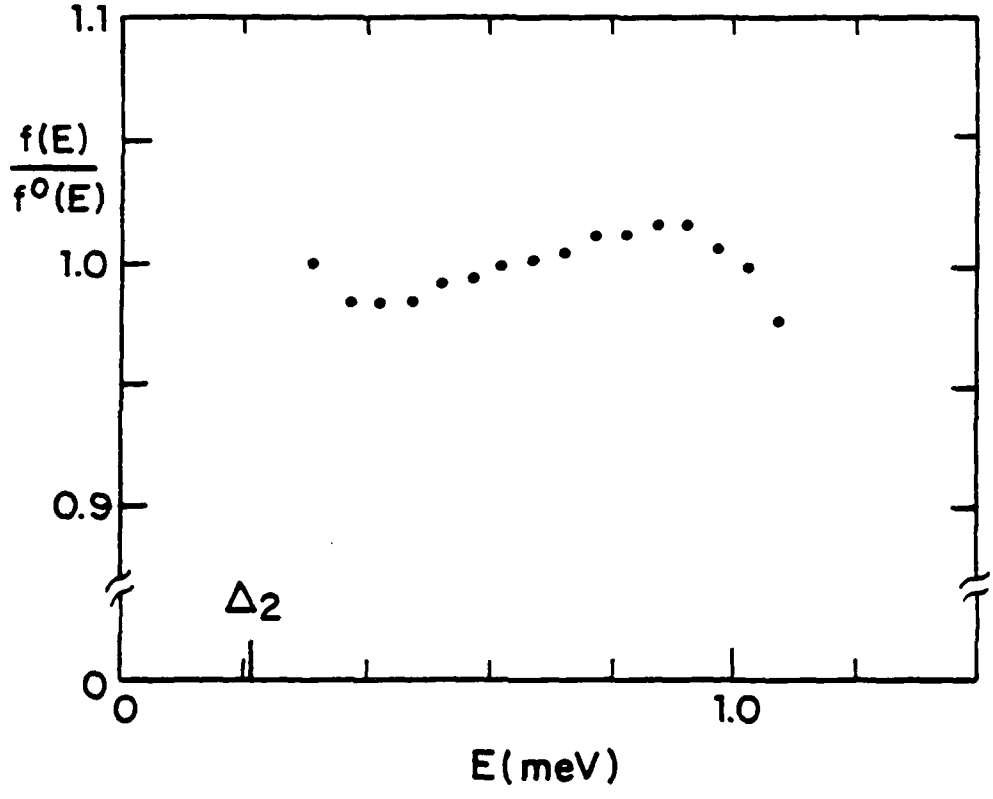

FIGURE 3.5. Unfolded equilibrium values of f(E) vs. E normalized to the Fermi distribution with temperature 1.506 K. Parameters are as in Fig. 3.4.

B. Unfolding for small perturbations

For the case of small nonequilibrium unfolding, where only departures from equilibrium currents are measured, a small modification of technique is necessary. Irradiation changes f(E) by an amount f(E), which increases the observed current. An increase in f(E) will also have the effect of decreasing the gap, which will subsequently also cause a change in the tunneling current. Differentiating equation (3.7) yields the linearized approximation:

$$\delta I(V) = \int \tilde{G}\, \delta \tilde{f}\, dE + \delta\Delta_1 \int \frac{\partial \tilde{G}}{\partial \Delta_1}\, \tilde{f}\, dE + \delta\Delta_2 \int \frac{\partial \tilde{G}}{\partial \Delta_2}\, \tilde{f}\, dE \quad (3.15)$$

where $\delta\Delta_1$ is the shift in the gap parameter for superconductor "i". Figure 3.6 shows the shape of the incremental change in current resulting from a change in Δ_1 and a change in Δ_2 compared to a $\delta f(E)$ of the μ^* type and a $\delta f(E)$ of the T* type. These shapes are best understood by reviewing the semiconductor tunneling picture algebraically described by the third term of equation (3.3). Because a drop in Δ_2 decreases the density of states $N_2(E)$, especially near the gap, the effect of $\delta\Delta_2$ on $\delta I(V)$ is to decrease the current, particulary at the singularity. A depression in Δ_1, however, at a given voltage V, has the effect of

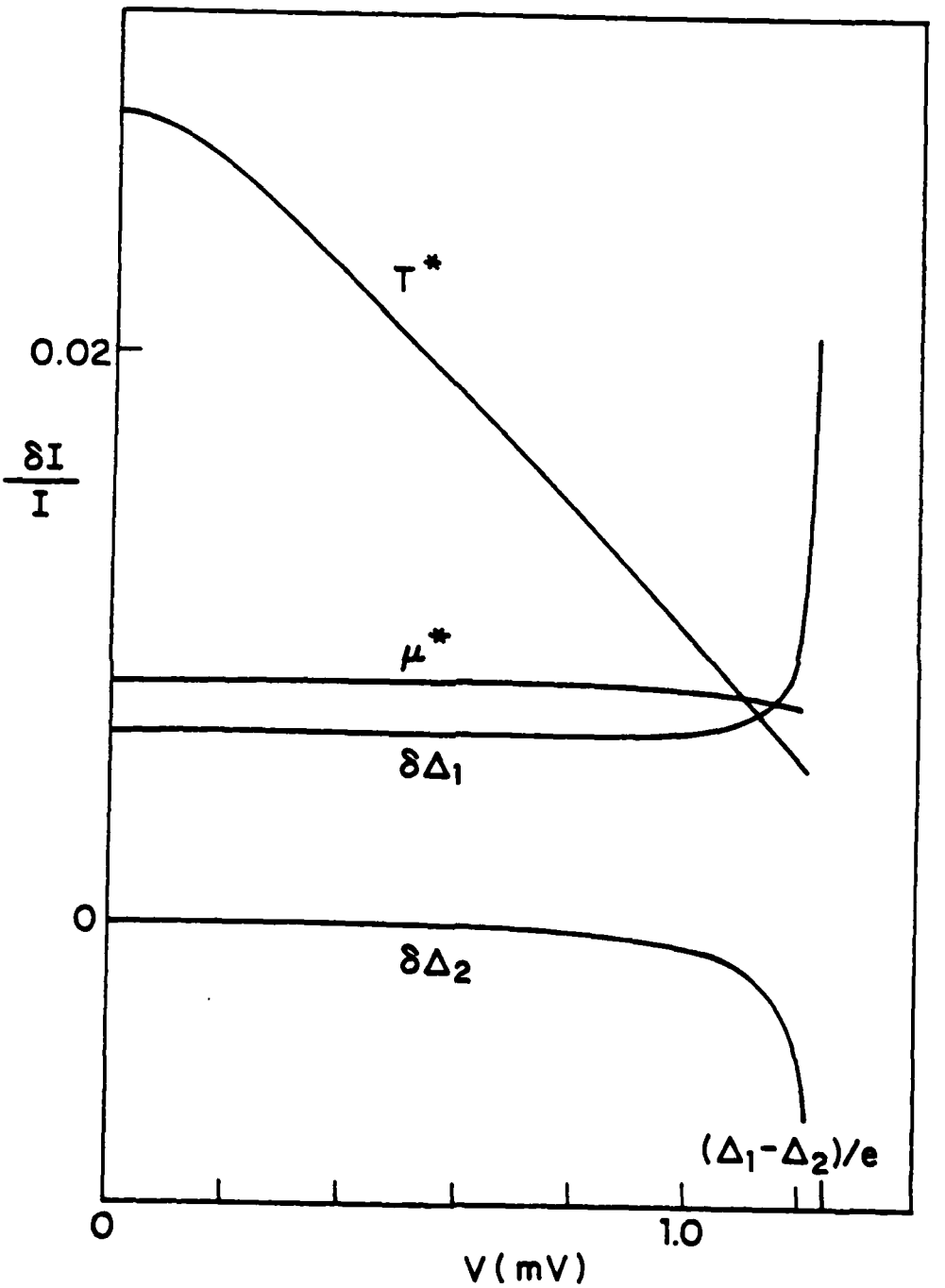

FIGURE 3.6. Relative shapes of $I(V)/I(V)$ predicted for changes in Δ_1, Δ_2, T^*, and μ^*. (Only one parameter is varied per curve.) Equilibrium parameters are the same as Fig. 3.4, while $|\delta\Delta_1| = 0.88$ μeV, $|\delta\Delta_2| = 0.88$ μeV, $\mu^* = 1.1$ μeV, and $\delta T^* = 4$ mK.

initiating tunneling of aluminum quasiparticles with energies in the range $\Delta_1 - eV - \delta\Delta_1 < E < \Delta_1 - eV$. Except near the singularity, a drop in Δ_1 contributes fairly uniformly to the relative increase in current. Note that except for measurements taken at voltages near $\Delta_1 - \Delta_2$ it is very difficult to differentiate the effects of a drop in Δ_1 from a change in the effective aluminum chemical potential μ^*. Consequently it is important to have an accurate estimate of $\delta\Delta_1$ in order to make deductions about the possible μ^* character of f(E).

Assuming the equilibrium state f(E) is known, it is possible to correct for $\delta\Delta_1$ and $\delta\Delta_2$ effects by subtracting the appropriate currents contributed by the respective gap drops. The resultant $\delta I(V)^{eff}$ can then be unfolded in a similar manner as for I(V). Experimentally the quantity $\delta\Delta_1 + \delta\Delta_2$ may be measured by observing the current jump voltage. It is necessary, however, to make some self-consistent assumption about the relative sizes of $\delta\Delta_1$ and $\delta\Delta_2$. As a check on the inferred $\delta\Delta_2$, the resultant $\delta f(E)$ should satisfy the BCS gap equation for the reduced gap value. Given an accurate parameterization of the equilibrium state, current represented by the $\delta\Delta_1$ and $\delta\Delta_2$ terms in equation (3.15) may be readily subtracted out as a background current, and the unfolding may proceed as before. For comparison to theory, it is often then useful to compute $\delta f/f$. This is readily accomplished by dividing the ac $\delta f/f^o$ values by the dc f/f^o results.

The advantages of using the ac technique are that the high sensitivity and good noise rejection of phase sensitive detection can be used to measure very small changes in occupation numbers (see Chapter IV.). In addition, the dc (equilibrium) data can be used to precisely determine the important parameters (Δ_1,Δ_2, T, and R) needed to do the unfolding.

C. Error Analysis

Before applying the unfolding technique to real nonequilibrium data, it is important to understand what types of errors will enter into the deconvolution, and what the sizes of these errors will be.

Systematic unfolding errors can result from incorrect choice of parameters for the unfolding. Although location of the gap singularities provides a fairly good estimate of Δ_1 and Δ_2, R is known from normal state resistance, and T can be measured with a thermometer, small errors in parameter estimates can still present problems. For the unfolding procedure to provide useful information about the nonequilibrium state, it is important that small errors in input parameters should not drastically change results of the unfolding.

To check the sensitivity of the output $\bar{f}$ values to erroneous choices of material parameters, a theoretical I(V) curve was computed by

numerical integration. Figure 3.7 shows the results of unfolding calculated BCS model I(V) data points with various parameter errors. The dc unfolding is sensitive to even small changes in the input parameters. This sensitivity can prove useful in getting better estimates of the key parameters.

For the nonequilibrium unfolding, the results are highly insensitive to mistakes in the input parameters. To check this assertion, $\delta I(V)$ values were calculated using a model T* distribution. The nonequilibrium currents were then unfolded using erroneously selected input parameters. Figure 3.8 shows the results of unfolding with parameter errors similar to those used for figure 3.7. The excellent error immunity is the result of the use of equilibrium $\tilde{f}$ values to normalize out most errors.

A related source of systematic error is miscalculation of the unfolding elements because the densities of states for the two metals are not perfectly described by the BCS density of states. In reality, there is always some smearing of the gap. The smearing may be due to inhomogeneity, anisotropy, or finite lifetime effects (Dynes, et al., 1978). For both PbBi and dirty aluminum, the gap width is quite sharp. The 20 μeV width of the $\Delta_1 + \Delta_2$ rise does provide a limit to the energy resolution obtainable without using a more realistic density of states.

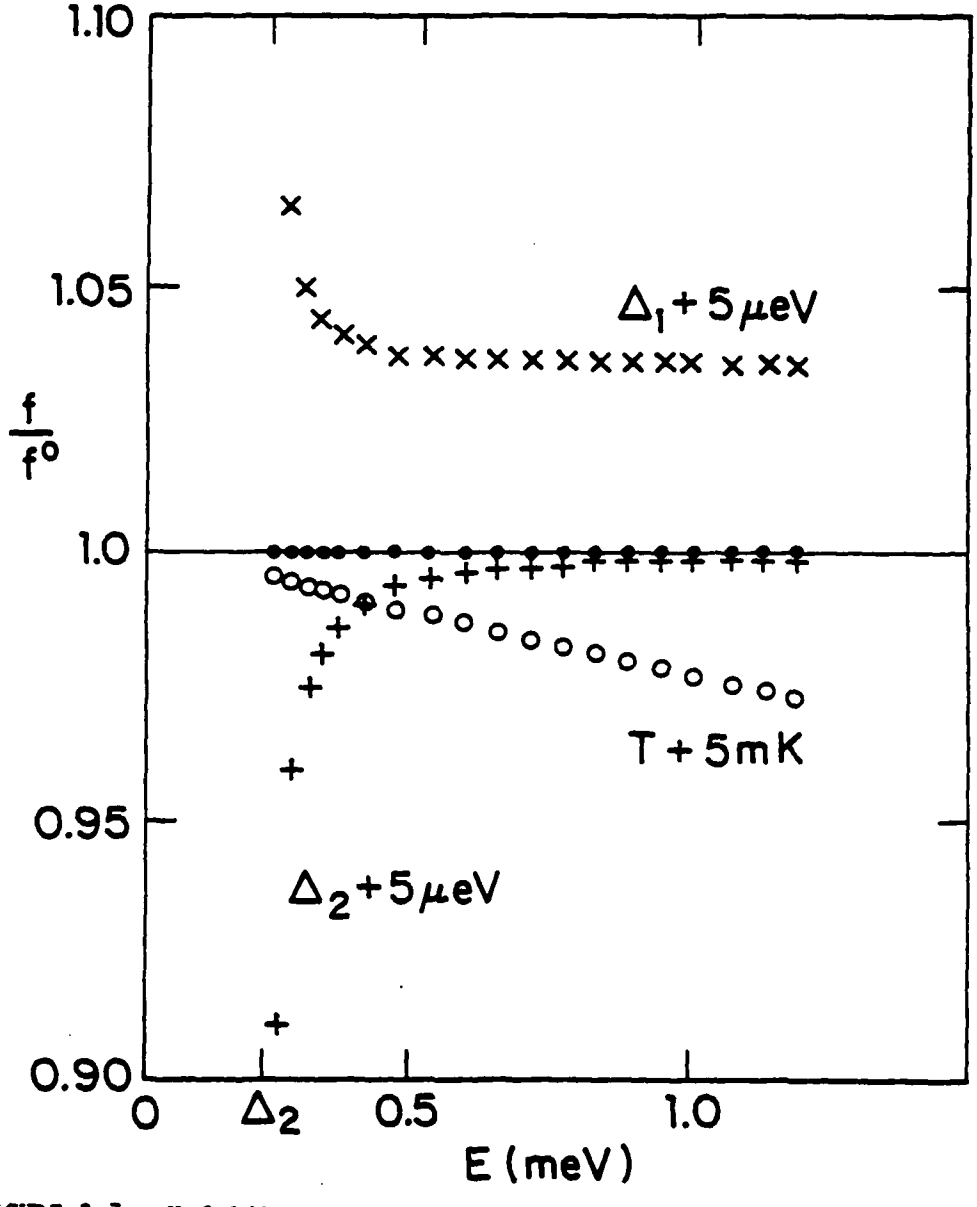

FIGURE 3.7. Unfolding results for correct values of parameters Δ_1, Δ_2, and T (solid dots), and with errors in unfolding parameters (as marked).

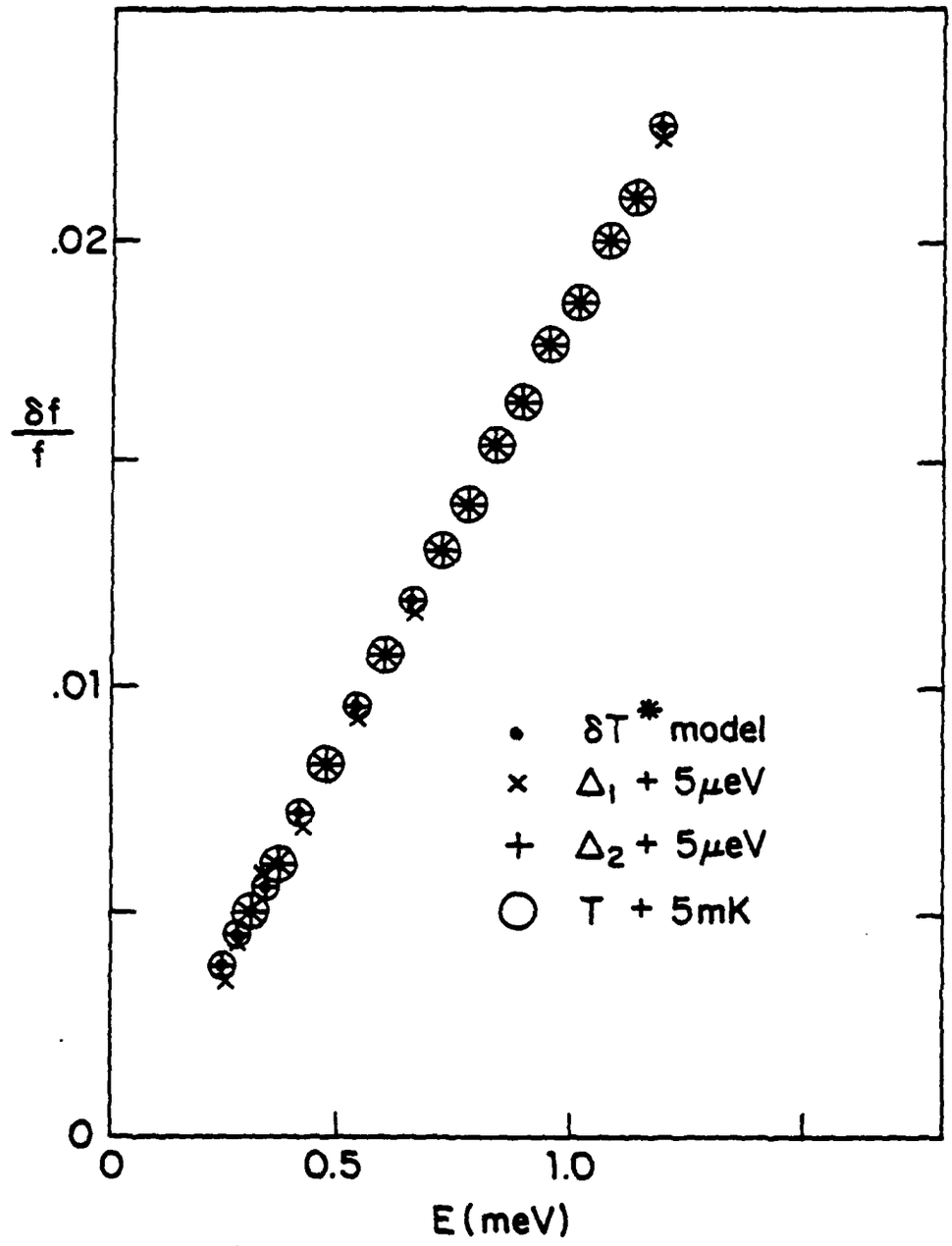

FIGURE 3.8. δT^* model unfolding results for correct parameters (dots) and with errors in unfolding parameters (as marked).

Random errors enter the unfolding from three sources: electronic noise in measuring the current of a data point, noise in measuring the voltage of a data point, and roundoff error during the unfolding calculations.

The quantitative effect of mismeasurement of current can be readily calculated using equation (3.12). Assuming independent errors σ_j in measuring the current I_j, the variance in unfolding $\tilde{f}_i$ is given by:

$$\sigma_{f_i}^2 = \sum_j (D_{ij} \ \sigma_j)^2 \qquad (3.16)$$

Because constant current biasing is used, the most important random error in measuring current is caused by the limited resolution of the analog-to-digital converters used in the Analog Devices input board of the microcomputer. These errors have been measured using a dummy sample and are in agreement with the manufacturer's specifications, namely, 0.1 per cent of the measured current. For the unfolding illustrated in figure 3.3, application of equation (3.15) suggests an uncertainty in the dc f(E) values of 0.2 per cent.

Noise currents are not a significant problem except at the highest sensitivities. Johnson noise, at < 3 pA, is several orders of magnitude smaller than the externally applied current. Rf pickup is largely shunted by the junction capacitance, while line pickup is minimized by careful shielding, using twisted pairs, and avoidance of ground loops.

Mismeasurement of the voltage of a given data point can be translated into an effective error in reading the current as

$$\sigma_j^{eff} = (dI/dV) \quad \sigma_{V_j} \tag{3.17}$$

The voltage error is primarily due to low frequency ("1/f") noise in the PAR 113 preamplifier averaged over a measurement period, and amounts to roughly 1 microvolt. Because the current is roughly exponential in voltage,

$$\sigma_j^{eff}/I_j \approx e\, \sigma_{V_j}/kT \tag{3.18}$$

For T = 1.5 K, this error is 0.75 per cent. Plugging into equation (3.16) yields an error in f(E) of 1.5 per cent.

The final source of random noise, computer roundoff error, is more difficult to calculate directly. The individual data points are stored with six digit accuracy (far more accuracy than the data is taken with), but the iterative arithmetic operations which go on in the correlations and matrix inversion each introduce roundoff error. To test the significance of these errors, computed BCS model I(V) data points were fed in as simulated data and unfolded. The results were accurate to the 4 digit print out resolution used. Roundoff errors, in other words, should be an insignificant component of the total noise.

D. Unfolding for equal gap tunnel junctions

The unfolding procedure described in sections III. A. and III. B. is also valid for symmetric tunnel junctions, and my first efforts to do unfolding involved symmetric tin-tin oxide-tin tunnel junctions. Unfortunately there are significant practical limitations to useful application of these techniques (Jaworski and Parker, 1979). These inherent limitations may be understood within the framework of the notation already introduced.

For purposes of discussion, it will be assumed that phonons crossing the oxide maintain f(E) equal on both sides of the junction. (Results vary only slightly if this constraint is eliminated.) For obvious reasons the restriction to study only those states with $E < \Delta_1$ will be dismissed for this symmetric tunneling case. Furthermore, the necessity of avoiding pair-breaking tunneling is now translated to the requirement that data be taken at voltages $eV < 2\Delta$.

Figure 3.9a shows the semiconductor model picture of quasiparticle tunneling in a symmetrical tunnel junction biased at a voltage V. For a particular quasiparticle state with energy E_o, the voltage has been chosen just less than $(E_o-\Delta)/e$. The electron-like quasiparticle states noted on the upper branch are, by the zero branch-imbalance assumption, populated the same as the hole-like quasiparticle states shown on the lower branch. As shown, both electron-like and hole-like tunneling is

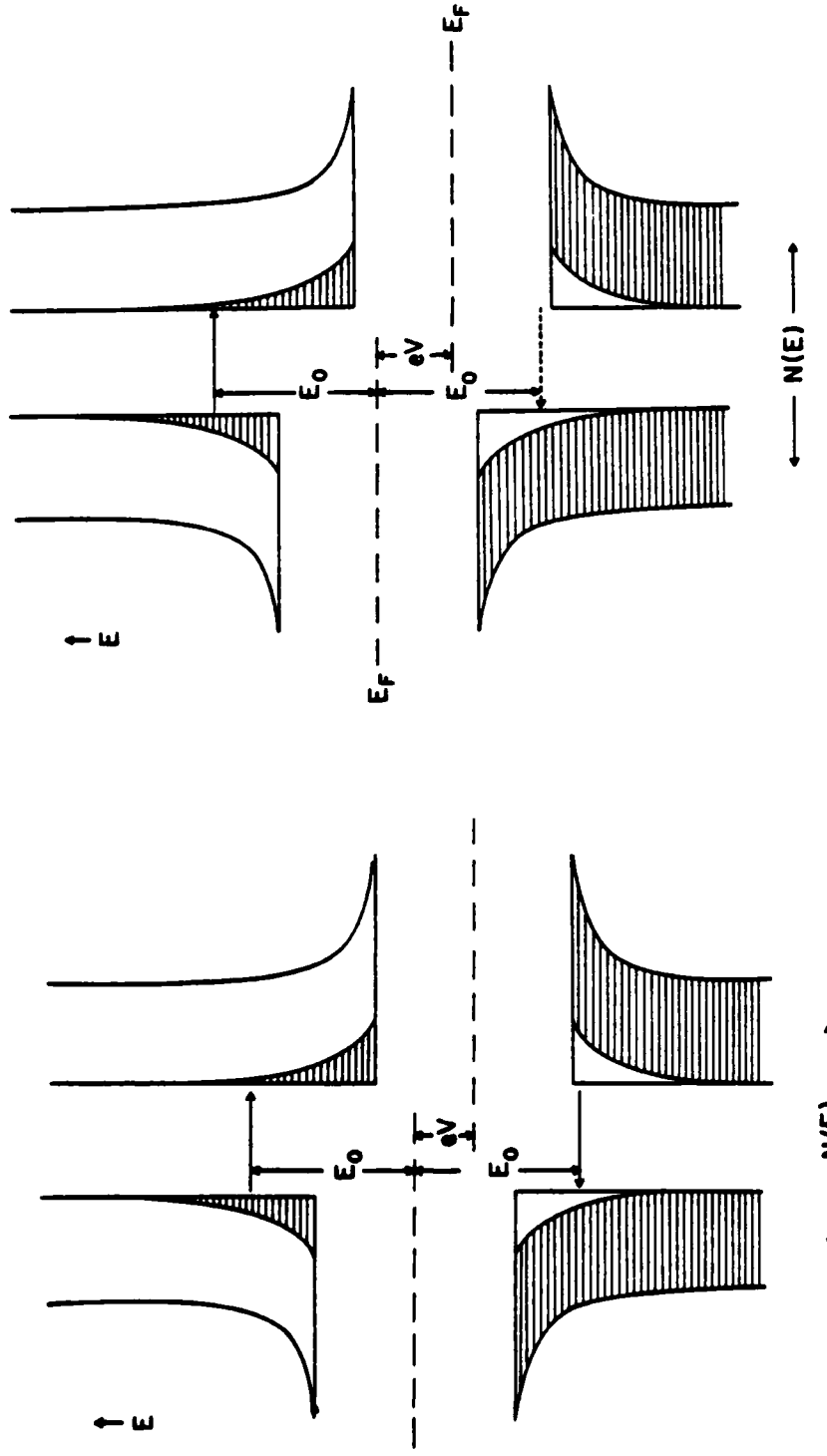

FIGURE 3.9. Semiconductor-model of tunneling into left-side states with energy E_o for two different voltages V.

allowed. Because the lower branch is opposite a larger density of states than the upper branch, the net current flow from E_o states will actually be against the direction of the applied voltage! The situation changes suddenly as the voltage is increased slightly, as shown in figure 3.9b. Tunneling into the lower branch states is now disallowed. As a result, only the contribution to the total current from states with energy E_o is now positive.

Figure 3.10 shows the resultant behavior of G(E,V) for this particular value of the energy E_o. The critical voltage is marked as V_o, and it satisfies the condition that $eV + E = \Delta$. There is a square root singularity as the gap singularity is approached with increasing voltage, followed by a jump to a fairly steady value near unity. In contrast to the asymmetric tunneling case (see figure 3.2) where tunneling begins at voltage $(\Delta_1 - E)/e$, symmetric tunneling changes at a voltage $(E - \Delta)/e$.

The major difficulty with symmetric junction unfolding stems from the fact that the current jump at $(E-\Delta)/e$ is masked by the larger current contributions of the states with lower energies (and hence higher occupations!). In contrast, with asymmetric tunneling the current increase for a given energy occurs with contributions from the less populated states, which can be readily subtracted out (Gray and Willemsen, 1979b).

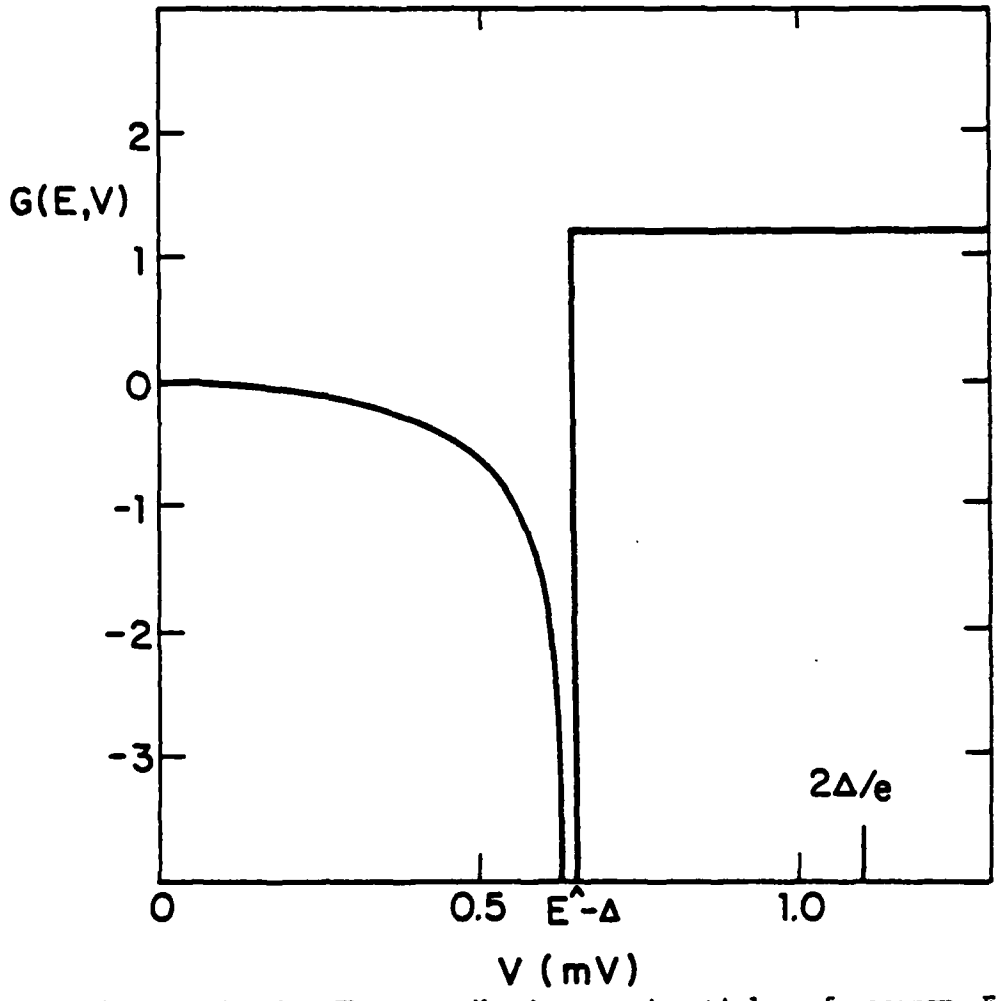

FIGURE 3.10. G(E,V): The contribution quasiparticles of energy E make to the tunneling current I(V). Parameters are Δ and E are taken as 0.55 meV and 1.2 meV respectively.

Of course the mathematical inversion process is still correct in theory. For noise-free data and perfectly defined densities of states, the procedure will still give correct f(E) values for output. For real data, however, the signal-to-noise problems become unmanageable (Jaworski and Parker, 1979). Quantitatively this can be understood from calculation of the unfolding elements $D_{ij}\ I_j/\bar{f}_i$, plotted in figure 3.11. The large values and slow convergence indicate that the output unfolding values will be quite sensitive to noise in the current measurements. (See equation 3.16).

A second difficulty with symmetric junction unfolding involves handling "leakage" currents, multiparticle tunneling, and other anomalous additional currents. High sensitivity is needed to measure the occupation of the high energy states. Unfortunately for symmetric tunnel junctions the data most important in calculating these states is taken at voltages near $2\Delta/e$ where these anomalous currents are largest. For asymmetric junctions, on the other hand, one calculates high energy occupations using current measurements taken near V=0, where at least some of the anomalous currents are small.

As we have seen, asymmetric tunnel junctions offer some important advantages over symmetric tunnel junctions for unfolding to obtain occupation numbers. The unfolding procedure can be used to extract highly accurate information about the occupation of the nonequilibrium states.

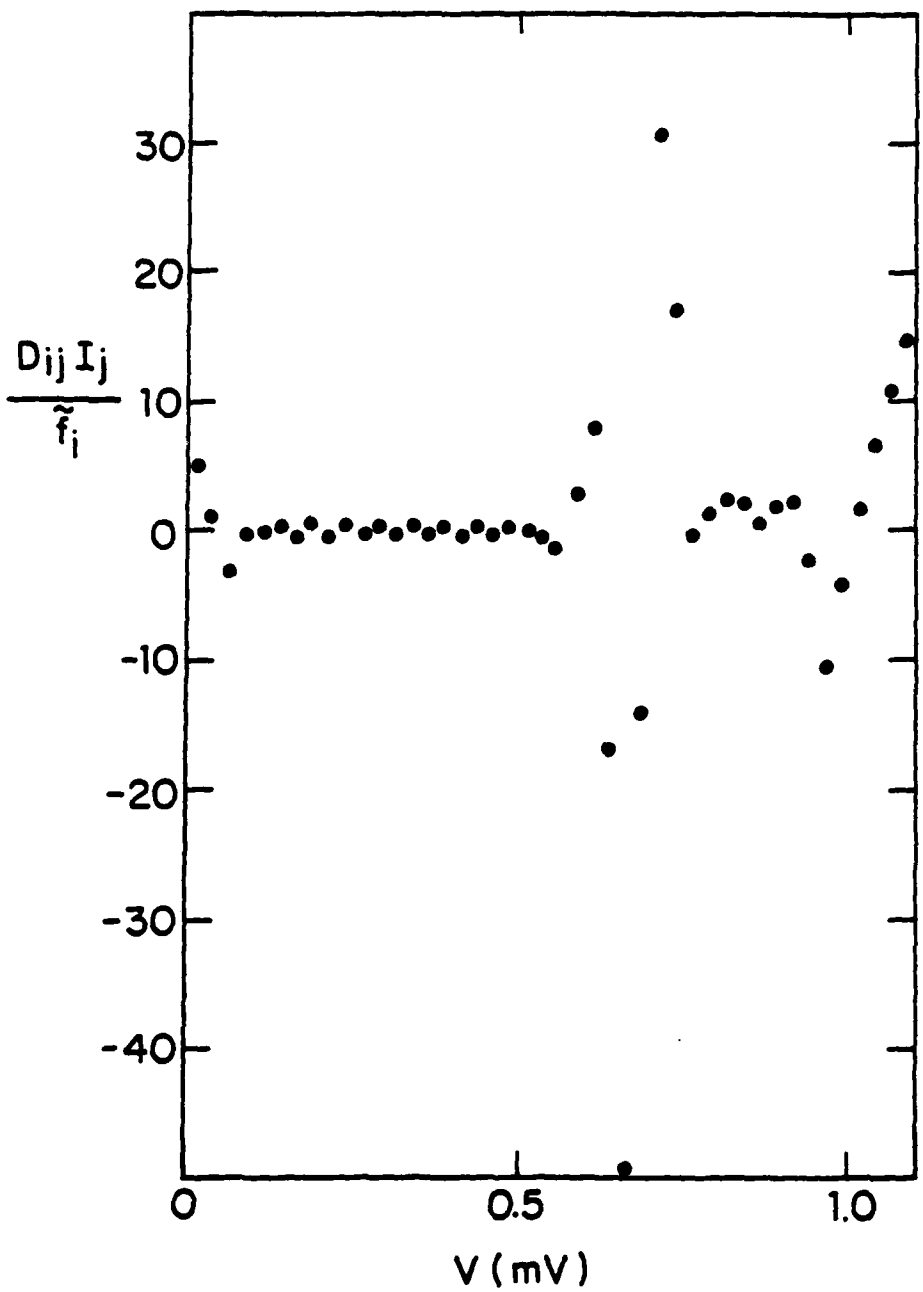

FIGURE 3.11. Normalized deconvolution elements for unfolding I(V) for a symmetric tunnel junction. The temperature is assumed T = 2.17 K, and Δ = 0.55 meV. The energy bin is [1.2, 1.25] meV.

Chapter IV. RESULTS OF NONEQUILIBRIUM STATE UNFOLDING

A. Aluminum-Side Illumination

The unfolding program was used to analyze data taken for both aluminum-side and lead-bismuth-side illumination. For illumination of the dirty aluminum the assumption $\delta\Delta_{Al} >> \delta\Delta_{PbBi}$ is appropriate. (For clarity the subscripts 1 and 2 used in the previous chapter have been identified explicitly with the lead-bismuth and aluminum films respectively.) Photon absorption occurs only in the aluminum; the lead-bismuth is perturbed only by phonons escaping from the aluminum film. Most of the phonons from the aluminum film have energies of roughly Δ_{Al} (Chang and Scalapino, 1978). The lead-bismuth film is largely transparent to these phonons, since they lack sufficient energy to break lead-bismuth pairs. The lead-bismuth film should remain quite close to the bath temperature. Therefore I assume $\delta\Delta_{PbBi} = 0$ and determine $\delta\Delta_{Al}$ from the experimentally measured value of $\delta(\Delta_{PbBi} + \Delta_{Al})$. This assumption will be tested later. The values of Δ_{PbBi}, Δ_{Al}, and T are the values fixed by fit to the equilibrium (dc) data.

Results of unfolding of data with illumination on the aluminum side are shown in figures 4.1 and 4.2. Increase in the occupation function was limited to a few percent. The data are in excellent agreement with the theoretical $\delta f(E)$ resulting from a rise in the effective

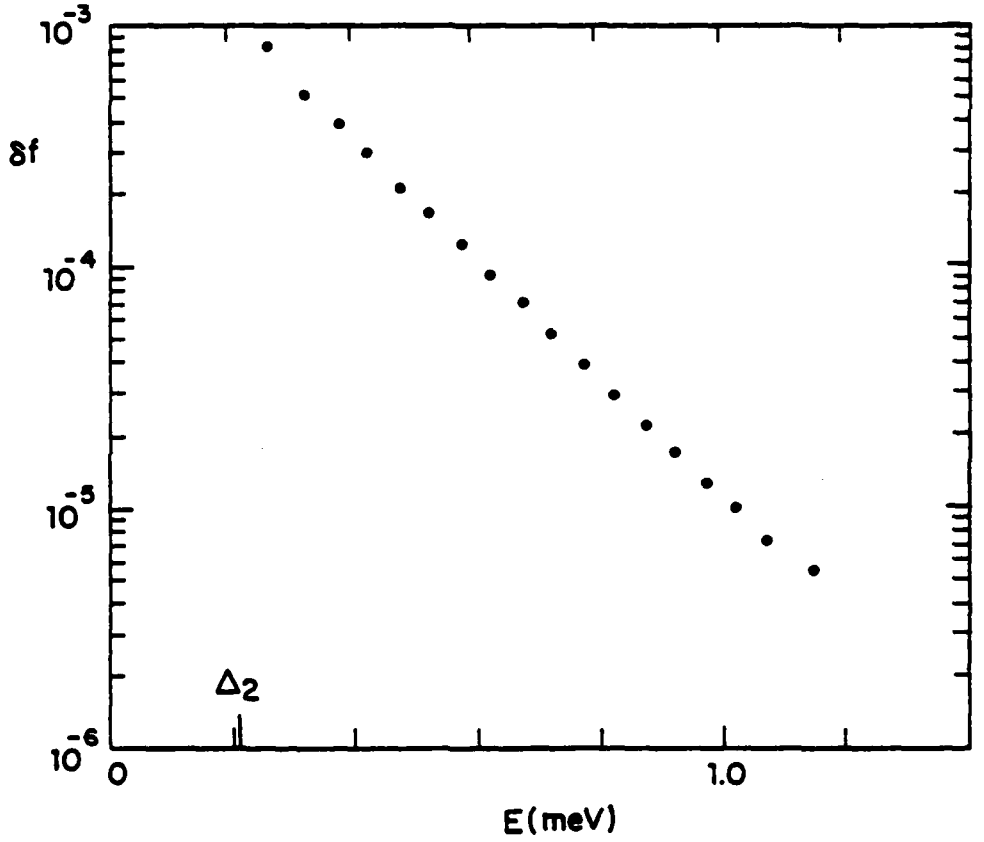

FIGURE 4.1. Unfolded nonequilibrium values of $\delta f(E)$ for aluminum-side illumination. Unfolding parameters are Δ_1=1.442 meV, Δ_2=0.2053 meV, T=1.506 K, R=51.3 ohms, and $\delta\Delta_2$=0.88 μeV.

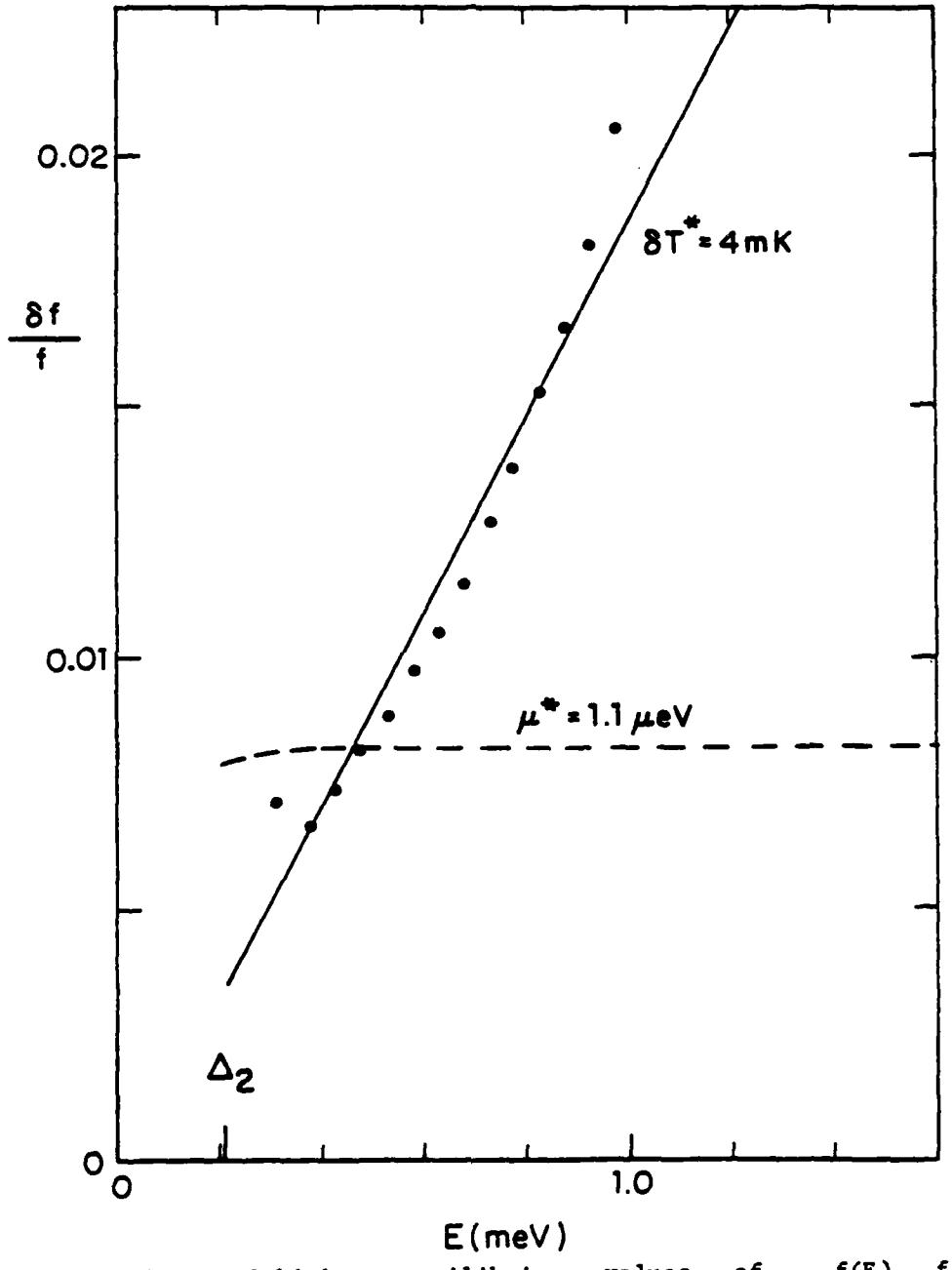

FIGURE 4.2. Unfolded nonequilibrium values of f(E) for aluminum-side illumination normalized to the Fermi distribution with temperature 1.506 K. The solid line is a fit to a T^* model with δT^*=4mK. The dashed line is a μ^* fit with the same number of excess quasiparticles as the T^* fit.

quasiparticle temperature by an amount δT^* equal to 4 mK. As a self-consistency check on the unfolding, the fit δT^* value can be plugged into the BCS gap equation, which can be approximated as:

$$d^2 = 3.016\ (1-t) - 2.45\ (1-t)^2 \qquad (4.1)$$

where $d = \Delta/\Delta(0)$ and $t = T/T_c$. (The expansion was performed by numerically solving the BCS gap equation and fitting the results for $t<0.7$ to within 0.3 percent.) For the data plotted here, a gap drop of 0.88 ± 0.05 μeV was measured from shifts in the $(\Delta_{PbBi} + \Delta_{Al})/e$ jump. This compares quite well to the computed T^* model drop of 0.84 μeV. Thus not only is the shape of f(E) correct, but also the observed decrease in the aluminum gap agrees with the gap decrease expected for a T* fit. Furthermore, the earlier assumption that $\delta\Delta_{PbBi} = 0$ appears justified. Also plotted in figure 4.2 is δf expected for a μ^* distribution corresponding to the observed $\delta\Delta_{Al}$. There appears to be little evidence for a shift in chemical potential for the quasiparticle system.

These quantitative unfolding results are in good agreement with conclusions drawn by Gerbstein, et. al. (1978) who studied intense optical illumination of tin in a tin-tin oxide-lead tunneling structure. The nonequilibrium state they observed closely resembled a thermal state of higher temperature than the bath. Several potential problems involved

with intense optical illumination are avoided with weak illumination. Inhomogeneous state effects due to nonuniform film reflectivity, microscopic laser speckle, or material inhomogeneity should simply average since the perturbation from equilibrium is small enough to be considered in the linear regime. Also the relaxation mechanism and rates should, in large part, be equal to those of the equilibrium state because the excess number of quasiparticles is kept small compared to the thermal occupation values.

In order to compare unfolding results to theory, it is useful to compare the relative speeds of the important relaxation channels. Taking the relaxation times of Kaplan, et. al. (1976), the recombination rate τ_R^{-1} is roughly three times faster than the thermal phonon scattering rate τ_S^{-1}. One does not, therefore, expect a simple μ^* model to give a good description of the nonequilibrium state. The phonon trapping factor, γ, (defined as the inverse of the probability that a recombination phonon will escape the film before breaking a pair) gives a sense of what fraction of the recombination phonons break pairs and hence are able to adjust the energy distribution of the quasiparticles. Studies by Eisenmenger et. al. (1977) show the transmissivity of phonons from aluminum to sapphire is only 0.14. For the film geometry used here, this results in a γ of roughly 20. The high energy phonons are well coupled to the nonequilibrium quasiparticles as is assumed under Parker's T* model. Thus for our experimental conditions the T* model

should be more applicable as a first approximation to the excited occupation distribution, in agreement with out experimental results.

B. Lead-Bismuth-Side Illumination

The experiment was also performed with illumination of the lead-bismuth side of the tunnel junction. From the perspective of the aluminum film, the result of the laser illumination is to create a phonon flow from the lead-bismuth film. Numerical studies by Chang and Scalapino (1978) have shown that most of the energy leaving the lead-bismuth film is in the form of recombination phonons ($\hbar\omega_{ph} \geq 2\Delta_{PbBi} \cong 3$ meV). This energy corresponds to roughly $12\,\Delta_{Al}$. Although the energy per excitation is a factor of 1000 smaller than was the case with the direct optical illumination of aluminum, the general character of the resultant nonequilibrium state is expected to be similar, since in both cases the excitation energies are much larger than Δ_{Al}.

Because of the relatively poor phonon coupling between the superconducting films, an assumption that $\delta\Delta_{Al} \gg \delta\Delta_{PbBi}$ is no longer valid. The observed shift in the $(\Delta_{PbBi} + \Delta_{Al})/e$ current step was again used to gauge the value of $\delta\Delta_{PbBi} + \delta\Delta_{Al}$. Although quantitative measurement of the voltage of the shifted $(\Delta_{PbBi} - \Delta_{Al})/e$

peak in current was impractical due to hysteresis, the sign of the current increment near $V = (\Delta_{PbBi} - \Delta_{Al})/e$ was observed to be in the opposite direction as with aluminum-side illumination (i.e. $\delta\Delta_{Al} \leq \delta\Delta_{PbBi}$ for lead-bismuth-side illumination). The value of $\delta\Delta_{Al}$ was chosen to give the best fit to a T*-like nonequilibrium distribution in the aluminum. The unfolding results are shown in figure 4.3 along with the predicted disequilibrium for a $\delta T^* = 2$ mK distribution. In a consistency check, the aluminum gap drop predicted for the fit δT^* was found to agree with the $\delta\Delta_{Al}$ parameter implied by the choice of $\delta\Delta_{PbBi}$. This would not be the case if $\delta\Delta_{PbBi}$ were chosen as zero as was the case for aluminum-side illumination. It is tempting to attribute the small deviations from the T* model to the effects of $2\Delta_{PbBi}$ phonons from the lead-bismuth; however, the weakness of the self consistency check on the parameters for this case is such that these deviations may not be significant.

The $\delta f(E)$ distribution shape for lead-bismuth illumination is consistent with results for aluminum illumination. Although the initial pair breaking energy of the optical photon is much greater than the $2\Delta_{PbBi}$ phonons, the large phonon trapping factor should dominate in determination of the basic nonequilibrium $\delta f(E)$ shape.

In summary, unfolding of I(V) measurements of dissimilar metal tunnel junctions provides a useful tool for measuring the quasiparticle energy distribution. Absolute sensitivity of 10^{-5} and relative accuracy

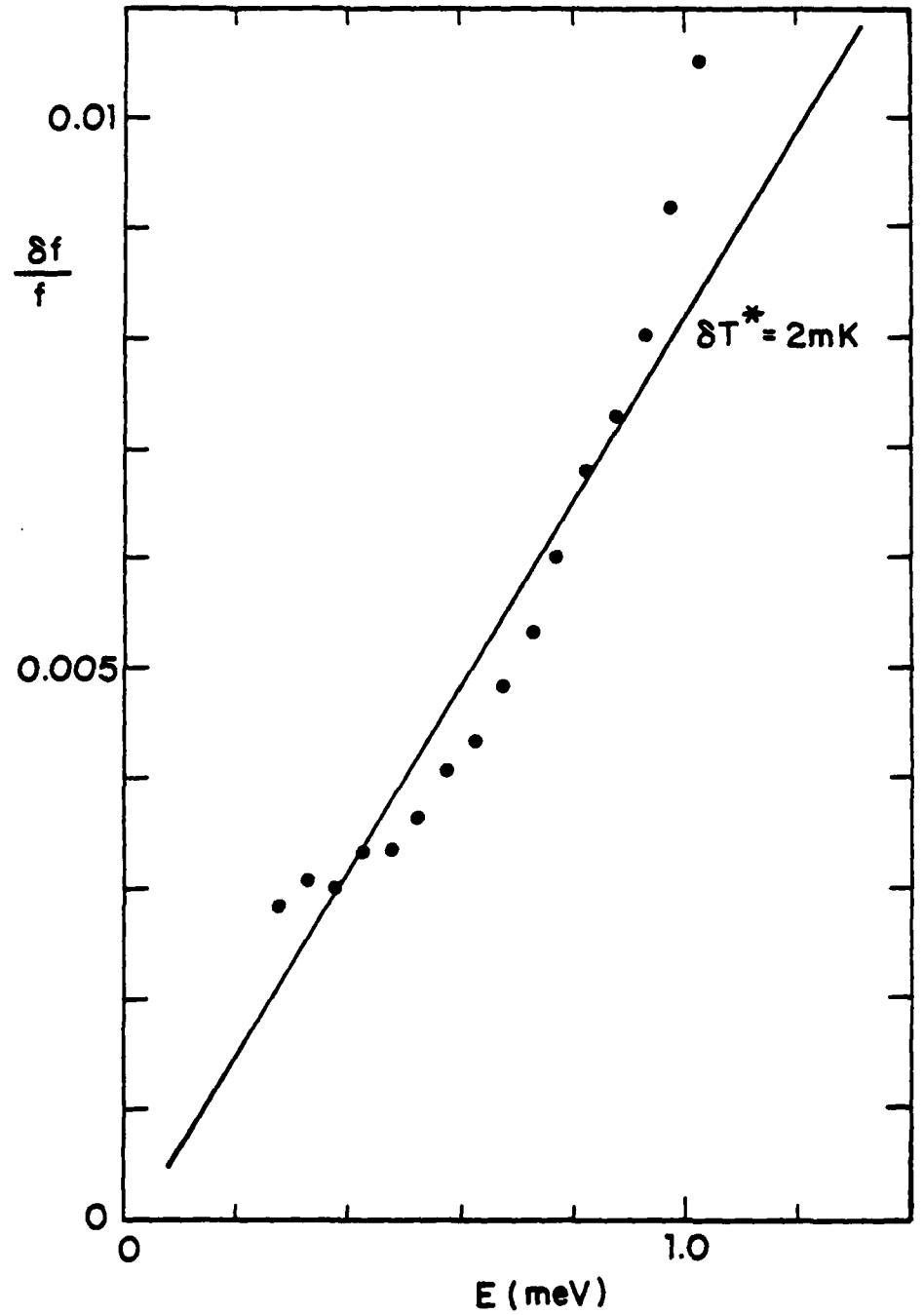

FIGURE 4.3. Unfolded nonequilibrium value of aluminum $\delta f(E)$ for lead-bismuth-side illumination normalized to the Fermi distribution. The equilibrium parameters are essentially the same as Fig. 4.1, while $\delta\Delta_1 = \delta\Delta_2 = -0.48$ μeV. Also plotted is $\delta f/f$ expected for a T^* distribution with $\delta T^* = 2$mK.

of a few percent are readily obtainable for small perturbations from equilibrium. Results of unfolding experimental data from optically illuminated aluminum--aluminum oxide--lead-bismuth tunnel junctions show the aluminum nonequilibrium state is well described by a T* model behavior over several orders of magnitude in $\delta f(E)$. This last conclusion is valid for both optical and high energy phonon illumination of the dirty aluminum film.

V. THERMOELECTRIC EFFECTS IN TUNNEL JUNCTIONS

A. Introduction

The study of unfolding leads quite naturally to the study of thermoelectric effects in tunnel junctions. For the thin oxide barrier of the tunnel junction, temperature gradients of 10^7 K/cm could be obtained readily with laser illumination.

Thermoelectricity in superconductors has been studied in several types of experiments. A temperature gradient across a bimetallic superconducting loop is predicted to induce a current flow around the loop, if the quasiparticles have nonzero thermopower S (Gal'perin, et al., 1974; Garland and Van Harlingen, 1974). A number of different experimental designs have been used to look for such an effect, most recently a laser-heated loop experiment by Schuller and Falco (1978), and a toroidal geometry experiment by Van Harlingen and Garland (1978).

A second group of experiments has concerned thermoelectric effects caused by interaction of temperature gradients and supercurrents. An effect proportional to $\vec{v}_s \cdot \vec{\nabla} T$ was predicted (Pethick and Smith, 1979) to give rise to a local charge imbalance within the quasiparticles which could be measured with a tunnel junction probe. The magnitude of the effect depends on the mean free path of the quasiparticles, as well as Δ, but is entirely independent of the normal state thermopower.

Experiments by Clarke *et al.* (1979), Heidel and Garland (1980), and Van Harlingen (1980) confirm the existence of an emf which is proportional to $\vec{v}_s \cdot \vec{\nabla} T$, although the theoretical magnitude and temperature dependence have been open to debate (Schmid and Schon, 1979; Clarke and Tinkham, 1980).

This chapter and following chapters will treat the discovery of an entirely different type of thermoelectric effect, applicable to tunneling through oxide barriers between both superconductors and normal metals. The effective temperature difference across the oxide barrier gives rise to a thermoelectric current. Observations of this thermoelectric effect will be presented for both open circuit voltage measurements and short circuit current measurements. The existence of this thermoelectric effect can explain discrepancies between experimental results and theoretical predictions in several earlier superconducting thermopower experiments with point contacts.

B. Derivation of a Tunneling Thermoelectric Current

The tunneling barriers in tunnel junctions are typically 10 - 40 Å thick oxides of one of the electrodes. Moderately thick oxide barriers reduce the transmission probability of electrons to cross the barrier to $\sim 10^{-10}$. The oxide barrier also serves as a barrier to phonon propagation (Kaplan, 1979). As a result, the metal films comprising the

tunnel junction can have significantly different temperatures in nonequilibrium situations (Melton, et al., 1980). These effects are especially important at low temperatures, when the phonon heat transmission (~ T^4) is low.

Qualitatively the physical processes explaining a thermoelectric quasiparticle current at zero voltage can be seen in Fig. 5.1, in which the semiconductor-model density of states is plotted for an Al-PbBi tunnel junction. A heat source creates an equal number of electron-like (upper branch) and hole-like (lower branch) quasiparticles in the PbBi, so that the superconductor on the left (PbBi) is effectively at a higher temperature than the superconductor on the right (Al). The Fermi energies are held equal externally by a superconducting shorting wire. Electrons tunnel across the barrier from the PbBi to the Al in the tunneling channel labeled A. There is a back current, labeled B, for states in the lower branch. For an oxide transmission probability X(E) that is energy independent, the charge transfer for the two processes exactly cancels. Harrison (1961) has noted that the densities of states of the metals are proportional to $(dE/dk)^{-1}$ and the group velocities for electrons to approach the barrier are proportional to dE/dk, so that the branch cancellation is independent of density of states changes. If transmission probabilities for A and B processes are not exactly equal, however, there will be a net thermoelectric current, which can be experimentally measured by using a galvanometer in place of the

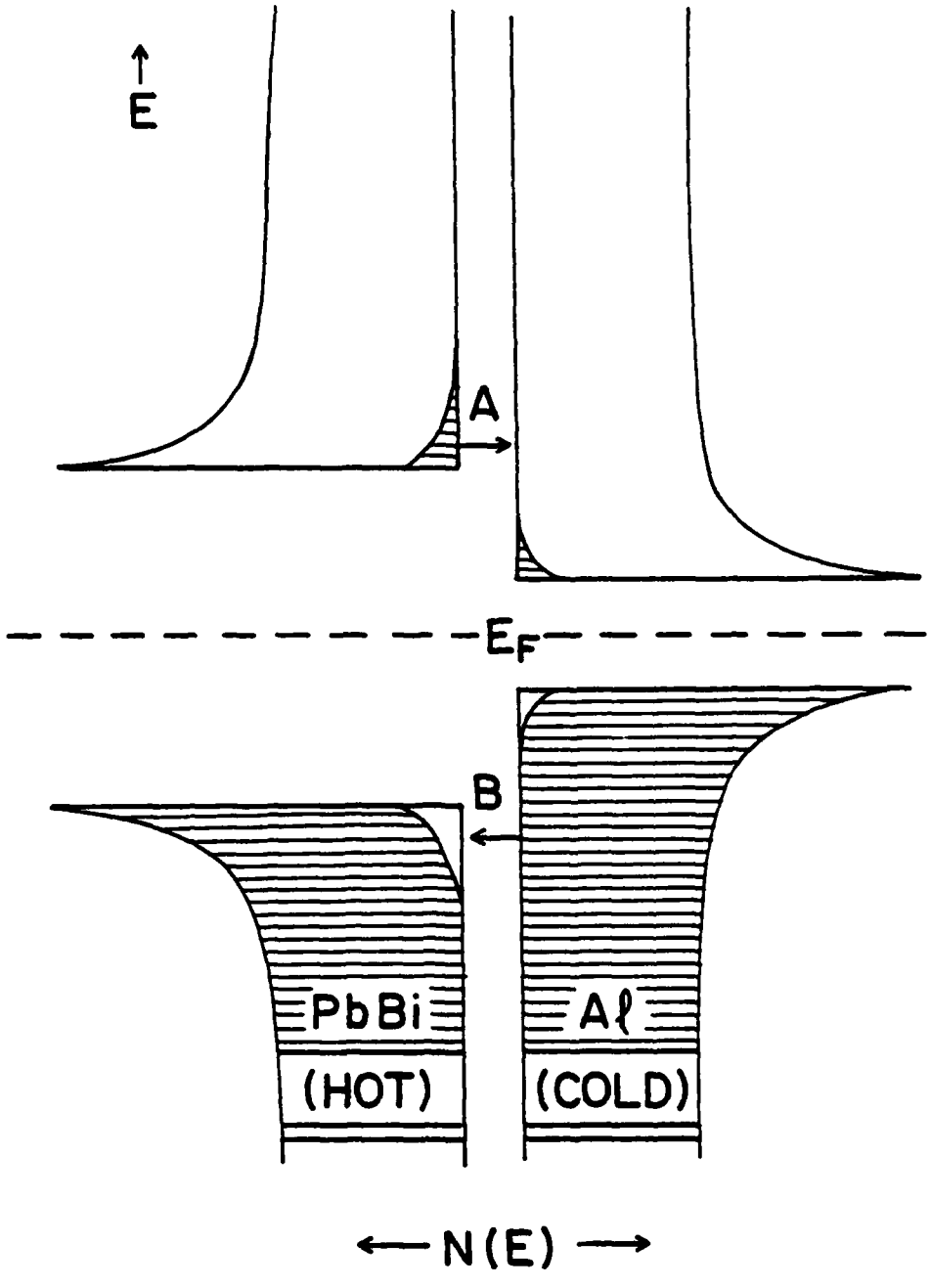

FIGURE 5.1. Semiconductor-model picture of tunneling between two superconductors at zero voltage. Electron-like (A) and hole-like (B) tunneling is shown.

superconducting shorting wire.

An estimate of the energy dependence of the electron transmission probability can be obtained using the one-band WKB approximation. For an oxide barrier potential ϕ, electron energy E (both measured from E_F), and oxide thickness s, X(E) is given by (Hartman, 1964)

$$\ln[X(E)] \cong -\alpha s(\phi-E)^{1/2} + \text{constant} \qquad (5.1)$$

where

$$\alpha = 4\pi(2m)^{1/2}/h = 1.025\ eV^{-1/2}\ \text{Å}^{-1} \qquad (5.2)$$

The dependence of X on the angle of incidence upon the barrier has been integrated out.

We will restrict our analysis to study of tunneling at low voltages, i.e. $V << \phi/e$. In this case, only states close to E_F contribute significantly to the tunneling current. The transmission probability for these states may be expressed in terms of a Taylor's expansion about E_F:

$$\ln(X(E)) = -b + c_1 E + \ldots \qquad (5.3)$$

The fractional change in X as E varies is given by

$$(1/X)\ (dX/dE)\,|_{E_F} = c_1 = d/dE\ \ 1n(X)\,|_{E_F} \qquad (5.4)$$

For the model described by Eq. (5.1) this may be evaluated as:

$$c_1 = \alpha s/(2\ \phi^{1/2}) \cong [23 + 1n(RA)]/(2\phi) \qquad (5.5)$$

where R is in ohms and A is in cm^2.

Typical values of the parameters for an aluminum oxide tunneling barrier would be $s \cong 10$ Å and $\phi \cong 3.7$ eV. (Konkin and Adler, 1974). Evaluating equation (5.5) for electron states near the Fermi surface and a 1 *ohm* cm^2 junction resistivity, this simple model gives:

$$c_1 = 3.1\ eV^{-1} \qquad (5.6)$$

(It should be noted that Gundlach (1973) has done calculations using a slightly more sophisticated, two band model. This model introduces the effects of the valance band of the oxide on the tunneling probabilities. In general the results of these calculations are to lower the estimates of c_1, although accurate predictions for c_1 are rather difficult. The two band model has proven superior to the one band model when applied to explain high voltage asymmetries in tunneling I(V) characteristics (Basavaiah, et al., 1974; Ekrut and Hahn, 1980).)

If the relevent energy separation of the two branches is $2\Delta_{PbBi}$ ($\approx$ 3 meV), equation (4) suggests that the A currents illustrated in figure 5.1 could be expected to be on the order of one percent larger than the B currents.

The exact magnitude of the current depends on the excess number density of excited quasiparticles that are able to tunnel as well as details of the junction itself. The semiconductor model predicts

$$I_o = (1/eRX(0)) \int_{-\infty}^{\infty} X(E)\, N_1(E)\, N_2(E)\, [f_1(E)-f_2(E)]\, dE \qquad (5.7)$$

where I_o is the predicted zero voltage current, N_i is the superconducting density of states normalized to the electronic density of states per spin, N(0), and e is negative. The normalized transmission probability can be expanded as:

$$X(E)/X(0) = 1 + c_1 E + \ldots \qquad (5.8)$$

Using this expression in Eq. (5.7), the first term integrates to zero, leaving:

$$I_o = (1/eR)\, c_1 \int_{-\infty}^{\infty} E\, N_1(E)\, N_2(E)\, [f_1(E) - f_2(E)]\, dE \qquad (5.9)$$

Although the semiconductor model used to describe the phenomena of a thermoelectric current correctly predicts the rough magnitude and correct sign of the effect, it does not carefully take into account the combined hole-electron nature of quasiparticles. (For a more detailed and rigorous calculation of the thermoelectric current, see Appendix II.) The major conclusion should be valid, however, namely that a thermoelectric current proportional to the excess number of quasiparticles able to tunnel should be excited across the oxide barrier of the tunnel junction, i.e.

$$I_o \propto n - n_o(T) \tag{5.10}$$

where n(T) is the number density of quasiparticles (conventionally normalized to $4N(0)\Delta(0)\Omega$, Ω is the electrode effective volume, and n_o is the thermal equilibrium value defined by the counter electrode (Al) effective temperature. (See appendix equations (A.7) and (A.8)).

It should be noted that the thermoelectric current derived here is entirely a tunneling barrier effect. The current is independent of those electrode material parameters normally associated with thermoelectricity: the thermopower S, the quasiparticle diffusion length Λ_Q, the mean free path ℓ, etc. The only important material parameters are those determining the number of quasiparticles which are able to tunnel.

C. Dependence on Bath Temperature and Laser Power

Measurements which will be described more fully in Chapter VII. were taken to study the power and temperature dependence of the thermoelectric effect. As before, a laser was used to supply heat to the lead-bismuth film of the tunnel junction. An advantage of this technique over joule heating techniques is that it avoids inductive or capacitive coupling between external heaters and the tunnel junction. A difficulty of the laser heating technique is that the effective temperature of the illuminated film, T^*, must be estimated rather than measured directly.

The value of $(n - n_o)$ is related to the incident laser power P, as well as the gap parameter. The number of quasiparticles excited may be estimated using the coupled Rothwarf-Taylor (1967) rate equations. The steady state number of excited quasiparticles (in normalized units) is:

$$n - n_o = (P\ \tau_{eff})/(4\ \langle E \rangle\ \Delta(0)\ N(0)\ \Omega) \quad (5.13)$$

where τ_{eff} is the effective lifetime of the excitations before recombination occurs and $\langle E \rangle$ is the average energy per quasiparticle Parker, 1975). The lifetime τ_{eff} is itself dependent on the number of quasiparticles. For a quasiparticle to recombine, it must pair with another quasiparticle. The recombination rate for quasiparticles is

simply proportional to the number of combinations of pairs of quasiparticles ($n^2/2$), so the effective recombination time is given by:

$$\tau_{eff} = n\,(dn/dt)^{-1} = b\,\tau_o\,\gamma/n \qquad (5.14)$$

where τ_o is a characteristic time for the superconductor (Kaplan, et al., 1976), b is a dimensionless constant of proportionality (equal to 0.048), and γ is the phonon trapping factor (Kaplan, 1979), which may be on the order of 50 depending on the materials at the interface.

If $n \ll 1$, Δ is independent of n, and equations (5.13) and (5.14) may be solved self-consistently, yielding:

$$n - n_o = \{[\, n_o^2 + P\gamma b\,\tau_o/(\langle E\rangle\,\Delta\,N(0)\Omega\,)]^{1/2} - n_o\}/2 \qquad (5.15)$$

Several limiting cases of Eq. (5.15) are worthy of note. Combining Eqs. (5.15) and (A.12) gives for low incident power:

$$I_o = (2/eR)\,c_1\,P\,\tau_o\,\gamma b/(4n_o N(0)\Omega) \qquad (5.16)$$

The current is simply proportional to the incident laser power, with a coefficient that depends on temperature. For temperature-independent c_1 and γ, this temperature dependence goes as $n_o(T)^{-1}$.

At low temperatures, where $n_o(T)$ becomes small exponentially, the number of laser-excited quasiparticles may exceed the number of thermally excited quasiparticles. For sufficiently large laser power, Eqs. (5.15) and (A.12) lead to

$$I_o \cong (1/eR)\, c_1 \Delta\, (P\gamma\tau_o/N(0)\Omega)^{1/2} \qquad (5.17)$$

The linear thermoelectric current saturates, producing a square root dependence on applied laser power.

In summary, the expected power dependence predicted by this simple Rothwarf-Taylor equation model should be linear for small laser power and moderately large temperatures. For sufficiently low temperature (and therefore small n_o), the predicted thermoelectric current should vary as $P^{1/2}$. For fixed (small) laser power, the temperature dependence of the current should roughly follow $n_o(T)^{-1}$, which increases with decreasing temperature. All of these predictions are based on temperature independent values for γ and c_1.

Chapter VI. THERMOELECTRIC EFFECT MEASUREMENT TECHNIQUES

A. SQUID Circuit

Measurement of the thermoelectric current presented challenging problems in low noise metrology. To measure signals down to 1 pA, at essentially zero voltage, a circuit was designed around a S.H.E. SQUID galvanometer. The quoted current noise for the SQUID system was 20 $pA/(Hz)^{1/2}$. In order to improve upon this noise figure, a superconducting transformer was wound using superconducting NbTi wire. The transformer was surrounded by a lead shield to reduce magnetic pickup from external fields. The in-circuit current gain of the transformer was measured as 14. Use of the computer to average data over 11 second intervals reduced the bandwidth to roughly 0.1 Hz. The total system noise, measured by taking data on a superconducting tunnel junction, was 0.6 pA, which is very close to the theoretical limit of 0.4 pA set by the SQUID-transformer circuit.

The electronic schematic for the SQUID circuit is shown in Fig. 6.1. The SQUID noise bandwidth was limited to about 10^5 Hz by including a 3 ohm parallel resistor, R_p. This acted as a low-pass filter, attenuating all higher frequency signals. The actual laser signal was chopped at 25 or 337 Hz, so the high frequency limit presented no difficulty. Also included in the circuit was a 8×10^{-5} ohm series resistor, R_S, which provided a low frequency rolloff at 3 Hz. This was

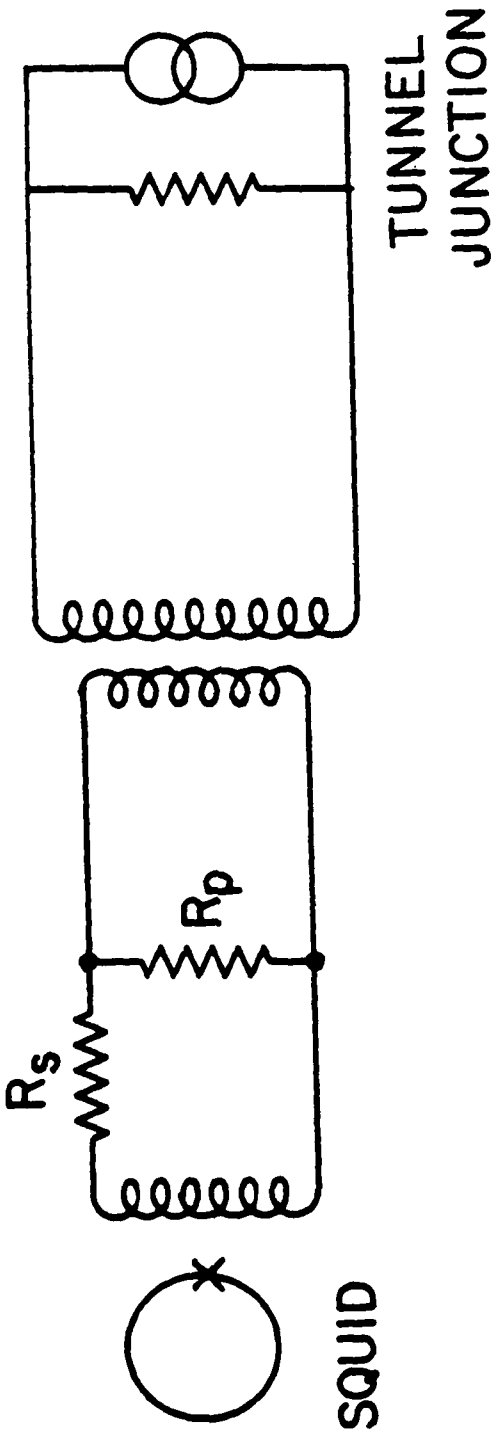

FIGURE 6.1. Detailed electrical schematic of the SQUID coupling circuit.

done to eliminate trapped flux from the SQUID loop. Note that in contrast to the capacitive corrections required for the high impedance experiments described earlier, tunnel junction capacitance has no effect on these low impedance measurements. The SQUID circuit effectively shorts out the capacitance.

The sample geometry was modified slightly from the earlier experiments, and is shown in Fig. 6.2. The tunnel junction (located on the upper end) was somewhat larger, measuring about 5 mm^2. Electrical contacts to the sample were made by the same type of pressure contact mount as was described in chapter 2. At the other end of the sapphire substrate, electrically isolated from the sample junction, a simple aluminum strip was evaporated at the same time that the aluminum was evaporated for the tunnel junction. Four-terminal measurements of the isolated strip were used to determine T_c of the aluminum electrode of the tunnel junction without introducing noise into the junction circuit.

The overall current measurement experiment is diagramed schematically in Fig. 6.3. A chopped laser beam illuminated the tunnel junction, generally from the lead-bismuth side. The tunnel junction was coupled through the superconducting transformer to the SQUID circuit. The SQUID output signal was filtered with an Ithaco electronic filter to remove occasional flux-jump spikes. The output from the filter was then fed into the two lock-in setup described earlier. The computer was programed to sample, average, and record the lock-in output signal in

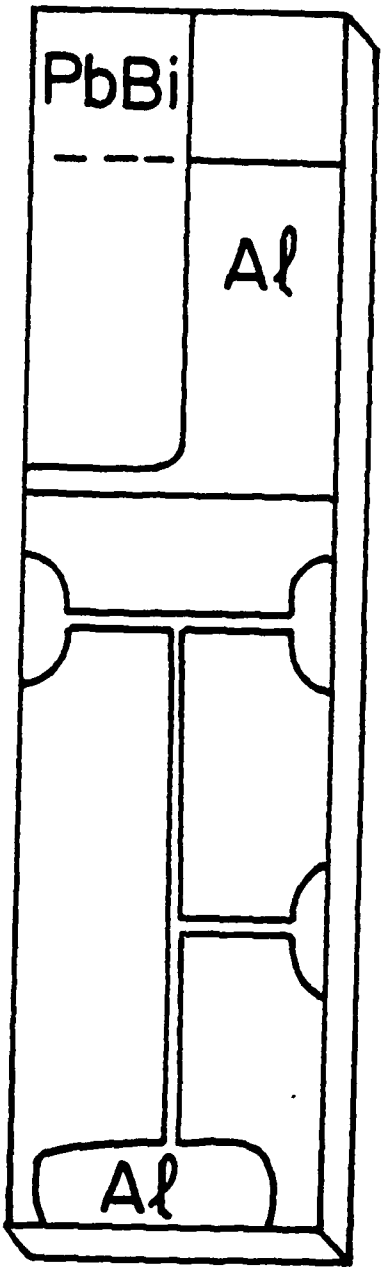

FIGURE 6.2. Tunnel junction layout used for current measurements.

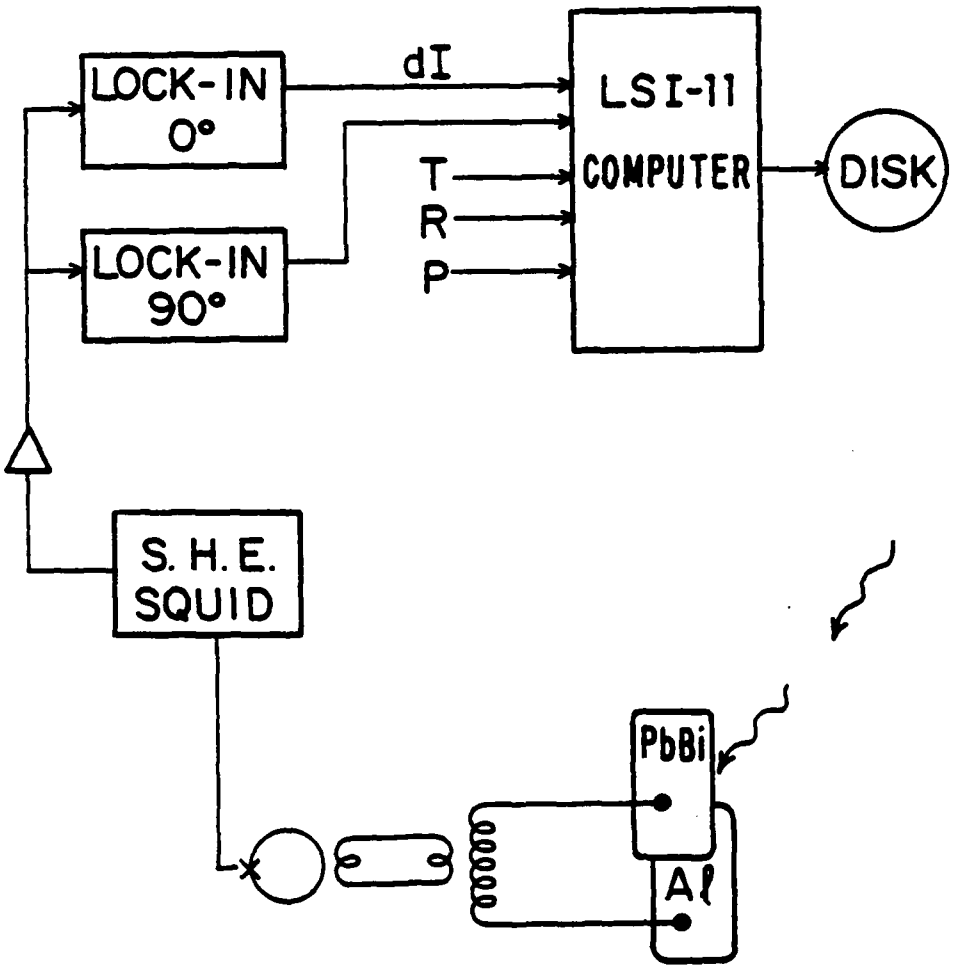

FIGURE 6.3. Schematic diagram of current measurement circuit.

addition to the bath temperature, laser power, and resistance of the aluminum strip. Runs were taken varying either the temperature or laser power.

B. Fiber Optics

The extremely high sensitivity of the SQUID system made careful electronic shielding of the tunnel junction from outside rf noise imperative. Unfortunately, a major source of the rf noise in the laboratory was the electric discharge in the laser tube. Successful simultaneous operation of the SQUID and the laser was found to require keeping the tunnel junction and SQUID in an rf shielded room, while somehow getting the laser beam into the shielded room and down onto the tunnel junction sample.

These difficulties were overcome through the use of an optical fiber. Recent advances in optical fiber technology have produced low loss (<10 dB/km), low cost (~$1/meter), commercially available fiber capable of transporting powers of up to kilowatts in a flexible light pipe. For my requirements, I wanted to be able to transport the laser beam over a distance of roughly 30 meters, without losing more than a factor of ten in optical power. The fiber also had to be able work at

temperatures as low as 1.5 K, without loss of mechanical strength or flexibility.

Several types of optical fibers were considered for use in the experiment. Plastic fibers were ruled out because of their high loss (> 1 dB/meter). Fibers of silica with silicone cladding were unsuitable because the silicone changes its index of refraction at low temperatures, causing the fiber to become quite lossy. A difficulty presented by fiber bundles and composite fibers was differential contraction of the cladding material. At low temperatures the differential contraction causes microbending which leads to high optical losses into the cladding material.

All the above difficulties were avoided by using an all glass fiber made by Corning Glassworks. Corning was generous enough to respond to my request for a small sample by sending 5 km of their Corguide optical waveguide. A length of the fiber was tested in liquid nitrogen, and found to be strong, flexible and almost loss-free.

There were two major constraints to a practical coupling scheme from the laser to the fiber. The first involved the size of the fiber. The optically conducting core of the fiber was only 63 μm in diameter. The nearly parallel laser light could be focussed down to a spot size of $f\lambda$, where f is the f number of the lens system, and λ is the optical wavelength (0.5145 μm). This imposed a constraint that

$$f < 100 \qquad (6.1)$$

It should be understood that this limit is for a very high quality lens. For the more economical lenses actually used, this limit should be scaled down somewhat. In general, the larger f is, the larger the spot size on the fiber.

The second constraint on the laser-fiber coupling scheme was imposed by the limited acceptance angle of the fiber. The index of refraction of the fiber material falls off parabolically away from the center of the channel. This serves to refocus light which is not too greatly off axis. For light inside the fiber core to be totally internally reflected by this refocusing mechanism, the departure from alignment should not exceed the critical angle set by the index of refraction profile of the film. For the Corning Corguide fiber used in this experiment, it was necessary that light hitting the center of the fiber enter from an angle of no more than 0.2 radians (12^{o}). (For light near the edge of the conducting core the critical angle is even smaller.) This imposes a constraint that

$$f \geq 4.7 \qquad (6.2)$$

A tradeoff was made between small spot size and small entrance angle by using a 9 mm focal length lens. For the 1.5 mm diameter laser beam, this

resulted in f/6. Experimentally this was found to couple the power into the fiber most efficiently, for the argon-ion-laser beam. A spot size of 10 μm could be readily obtained and scanned across the end of the fiber using an NRC FB-1 XYZ positioning mount for the fiber.

A practical difficulty in the use of the fiber was that its transparency and small size made it almost invisible. Although the optical fiber was strong enough to support its own weight, as well as take some fairly rough handling, it consistently failed when it was stepped upon. This necessitated running the fiber as close to the ceiling as possible, and hence out of harm's way.

The fiber was run from the XYZ mount up to the ceiling, through a hole in the wall, across another room, through the copper screening of the rf shielded room, and down to the cryostat. At the cryostat it was threaded down a thin teflon tube which was then sealed at the top with putty-like Apiezon Q leak sealant. The teflon tube served to protect the fiber from abrasion. The fiber was positioned above the tunnel junction by teflon-taping it onto a small support rod located on the substrate holder.

The power transmission for the entire system, including 30 meters of fiber, was measured using a thermopile detector at the output end of the fiber. For the optimized system, the total coupling efficiency (defined as the ratio of output from the fiber divided by the laser ouput power)

was 0.65. This compares quite favorably with the theoretical limit of 0.78 imposed by partial reflections (4 percent per surface) at the glass surfaces in the optical path (the beam splitter, the focusing lens and the optical fiber itself).

An added advantage in use of the glass optical fiber over more conventional optical coupling schemes is that the heat leak down the glass is negligible. Based on typical thermal conductivity values of glass (Childs, et al., 1973), the heat leak is estimated to be ~2 μW. In contrast, transverse optical access dewars must necessarily allow a path for at least some blackbody radiation (47 mW/cm^2 at 300K) to enter the sample area, as well as the desired optical radiation.

The optical system is diagramed schematically in Fig. 6.4. The laser output power could be regulated from 50 mW to 500 mW. For lower powers, a 10 dB attenuater was inserted into the beam path. A glass beamsplitter reflected about 8 percent of the light onto a silicon photodiode detector. The rest of the beam was chopped at 337 Hz (a particularly low noise frequency for lock-in detection), then focused down onto the core of the optical fiber. The chopper generated an electrical signal which was used to synchronize the two lock-ins.

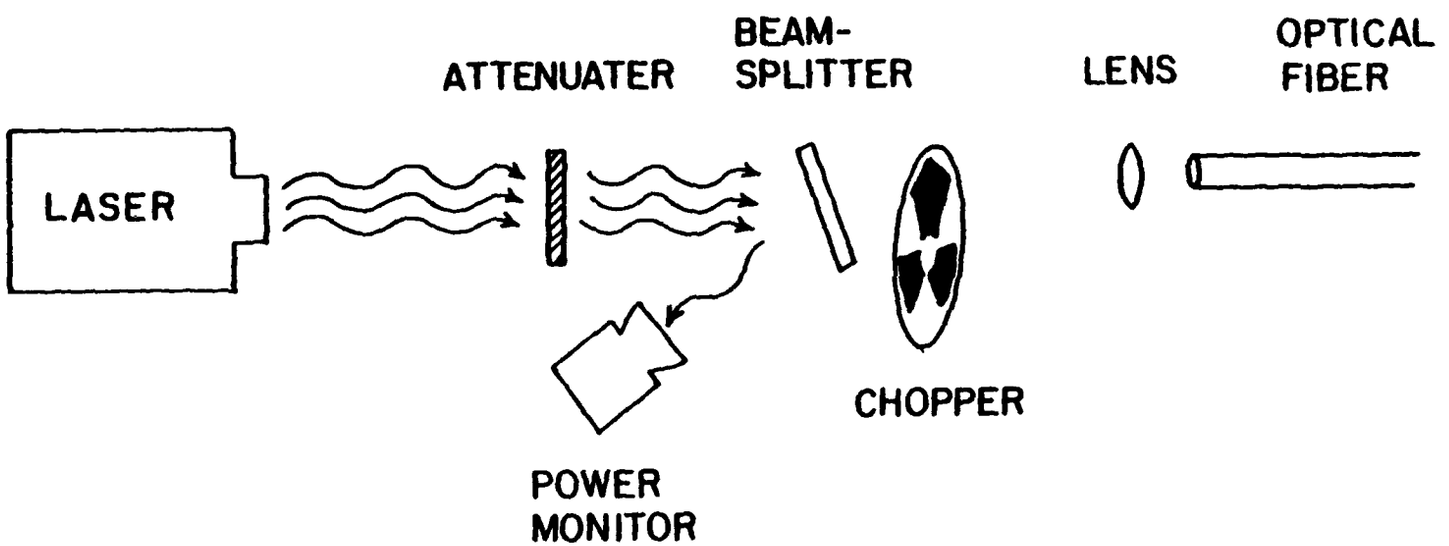

FIGURE 6.4. Diagram of the optical path from the laser to the optical fiber.

AD-A089 520 HARVARD UNIV CAMBRIDGE MA DIV OF APPLIED SCIENCES F/G 9/3
NONEQUILIBRIUM SUPERCONDUCTIVITY IN OPTICALLY ILLUMINATED TUNNE--ETC(U)
AUG 80 A D SMITH N00014-77-C-0085
UNCLASSIFIED TR-17 NL

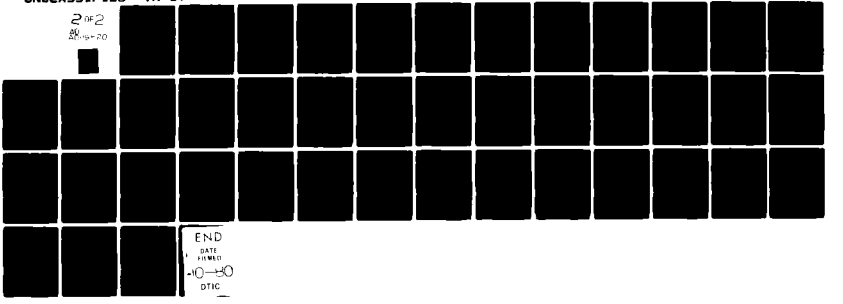

VII. THERMOELECTRIC EFFECT RESULTS AND DISCUSSION

A. Voltage Dependence Measurements

A test for the existence of a thermoelectric effect in tunnel junctions was first performed by using the voltage measurement scheme described in Chapter II. The data used for the unfolding analysis could be used to search for a tunneling thermoelectric effect. Illuminating the tunnel junction from the lead-bismuth side causes two observable effects in the tunnel junctions. The first is a general increase in the tunneling conductance, caused by the larger number of excited quasiparticles (see earlier chapters). For constant current biasing, this leads to a contribution to the observed $|dV|$ which is an even function of voltage, and is defined as the symmetric contribution. (The sign of dV reverses near the origin.) Of more concern here, is the thermoelectric contribution to $|dV|$. The thermoelectric current through the tunneling barrier should be only weakly voltage dependent, as is clear from the argument leading to Eq. (5.5). For a fixed current bias, the thermoelectric current, I_o, must be countered by a decrease in the conventional quasiparticle current. This gives rise to an observable shift in the junction voltage given by:

$$dV = dV/dI\ I_o \qquad (7.1)$$

where dV/dI is the dynamic resistance of the tunnel junction.

Typical behavior of $|dV|$ is shown in Fig. 7.1. The absolute value of dV is plotted to show the asymmetry, expecially at low voltages. The observed voltage shift $|dV(V)|$ could be decomposed into a symmetric $dV^s(V)$, and an anti-symmetric $dV^a(V)$. The values of dV^s were used in the unfolding analysis, and will not be further discussed here. The measured anti-symmetric contribution is plotted in Fig. 7.2. The falloff in dV^a for large voltages corresponds to the decrease in the dynamic resistance of the tunnel junction at high voltages, and is expected from Eq. (7.1). Fig. 7.3 shows the asymmetry plotted as a function of the dynamic resistance of the junction for one tunnel junction at a fixed bath temperature. The straight-line fit, corresponding to a voltage-independent thermoelectric current of $I_o = 0.91$ nA, is good to within the accuracy of the data.

An estimate for c_1 can be obtained by comparing the observed thermoelectric current to theory (Eq. (A.12)). A value of $\delta\Delta_{PbBi}$ was estimated by measuring the shift in the $\Delta_{PbBi} + \Delta_{Al}$ current jump location on the I(V) curve. (See Chapter IV. for details on this type of calculation.) The inferred value of $\delta\Delta_{PbBi}$ was then used to calculate the extra quasiparticle density in the lead-bismuth according to

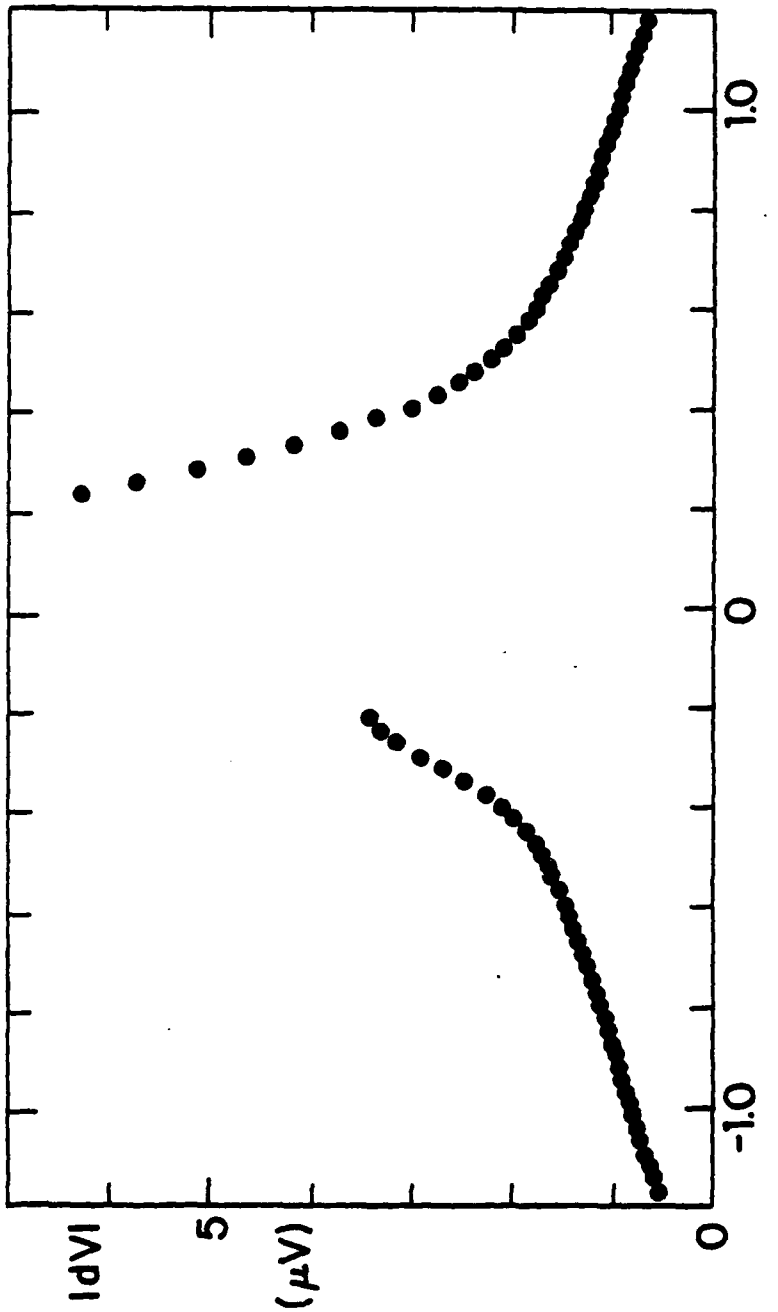

FIGURE 7.1. Observed laser-induced voltage shift $|dV|$ vs. V for an Al-PbBi tunnel junction illuminated on the PbBi side. The temperature was 1.588 K.

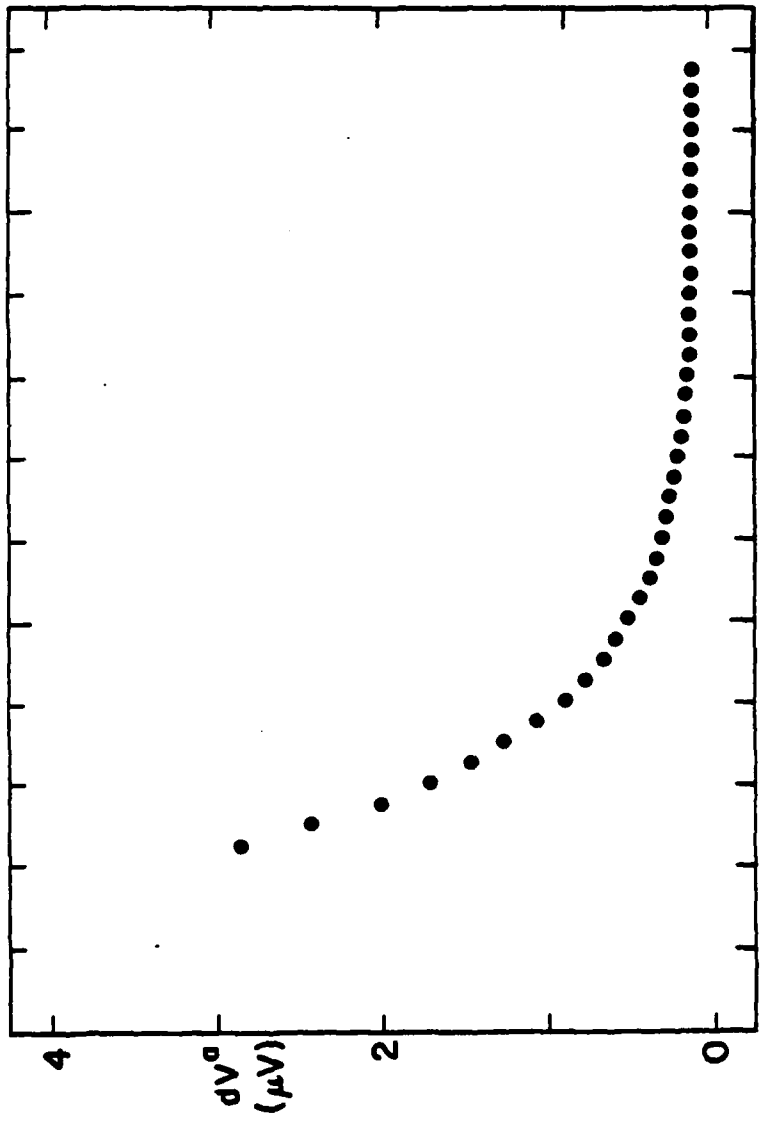

FIGURE 7.2. Measured dV^a vs. V for data shown in Fig. 7.1.

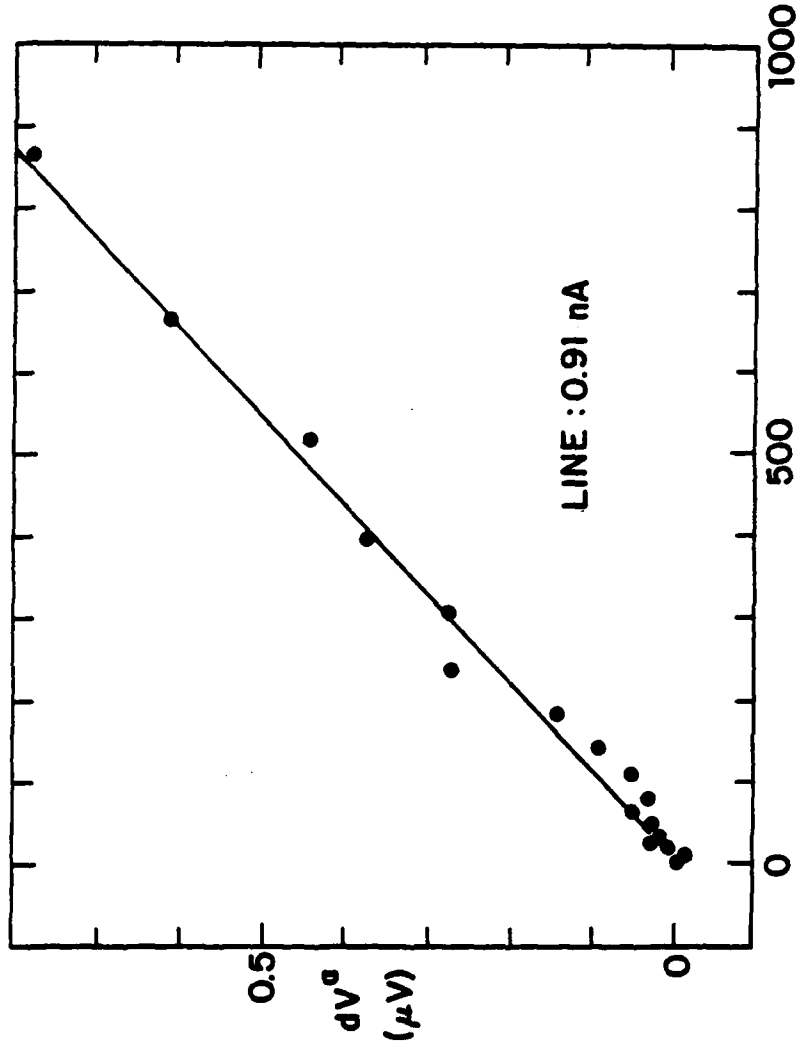

FIGURE 7.3. Observed dV^a vs. dV/dI, the (voltage dependent) dynamic resistance of the tunnel junction. The straight line is the best fit to a constant thermoelectric current model.

$$\Delta/\Delta(0) = 1 - 2n \qquad (7.2)$$

The aluminum film has a relatively small increase in the density of quasiparticles with sufficiently high energy to tunnel ($E \geq \Delta_{PbBi}$). For the observed thermoelectric currents and the value of δn_{PbBi} implied by $\delta\Delta_{PbBi}$, values of 0.09 - 0.40 eV^{-1} were obtained for c_1. These estimates are an order of magnitude less than the 3.1 eV^{-1} predicted by the one-band model (Eq. (5.6)), but the direction of the discrepancy is in qualitative agreement with the two-band corrections of Gundlach (1973).

B. SQUID Measurements

The voltage measurement techniques are not convenient for detailed measurements of the thermoelectric effect. To measure the power and temperature dependence of the thermoelectric effect, the SQUID system described in Chapter VI. was used to provide direct measurement of the zero-voltage thermoelectric current, I_o.

Results for a sweep in temperature, with constant (small) laser power, are shown in Fig. 7.4. The sample temperature was initially at 3 K and the temperature was reduced eventually to roughly 1.6 K. The current became larger as T (and hence $n_o(T)$) decreased, as expected from

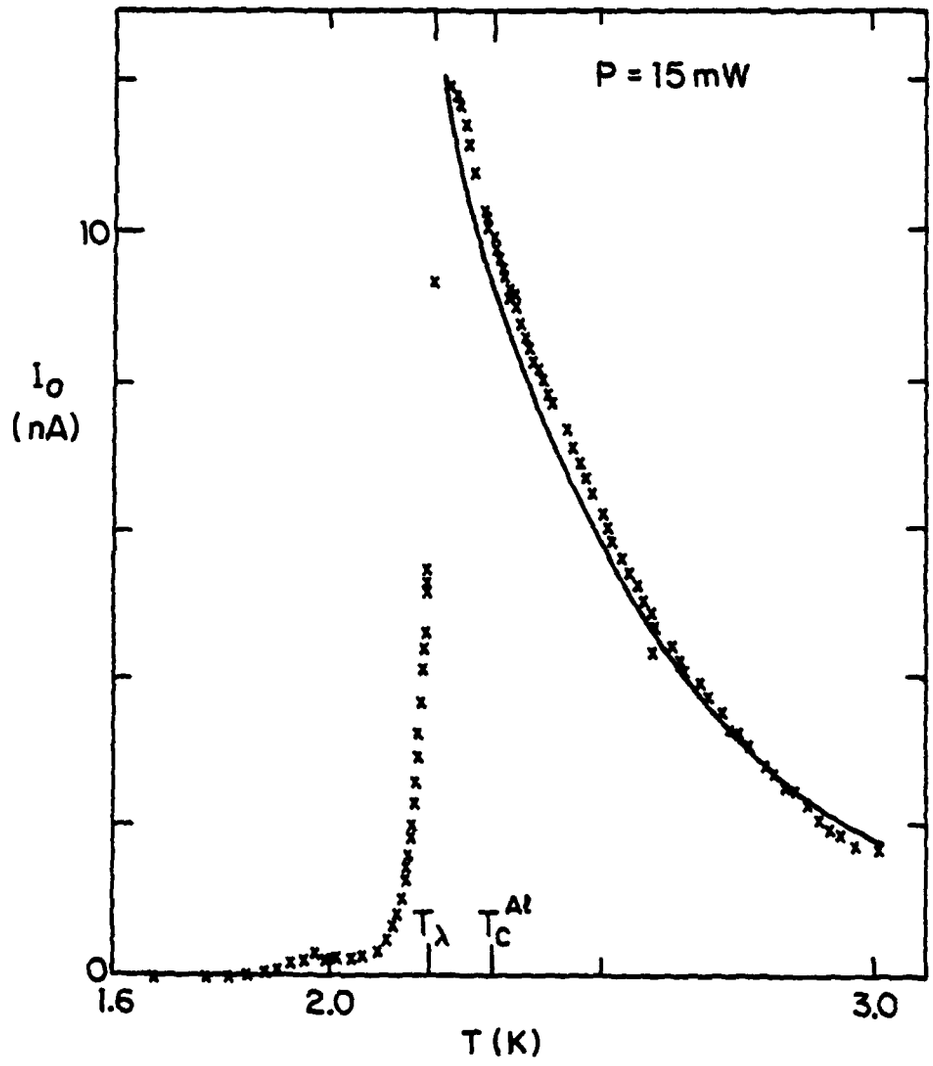

FIGURE 7.4. Observed I_o vs. bath temperature. The incident laser power was held fixed at 15 mW.

Eq. (5.16). There was no noticeable change observed upon passing through T_c of the dirty aluminum film. The solid curve is proportional to $n_o(T)^{-1}$, as my model prodicts. The fit is good for temperatures above the lambda point of helium. At the lambda point there was an abrupt decrease in the measured signal. This is attributed to the improved coupling of phonons to the now superfluid bath, and the resultant decrease in τ_{eff}. At a temperature near 1.85 K the signal disappeared to the limits of resolution (1 pA) of the experiment. This temperature corresponded to that at which the Josephson supercurrent became large enough to be observed in a separate experiment in which current and voltage leads were attached to the sample. Accordingly, I interpret the disappearance of the external thermoelectric current as due to its being effectively shorted out by an internal backflow of supercurrent. This interpretation is supported by the fact that at nonzero voltages, where there is no dc supercurrent, a thermoelectric current is measured in the experiments reported in section A., even at temperatures as low as 1.5 K.

The SQUID galvanometer experiment was also performed at fixed temperature while varying the laser power P. Fig. 7.5 shows the power dependence of I_o for several temperatures. As expected, the observed currents become nonlinear in power for the lower temperatures.

Fig. 7.6 shows the predictions for my simple model (Eq. (5.15)). The value of c_1 and the value of the phonon trapping factor have been adjusted to give a best fit. For an assumed film optical absorptivity of

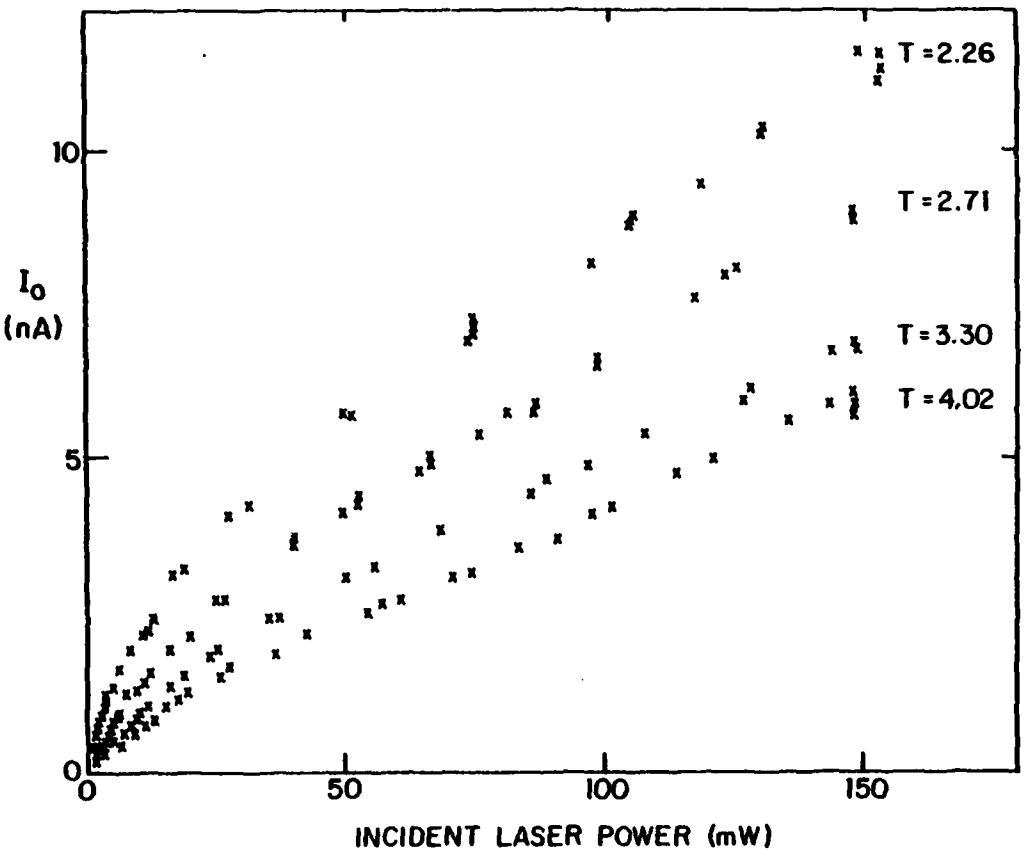

FIGURE 7.5. I_o vs. incident laser power for 4 fixed temperatures, all above the helium lambda point.

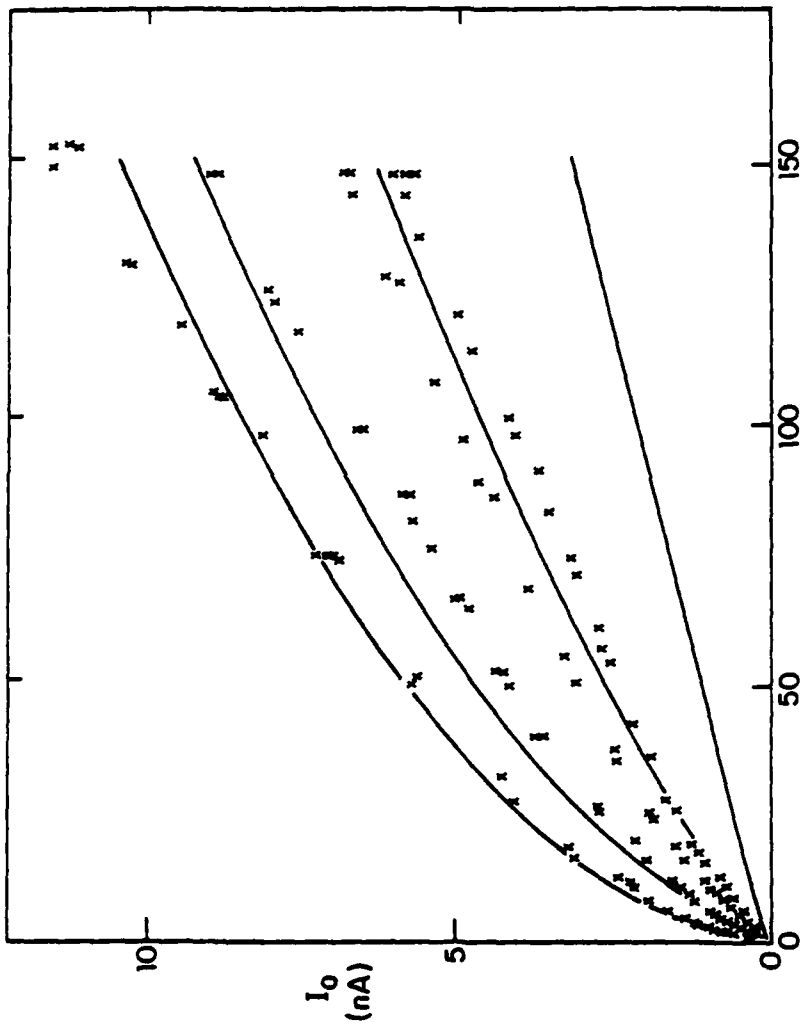

FIGURE 7.6. Fit of previous data to theory. Two adjustable parameters (c_1 and γ) were chosen to fit all plotted data.

2 percent, and τ_o of 4.3 X 10^{-11} sec., the fit value of γ is 15. As before, the fit values of c_1 (~0.5 eV^{-1}) are an order of magnitude less than predicted by the one band model calculation (Eq. (5.5)), but are in qualitative agreement with the two band corrections proposed by Gundlach (1973). While the general magnitude, shape, and sign of the $I_o(T)$ curves are in good agreement with the simple Rothwarf-Taylor calculations done here, the exact temperature dependence was less satisfactory. No attempt has been made to include liquid helium effects which would cause a temperature dependence to the phonon trapping factor. Available literature suggests that heat transport through helium is strongly dependent on the exact sample geometry and surface structure, and is therefore difficult to calculate realistically. The importance of the liquid helium in determining phonon trapping factor is evidenced by the dramatic decrease in I_o as the helium becomes superfluid.

For a given temperature, the adequacy of the Rothwarf-Taylor model to describe the energy relaxation within the superconductor is quite good. Fig. 7.7a shows the measured behavior of $I_o(P)$ in the low temperature regime. The accuracy of the $P^{1/2}$ power dependence is emphasized in Fig. 7.7b, where $I_o^2(P)$ is plotted for the same data. The straight-line behavior indicates that the self-consistent Rothwarf-Taylor solution for the number of excited quasiparticles fits the experimental situation very well.

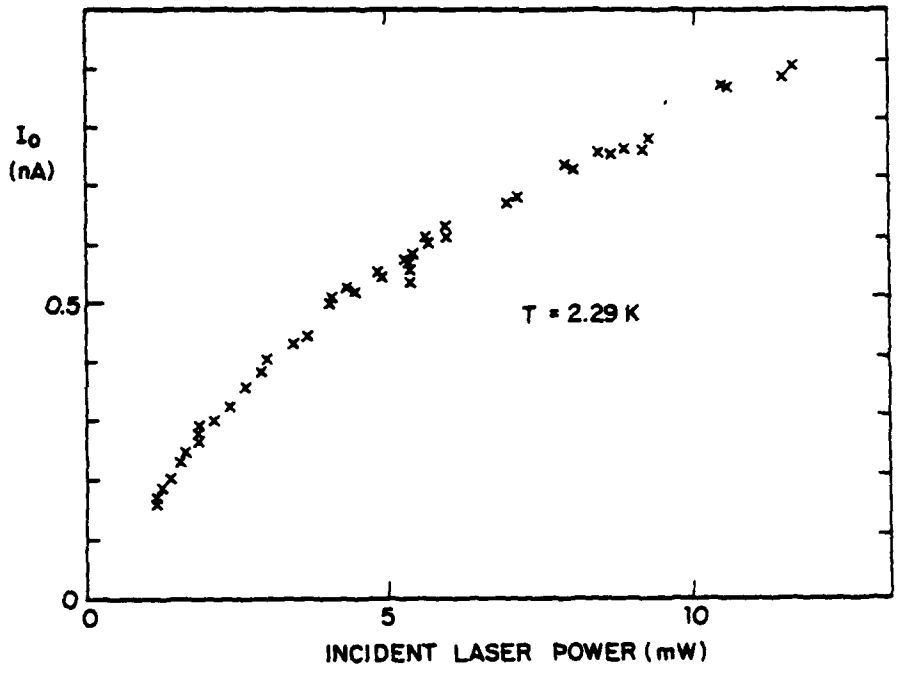

(7.7a)

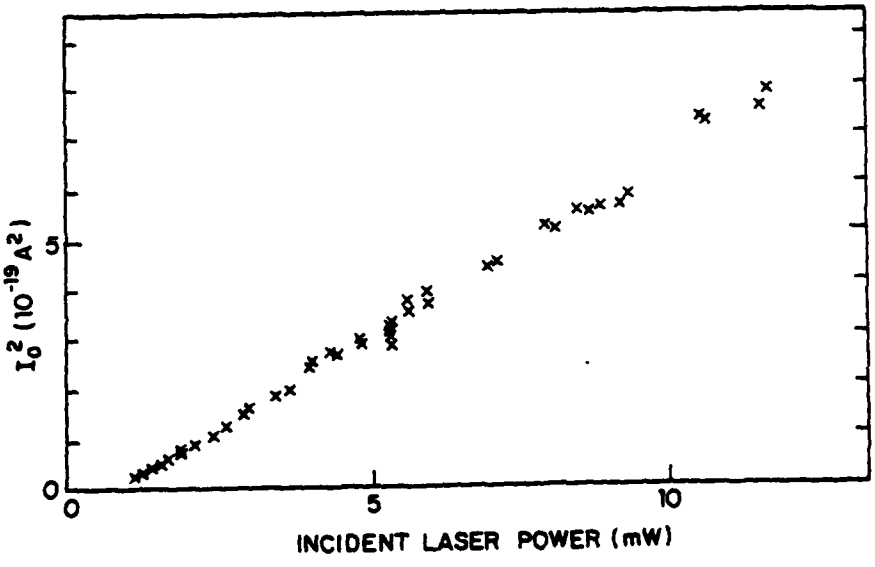

(7.7b)

FIGURE 7.7. Plots of I_o vs. P and $I_o^{1/2}$ vs. P for an Al-PbBi tunnel junction at 2.29 K.

C. Comparisons with Point Contact Experiments

The existence of a thermoelectric current across tunneling junctions explains several key discrepencies between earlier experiments and existing theory. In particular, it is useful to examine the experiments of Clarke and Freake (1972) in light of temperature gradients across oxide barriers. Their experiment consisted of a point contact formed by bringing a sharpened Pb wire into contact with a Pb foil. The temperatures of the wire and the foil could be independently varied and measured. Although the point contact supercurrent effectively shorted out any thermoelectric current, it was possible to measure the difference in the magnitude of the critical current for the two directions of current flow. This asymmetry was interpreted in terms of a thermoelectic quasiparticle current. Clarke and Freake measured a sizeable current whenever the point and foil were at different temperatures, although the size of the effect varied over a factor of 50 for different point contacts. The existence of any asymmetry current was surprising to those who expected no steady-state thermoelectric current to be possible within a superconducting channel.

In an effort to clarify matters, Welker and Bedard (1977) performed a somewhat similar experiment using Nb wire. They were extremely careful about sample preparation conditions. For very clean, oxide-free point contacts, where a small but continuous superconducting channel could be

assumed to exist, they found no evidence for a thermoelectric current. If they allowed an oxide to form in the point contact area, however, they did note a significant thermoelectric current. The deduced current was in the same direction relative to the temperature difference as was observed by Clarke and Freake, although Nb and Pb have thermopowers which differ in sign. Thus, the thermoelectric voltage was of the wrong sign to be predicted by the thermopower arguments of Clarke and Freake, but is correctly predicted by our model.

A follow up experiment by Matsinger et al. (1978) was performed using both Nb and Pb point contacts. Asymmetry was looked for over the entire I(V) curve of the point contacts, for both directions of applied temperature gradient. For situations where one electrode was raised above its T_c, while the other electrode was superconducting, they measured the expected normal thermopower. With both metals below T_c no asymmetry was observed to the limit of their sensitivity. Matsinger, et al. concluded that the Clarke and Freake measurements were "caused by a surface layer," and were not an intrinsic superconducting effect.

It seems likely that the asymmetric critical currents measured both by Clarke and Freake and by Welker and Bedard are the result of thermoelectric currents across oxide barriers. The sign predicted here for tunneling barrier thermoelectric currents agrees with experimental results. The magnitude of the predicted effect can be calculated using the point contact parameters given in the Clarke and Freake paper.

Integrating Eq. (A.16) numerically for Pb electrode temperatures of 7.0 and 5.3 K gives:

$$I_o = (2/eR)\, c_1 \quad (0.08\, \Delta^2) \qquad (7.3)$$

where Δ is the lead gap at 5.3 K. Estimating c_1 is not as simple as for our experimental geometry. For Pb tunnel junctions, Basavaiah et al. (1974) have measured the oxide barrier height as 1.05 eV. The actual junction area is somewhat poorly defined for a point contact. If a 1 μm^2 area is assumed, and the junction resistance is 1 ohm, then $c_1 \cong 4\ eV^{-1}$ and

$$I_o^{theory} = 0.7\ \mu A \qquad (7.4)$$

If the junction effective area is larger, the prediction is logarithmically larger. If not all the temperature difference occurs at the oxide, a smaller I_o should result. Given the variance in the experimental results, uncertainties in several of the barrier parameters, expecially A and ϕ, and the tendency of the one-band approximation to overestimate c_1, this is in good agreement with the plotted Clarke and Freake result

$$I_o^{experiment} = 0.25\ \mu A \qquad (7.5)$$

(Note that their experimental result has been adjusted by a factor of two because the published values are peak-to-peak.) Coincidentally, the expected normal state thermoelectric current for the point contact is the same order of magnitude, 0.4 μA. The two mechanisms are entirely independent; the mechanism reported here is an oxide effect, dependent on the barrier height and thickness, while the Seebeck effect depends on the metallic density of states of the electrode materials.

VIII. CONCLUSION

In summary, the study of optically illuminated Al-PbBi tunnel junctions has proven to be effective in the study of properties of nonequilibrium superconducting films. A general procedure for unfolding I(V) measurements of asymmetric tunnel junctions has been developed as a tool for measuring the quasiparticle energy distribution. Absolute sensitivity of 10^{-5} and relative accuracy of a few percent are readily obtainable for small perturbations from equilibrium. Results of unfolding experimental data from optically illuminated Al-PbBi tunnel junctions show that the aluminum nonequilibrium state is well described by a T^* model behavior over several orders of magnitude in f(E).

The enormous temperature gradients present across illuminated tunnel junctions (up to 10^7 K/cm) lead to the study of thermoelectric effects in tunnel junctions. For nonequilibrium situations in which a temperature difference exists across a tunneling barrier, I have shown the existence of a thermoelectric current, which exists even with no voltage difference across the oxide. This current results from the energy dependence of the electronic tunneling probability for barrier penetration, and is largely independent of material parameters of the electrode materials. I have measured this thermoelectric effect in an open circuit experiment as well as with a current measurement scheme. In both cases the data are in at least qualitative agreement with theoretical predictions.

The existence of the tunneling thermoelectric current can explain the supercurrent asymmetries studied in point contact experiments by a number of authors. The theory presented here correctly predicts the sign and magnitude for these asymmetries, as well as the absence of any asymmetry in very clean point contacts.

In addition, the temperature dependence and power dependence of the thermoelectric effect can be used as a probe of the nonequilibrium superconducting state. The thermoelectric current effectively measures the density of excited quasiparticles. The thermoelectric effect was studied in both the linear, weak perturbation regime and in the highly non-linear regime far from equilibrium. In both cases the behavior of the superconductor was well described by a self-consistent solution to the Rothwarf-Taylor equations.

In conclusion, the study of the I(V) characteristics of tunnel juncitons has helped to provide insight into a variety of nonequilibrium superconducting phenomena. It is my hope that the tools developed here will find future uses in exploring the superconducting state.

APPENDIX I. UNFOLDING PROGRAM

```
C         ASYMMETRIC JUNCTION UNFOLDING PROGRAM
C         WRITTEN BY ANDY SMITH
C         LINES BEGINNING WITH C ARE COMMENTS
C         LINES BEGINNING WITH D ARE IGNORED EXCEPT WHILE DEBUGGING
        COMMON /DEBUG/IDBG(2)
        COMMON Y(100)
        DIMENSION COEFFS(20),VEES(100),C(21)
        DIMENSION OBS(21,100),A(20),STDA(20)
C         INPUT FORMAT
C         LINE NO.
C         1          BLANKS UNLESS DEBUGGING
C         2          LARGER GAP, SMALLER GAP (MEV), TEMPERATURE (K),
C                    RESISTANCE (OHMS)  ALL FLOATING POINT NUMBERS
C         3-8        ENERGY BIN LIMITS (21 VALUES, 4 PER LINE)
C         9-         VOLTAGE (MV),CURRENT (MA) DATA, 1 PAIR PER LINE
C         OUTPUT IN FILE 1 CONTAINS BEST FIT F-TWIDDLE VALUES,
C         UNCERTAINTIES IN FIT VALUES, AND FINALLY DATA WITH FIT
        COMMON /PRAM/V,TEMP,DELTAA,DELTAS,E(21)
        READ(20,110)IDBG
  110   FORMAT(5I1)
        READ(20,2)DELTAS,DELTAA,TEMP,RESIST
        WRITE(1,2) DELTAS,DELTAA,TEMP,RESIST
        READ(20,34)E
        WRITE(1,35)E
   35   FORMAT(4F7.3)
        DO 36 K=1,21
   36   E(K)=E(K)/DELTAS
   34   FORMAT(4F)
        DO 1 NOBS=1,100
   52   READ(20,2,END=6)V,CURENT
        CURENT=CURENT*RESIST
        IF(V.LT.DELTAS-DELTAA)GO TO 50
        TYPE 51,NOBS
   51   FORMAT(' ATTEMPT TO USE VOLTAGE TOO HIGH ON OBS ',I5)
        GO TO 52
   50   VEES(NOBS)=V
C         ENTER DATA AND G VALUES
        CALL CRANK2(C)
        DO 3 KVAR=1,20
    3   OBS(KVAR,NOBS)=C(KVAR)
        OBS(21,NOBS)=CURENT
    1   CONTINUE
    6   NOBS=NOBS-1
        WRITE(22,37)(((OBS(MM,M),MM=1,21),VEES(M)),M=1,NOBS)
C         IS THERE ENOUGH DATA?
        IF(NOBS.GE.21)GO TO 55
        TYPE 56,NOBS
   56   FORMAT(' ONLY ',I5,' DATA POINTS ')
```

```
      STOP
   55 CONTINUE
    2 FORMAT(4F)
C     MAYBE I SHOULD CHECK FOR FIT WITH
C     A PARALLEL CONDUCTANCE AS ONE OF THE BINS
C       IF SO, REPLACE LAST BIN BY CONDUCTANCE
      IF( IDBG(2) .NE. 1) GO TO 120
      DO 121 K=1,NOBS
  121 OBS(20,K)=VEES(K)
  120 CONTINUE
   37 FORMAT(6E13.4)
C       DO THE JOB
      CALL FITIT(OBS,NOBS,21,Y,COEFFS,STDA)
      WRITE(1,10)COEFFS,STDA
      CHI=0.
      DO 77 K=1,NOBS
      CHI=CHI+(OBS(21,K)-Y(K))**2/OBS(21,K)**2
   77 WRITE(1,10)VEES(K),OBS(21,K),Y(K)
      STDDEV=SQRT(CHI/FLOAT(NOBS-21))
      WRITE(1,10) STDDEV
   10 FORMAT(2X,5E11.4)
   25 FORMAT(1X,5E12.3)
   27 FORMAT(5E15.6)
      STOP
      END
      SUBROUTINE CRANK2(OUT)
C       AT A GIVEN VOLTAGE, CALL ROUTINES TO CALCULATE ALL OF THE
C       G VALUES
      COMMON /PRAM/VREAL,TEMP,DELTAA,DELTAS,E(21)
      COMMON VD,BD,DADB2,X,Y
      DIMENSION OUT(11 )
      BD=11.6*DELTAS/TEMP
      VD=VREAL/DELTAS
      DADB2=(DELTAA/DELTAS)**2
      OUT(21)=0
  999 FORMAT(I4)
      DO 3 K=1,20
 8811 FORMAT(5F10.3)
      OUT(K)=DELTAS*CCC(E(K),E(K+1))
    3 OUT(21)=OUT(21)+OUT(K)
      CONTINUE
    2 CONTINUE
    4 FORMAT(11E10.3)
      RETURN
      STOP
      END
      FUNCTION CCC(EMIN,EMAX)
C       COMPUTE G VALUE FOR A GIVEN ENERGY RANGE
```

```
      EXTERNAL CO
C     CONTRIBUTION FROM QUASIPARTICLES WITHIN ENERGY RANGE
      COMMON VD,BD,DADB2,KI,TZERO
      DIMENSION POINT(4)
 101  FORMAT(F10.3,I5,F10.3)
      TOTAL=0.
      ITYPE=0
 100  FORMAT(5F10.3,I5,F10.3)
 888  FORMAT(I5)
C       TEST LIMITS OF INTEGRATION
      POINT(1)=1.-VD
      POINT(2)=1.
      POINT(3)=1.+VD
      POINT(4)=AMAX1(1.+8./BD,POINT(3)+1.)
      DO 1 K=1,3
C     DIVIDE INTO REGIONS
      KI=K
      E1=AMAX1(POINT(K),EMIN)
 103  FORMAT(5F10.4)
C       AVOID SINGULARITIES
      IF(E1.GT.EMAX)GO TO 99
      IF(E1.GT.POINT(K+1))GO TO 1
      E2=AMIN1(EMAX,POINT(K+1))
      T1=SQRT(E1-POINT(K))
      T2=SQRT(E2-POINT(K))
      TZERO=POINT(K)
      ADDIN=SIMPSN(CO,T1,T2,22)
      TOTAL=TOTAL+ADDIN
      IF(ITYPE.EQ.1)TYPE 106,VD,KI,E1,E2,T1,T2,ADDIN
 106  FORMAT(F5.2,I5,4F6.3,E10.3)
   1  CONTINUE
  99  CCC=2.*TOTAL
      RETURN
      END
      FUNCTION CO(T)
C     DADB2<1.
      COMMON VD,BD,DADB2,KI,TZERO
C     ALL ENERGIES EXPRESSED FOR LARGER DELTA
      ENT(X)=X/SQRT(X+1.)
      EN2(X)=X/SQRT(X**2-DADB2)
      EN1(X)=X/SQRT(X**2-1.)
      E=T**2+TZERO
 102  FORMAT(3F10.4,I6)
      CO=0.
C     SWITCH
      GO TO (1,2,3),KI
    3 CO=-ENT(E-VD)*EN2(E)+
     + T*EN1(E)*(EN2(E+VD)-EN2(E-VD))+
```

```
     +  T*EN1(E+VD)*EN2(E)
        GO TO 9
     2  CO=ENT(E)*(EN2(E+VD)-EN2(E-VD))+
     +  T*EN1(E+VD)*EN2(E)
        GO TO 9
     1  CO=CO+ENT(E+VD)*EN2(E)
     9  CO=CO/(1.+EXP(E*BD))
        RETURN
        END
C       THIS PROGRAM IS CALLED BY THE MAIN PROGRAM
C       GIVEN DATA, IT LOADS THE DATA AND CROSS-CORRELATES
C       IT THEN CALLS A MATRIX INVERSION SUBROUTINE TO UNFOLD
        SUBROUTINE FITIT(OBS,NOBS,NVAR,Y,A,STDA)
        COMMON /DEBUG/IDEBUG
        DOUBLE PRECISION ALPHA,DET,WA,WB
        DIMENSION ALPHA(20,20),BETA(20),STORE(20,20)
        DIMENSION SHOWIT(20),OUTPT(20)
        DIMENSION WA(35),WB(35)
        DIMENSION OBS(NVAR,NOBS),A(20),STDA(20),Y(NOBS)
        WGT(IOBSVR)=1./OBS(NVAR,IOBSVR)**2
        MVAR=NVAR-1
        TYPE 60
    60  FORMAT(' ENTERRED FITIT ')
        DO 1 KV=1,MVAR
        DO 2 LV=KV,MVAR
        SUM=0
C       CALCULATE CROSS CORRELATION MATRIX
        DO 3 IIOBS=1,NOBS
        IOBS=IIOBS
     3  SUM=SUM+ OBS(KV,IOBS)*OBS(LV,IOBS)*WGT(IOBS)
        ALPHA(KV,LV)=SUM
     2  ALPHA(LV,KV)=SUM
     1  CONTINUE
D       WRITE(23,55) OBS
D       WRITE(23,55) ZERO
D       WRITE(23,55)ALPHA
        TYPE 61
C       SET UP BETA COEFFICIENTS
    61  FORMAT(' SETTING UP BETA COEFFICIENTS')
        DO 4 KV=1,MVAR
        SUM=0.
        DO 5 IIOBS=1,NOBS
        IOBS=IIOBS
     5  SUM=SUM+OBS(KV,IOBS)*OBS(NVAR,IOBS)*WGT(IOBS)
     4  BETA(KV)=SUM
        DO 6 KA=1,MVAR
        DO 6 KB=1,MVAR
     6  STORE(KA,KB)=ALPHA(KA,KB)
```

```
C       CALCULATE EPSILON MATRIX
        TYPE 63
   63   FORMAT(' INVERTING')
        CALL MATINV(ALPHA,MVAR,DET,WA,WB)
D       WRITE(23,55)ALPHA
        ZERO=0.
D       WRITE(23,55) ZERO
D       WRITE(23,55) BETA
   55   FORMAT(1X,5E11.3)
        DO 8 KVAR=1,MVAR
        A(KVAR)=0
        DO 8 LVAR=1,MVAR
    8   A(KVAR)=A(KVAR)+ALPHA(KVAR,LVAR)*BETA(LVAR)
        SUMB=0.
        DO 10 IOBS=1,NOBS
        SUM= .0
        DO 9 IVAR=1,MVAR
    9   SUM=SUM+A(IVAR)*OBS(IVAR,IOBS)
        Y(IOBS)=SUM
   10   SUMB=SUMB+(SUM-OBS(NVAR,IOBS))**2*WGT(IOBS)
        VARNCE=SUMB/FLOAT(NOBS-NVAR)
C
C       THIS IS THE NEW STANDARD DEVIATION SECTION
C
        DO 200 KVAR=1,MVAR
        STDA(KVAR)=0.
        DO 202 IOBS=1,NOBS
        SUM=0.
        DO 201 LVAR=1,MVAR
  201   SUM=SUM+ALPHA(KVAR,LVAR)*OBS(LVAR,IOBS)
        SUM=SUM*WGT(IOBS)
C       SUM IS NOW DIJ, THE MATRIX RELATING F TO I
        STDA(KVAR)=STDA(KVAR)+(SUM*(Y(IOBS)-OBS(NVAR,IOBS)))**2
  202   CONTINUE
  200   STDA(KVAR)=SQRT(STDA(KVAR))
    70  CONTINUE
        TYPE 111,IDEBUG
   111  FORMAT(' IDEBUG IS ',I5)
        IF (IDEBUG .NE. 1)RETURN
C       NORMALIZE CROSS-CORRELATIONS
        WRITE(24,100)
   100  FORMAT(' NORMALIZED CROSS CORRELATION ')
   101  FORMAT(X,21F6.2)
        DO 102 K=1,20
        DO 103 L=1,20
   103  OUTPT(L)=STORE(K,L)/SQRT(ABS(STORE(K,K)*STORE(L,L)))
   102  WRITE(24,101) OUTPT
        WRITE(24,123)
```

```
  123   FORMAT(' FRACTIONAL CONTRIBUTIONS ')
C       FRACTIONAL CONRIBUTIONS
        DO 104 IIOBS=1,NOBS
        IOBS=IIOBS
        DO 105 K=1,20
        SUM=0.
        DO 106 L=1,20
  106   SUM=SUM+ALPHA(K,L)*WGT(IOBS)*OBS(L,IOBS)
  105   OUTPT(K)=SUM/A(K)*OBS(21,IOBS)
  104   WRITE(24,101)OUTPT
   72   FORMAT(I5,10F7.4)
        RETURN
        END
        SUBROUTINE MATINV(A,N,D,L,M)
C         MATRIX INVERTER
C       ARGUMENTS IN ORDER ARE:
C       INPUT MATRIX (DESTROYED IN COMPUTATION)
C       DIMENSIONALITY OF MATRIX
C       DETERMINANT OUTPUT
C       WORK VECTOR LENGTH N
C       WORK VECTOR LENGTH N
C       MODIFIED FOR DOUBLE PRECISION
        IMPLICIT DOUBLE PRECISION (A-H,O-Z)
        DIMENSION A(1),L(1),M(1)
        D=1.
        NK=-N
        DO  80 K=1,N
        NK=NK+N
        L(K)=K
        M(K)=K
        KK=NK+K
        BIGA=A(KK)
        DO 20 J=K,N
        IZ=N*(J-1)
        DO 20 I=K,N
        IJ=IZ+I
   10   IF(DABS(BIGA)-DABS(A(IJ))) 15,20,20
   15   BIGA=A(IJ)
        L(K)=I
        M(K)=J
   20   CONTINUE
        J=L(K)
        IF(J-K) 35,35,25
   25   KI=K-N
        DO 30 I=1,N
        KI=KI+N
        HOLD=-A(KI)
        JI=KI-K+J
```

```
      A(KI)=A(JI)
   30 A(JI)=HOLD
   35 I=M(K)
      IF(I-K) 45,45,38
   38 JP=N*(I-1)
      DO 40 J=1,N
      JK=NK+J
      JI=JP+J
      HOLD=-A(JK)
      A(JK)=A(JI)
   40 A(JI)=HOLD
   45 IF(BIGA) 48,46,48
   46 D=0.
      RETURN
   48 DO 55 I=1,N
      IF(I-K) 50,55,50
   50 IK=NK+I
      A(IK)=A(IK)/BIGA*-1.
   55 CONTINUE
      DO 65 I=1,N
      IK=NK+I
      HOLD=A(IK)
      IJ=I-N
      DO 65 J=1,N
      IJ=IJ+N
      IF(I-K) 60,65,60
   60 IF(J-K) 62,65,62
   62 KJ=IJ-I+K
      A(IJ) =HOLD*A(KJ) +A(IJ)
   65 CONTINUE
C     DIVIDE ROW BY PIVOT
      KJ=K-N
      DO 75 J=1,N
      KJ=KJ+N
      IF(J-K) 70,75,70
   70 A(KJ)=A(KJ)/BIGA
   75 CONTINUE
C     PRODUCT OF PIVOTS
      D=D*BIGA
C     REPLACE PIVOT BY RECIPROCAL
      A(KK )=1./BIGA
   80 CONTINUE
C     FINAL ROW AND COLUMN INTERCHANGE
      K=N
  100 K=(K-1)
      IF(K)150,150,105
  105 I=L(K)
      IF(I-K) 120,120,108
```

```
  108   JQ=N*(K-1)
        JR=N*(I-1)
        DO 110 J=1,N
        JK=JQ+J
        HOLD=A(JK)
        JI=JR+J
        A(JK)=-A(JI)
  110   A(JI) =HOLD
  120   J=M(K)
        IF(J-K) 100,100,125
  125   KI=K-N
        DO 130 I=1,N
        KI=KI+N
        HOLD=A(KI)
        JI=KI-K+J
        A(KI) =-A(JI)
  130   A(JI) =HOLD
        GO TO 100
  150   RETURN
        END
        FUNCTION SIMPSN(WHAT,XMIN,XMAX,N)
C         NUMERICAL INTEGRATION ROUTINE USING SIMPSONS RULE
        DX=(XMAX-XMIN)*.5/N
        X=XMIN+DX
        SUM=WHAT(XMIN)-WHAT(XMAX)
        DO 1 K=1,N
        SUM=SUM+4.*WHAT(X)+2.*WHAT(X+DX)
    1   X=DX*2.+X
        SIMPSN=DX*SUM/3.
        RETURN
        END
```

APPENDIX II. THERMOELECTRIC TUNNELING

A. Tunneling Hamiltonian

To calculate correctly the current through a superconducting tunnel junction, it is necessary to take account of the coherence factors which describe the quasiparticle wave functions. Barrier transmission probability amplitudes T_{kq} describe coupling between states with momenta k in one metal, and q in the other metal. For weak coupling through the oxide barrier, we can assume the familiar tunneling hamiltonian of the form

$$\mathcal{H}_T = \sum_{k,q} T_{kq}\, c_k^* c_q + T_{qk}^*\, c_q^* c_k \qquad (A.1)$$

where c_q annihilates an <u>electron</u> from the q side of the junction. The sum is taken over electron spins as well as momenta. The probability amplitudes T_{kq} will be seen to depend on the type of tunneling (electron-like or hole-like) in addition to the initial and final states, k and q.

The tunneling hamiltonian must be rewritten in terms of quasiparticle states in order to compute the allowed tunneling current in the superconducting case. Following the notation of Tinkham (1972)

$$\mathcal{H}_T = [T_{kq}(u_k \gamma^*_{ek0} + v_k \gamma_{hk1})(u_q \gamma_{eq0} + v_q \gamma^*_{hq1}) + T^*_{qk}(u_k \gamma_{ek0} + v_k \gamma^*_{hk1})(u_q \gamma^*_{eq0} + v_q \gamma_{hq1})] \quad (A.2)$$

The hamiltonian consists of eight terms, which fall into two categories. There are four terms involving one creation and one annihilation operator. These terms describe tunneling of quasiparticles from one side of the film to the other. The other four terms each have either two creation or two annihilation operators, and describe pair-breaking or pair-forming tunneling processes.

The effects of these terms are listed in table A.1. In describing the energies E_k and E_q, the excitation picture has been used, so that the energies are all expressed as positive numbers relative to the Fermi surface. Note that for a given energy E_k, tunneling will not necessarily be allowed in a given channel because of the existence of a gap in the density of states. (Tunneling is disallowed if $E_q < \Delta_q$.) Each tunneling term has been classified as electron-like (e), hole-like (h), or pair-breaking (pb). The sense of the voltage across the tunnel junction has been defined such that electrons gain energy in tunneling from the k-side film to the q-side film.

For simplicity we will restrict our attention to the case that $eV < (\Delta_k + \Delta_q)$. In this situation pair-breaking tunneling is

Term in $\mathcal{H}_T$		Probability Factor	E_q	Electron Transfer (k to q)	Type of Tunneling	Mean Electron Energy in the *oxide*
a	$T_{kq}u_k u_q \gamma^*_{ek0} \gamma_{eq0}$	$u_k^2 u_q^2 (1-f_k) f_q$	E_k+eV	-1	e	$E_k+(eV/2)$
b	$T^*_{qk}u_k u_q \gamma^*_{eq0} \gamma_{ek0}$	$u_k^2 u_q^2 f_k (1-f_q)$	E_k+eV	+1	e	$E_k+(eV/2)$
c	$T_{kq}v_k v_q \gamma_{hk1} \gamma^*_{hq1}$	$v_k^2 v_q^2 f_k (1-f_q)$	E_k-eV	-1	h	$-E_k+(eV/2)$
d	$T^*_{qk}v_k v_q \gamma_{hq1} \gamma^*_{hk1}$	$v_k^2 v_q^2 (1-f_k) f_q$	E_k-eV	+1	h	$-E_k+(eV/2)$
e	$T_{kq}v_k u_q \gamma_{hk1} \gamma_{eq0}$	$v_k^2 u_q^2 f_k f_q$	$-E_k+eV$	-1	pb	$-E_k+(eV/2)$
f	$T^*_{qk}v_k u_q \gamma^*_{eq0} \gamma^*_{hk1}$	$v_k^2 u_q^2 (1-f_k)(1-f_q)$	$-E_k+eV$	+1	pb	$-E_k+(eV/2)$
g	$T_{kq}u_k v_q \gamma^*_{ek0} \gamma^*_{hq1}$	$u_k^2 v_q^2 (1-f_k)(1-f_q)$	$-E_k-eV$	-1	pb	$E_k+(eV/2)$
h	$T^*_{qk}u_k v_q \gamma_{hq1} \gamma_{ek0}$	$u_k^2 v_q^2 f_k f_q$	$-E_k-eV$	+1	pb	$E_k+(eV/2)$

prohibitted by conservation of energy.

By Fermi's Golden Rule, the quasiparticle current is simply (Smith, 1975)

$$I_{qp} = 4\pi e/\hbar \sum \int_0^\infty dE \; |T_{kq}|^2 \{v_k^2 v_q^2 N_k(E)N_q(E+eV)[f_k(E)-f_q(e+eV)]$$

$$-u_k^2 u_q^2 N_k(E)N_q(E-eV)[f_k(E)-f_q(E-eV)]\} \quad (A.3)$$

The sum is over both excitation branches for both films (four terms). The sum over spins contributes a factor of 2, which has been incorporated into the equation. The terms involving $u_k^2 u_q^2$ describe the probability of tunneling of electron excitations from the k-side film to the q-side film, shown as A-type processes in Fig. 5.1. The $v_k^2 v_q^2$ terms involve transferring charge in the other direction (i.e. B-type hole tunneling).

B. Zero Voltage NS Tunneling

To further simplify the calculations, we will study the special case of zero-voltage current for a normal metal-insulator-superconductor (NS) tunnel junction (V=0 and Δ_q=0). Under these restrictions, Eq. (A.3) may be reduced by performing the sum over the electron and hole branches of the normal metal using the values:

$$\begin{aligned} u_q &= 0 && q < q_F \\ &= 1 && q > q_F \\ v_q &= 1 && q < q_F \\ &= 0 && q > q_F \end{aligned} \qquad \text{(A.4)}$$

Therefore

$$I_o^{NS} = 4\pi e/\hbar \sum \int_o^\infty dE \; (|T_{kq}|^2 v_k^2 - |T_{kq}|^2 u_k^2) N_k(E)[f_k(E)-f_q(E)] \qquad \text{(A.5)}$$

The sum now is only over the $k>k_F$ and $k<k_F$ branches of the superconductor. As was the case before, the u_k^2 terms describe tunneling from electron-like states in the superconductor, through the oxide, and into the normal metal with an energy E above the Fermi surface. For this electron tunneling it will be assumed that to lowest order in the energy (measured from the Fermi energy)

$$\left|\frac{T_{kq}}{T(0)}\right|^2 = 1 + c_1 E \qquad q > q_F \quad \text{(A.7)}$$

where T(0) is the tunneling probability amplitude at the Fermi surface. Similarly for hole tunneling (v_k^2 terms)

$$\left|\frac{T_{kq}}{T(0)}\right|^2 = 1 - c_1 E \qquad q < q_F \quad (A.8)$$

Substituting these values for T_{kq} into Eq. (A.5) yields

$$I_o^{NS} = (4\pi e/\hbar)\,|T(0)|^2 \sum \int_o^\infty dE\; c_1 E\; (v_k^2 + u_k^2) N_k(E)[f_k(E)-f_q(E)] \quad (A.9)$$

Using the identity ($v_k^2 + u_k^2 = 1$), we can eliminate the dependence on coherence factors in Eq. (A.9). The sum over the $k>k_F$ and $k<k_F$ branches then simply introduces a factor of two, leaving:

$$I_o^{NS} = 2\,[(4\pi e/\hbar)\,|T(0)|^2]\; c_1 \int_o^\infty dE\; E\; N_k(E)[f_k(E)-f_q(E)] \quad (A.10)$$

The factor $[(4\pi e/\hbar)\,|T(0)|^2]$ may be replaced by $(1/eR)$.

Several limiting cases of Eq. (A.10) are worthy of note. If both electrodes are at the same temperature, there will be no net current flow. On the other hand, if the q-side film is at zero temperature ($f_q = 0$), Eq. (A.10) reduces to the not too surprising result

$$I = (2/eR)\ c_1 \int_0^\infty dE\ E\ N_k(E)\ f_k(E) \qquad (A.11)$$

$$= (2/eR)\ c_1\ \Delta\ \langle E_k \rangle\ n_k \qquad (A.12)$$

where $\langle E_k \rangle$ is the average quasiparticle energy in the k-side film and n_k is the normalized quasiparticle density.

If the quasiparticle occupation of the k-side film is a Fermi-Dirac distribution with temperature T_k, and the q-side film has temperature T_q then the integral of (A.10) can be expressed as a sum of modified Bessel functions.

$$I_o^{NS} = (2/eR)c_1\Delta^2 \sum_{m=1} (-1)^{m+1}[K_o(m\Delta/kT_k)+(kT_k/m\Delta)K_1(m\Delta/kT_k)$$

$$-K_o(m\Delta/kT_q)-(kT_q/m\Delta)K_1(m\Delta/kT_q)] \qquad (A.13)$$

The series converges rapidly at low temperatures. The leading low temperature behavior is

$$I_o^{NS} \sim [(kT_k/\Delta)^{1/2} e^{-\Delta/kT_k} - (kT_q/\Delta)^{1/2} e^{-\Delta/kT_q}] \qquad (A.14)$$

C. SIS Tunneling

The more general case of tunneling between two superconductors can be calculated in a manner similar to that used to derive Eq. (A.10). Care should be taken to recognize the electron/hole dependence of T_{kq}. Denoting the two matrix elements as T^e_{kq} and T^h_{hk} respectively, Eq. (A.3) becomes

$$I_{qp} = 4\pi e/\hbar \sum \int_0^\infty dE \{ | T^h_{kq} |^2 v_k^2 v_q^2 N_k(E) N_q(E+eV)[f_k(E)-f_q(E+eV)]$$

$$- | T^e_{kq} |^2 u_k^2 u_q^2 N_k(E) N_q(E-eV)[f_k(E)-f_q(E-eV)]\} \quad (A.15)$$

Summing over the branches yields

$$I_{qp} = 4\pi e/\hbar \int_0^\infty dE \{ | T^h_{kq} |^2 N_k(E) N_q(E+eV)[f_k(E)-f_q(E+eV)]$$

$$- | T^e_{kq} |^2 N_k(E) N_q(E-eV)[f_k(E)-f_q(E-eV)]\} \quad (A.16)$$

Using the oxide electron energies given in the previous table, this can be approximated as

$$I_{qp} = (1/eR) \int_0^\infty dE\{[1+c_1(E+eV/2)]N_k(E) N_q(E+eV)[f_k(E)-f_q(E+eV)]$$

$$-[1-c_1(E-eV/2)]N_k(E) N_q(E-eV)[f_k(E)-f_q(E-eV)]\} \quad (A.17)$$

The eV/2 terms account for energy gain (or loss) of the electron as it traverses the oxide barrier in the presence of an electric field. Generally the thermoelectric constribution to the current is only slightly voltage dependent. The coefficient c_1 is only weakly voltage dependent (Gundlach, 1973) and can generally be treated as a constant for low voltages.

In all cases examined here, the basic temperature dependence is well described by the approximation made in Eq. (5.10).

REFERENCES

A. G. Aronov and B. Z. Spivak, Sov. J. Low Temp. Phys 4, 641 (1978).

O. P. Balkashin, I. K. Yanson, and A. V. Khotekevich, Fiz. Nizk. Temp. 5, 28 (1979) [Sov. J. Low Temp. Phys. 5, 12 (1979)].

S. Basavaiah, J. M. Eldridge, and J. Matisoo, J. Appl. Phys. 45, 457 (1974).

P. Bevington, Data Reduction and Error Analysis for the Physical Sciences, (McGraw-Hill, New York, 1969).

J. J. Chang and D. J. Scalapino, Phys. Rev. Lett. 37, 522 (1976).

J. J. Chang, Phys. Rev. Lett. 39, 1352 (1977).

J. J. Chang and D. J. Scalapino, J. Low Temp. Phys. 31, 1 (1978).

J. Clarke, B. R. Fjordbóge, and P. E. Lindelof, Phys. Rev. Lett. 43, 642 (1979).

J. Clarke and S. M. Freake, Phys. Rev. Lett. 29, 588 (1972).

J. Clarke and M. Tinkham, Phys. Rev. Lett. 44, 106 (1980).

R. C. Dynes, V. Narayanamurti, and J. P. Garno, Phys. Rev. Lett. 41, 1509 (1978).

W. Eisenmenger, K. Lassman, H. J. Trumpp, and R. Krauss, Appl. Phys. 12, 163 (1977).

H. Ekrut and A. Hahn, J. Appl. Phys. 51, 1686 (1980).

Yu M. Gal'perin, V. L. Gurevich, and V. I. Kozub, Zh. Eksp. Teor. Fiz. 60, 1387 (1974) [Sov. Phys.-JETP 39, 680 (1974)].

J. C. Garland and D. J. Van Harlingen, Phys. Lett. 47A, 423 (1974).

Yu. M. Gerbshtein, E. I. Nikulin, and B. Z. Spivak, Fiz. Tverd. Tela 20, 1067 (1978) [Sov. Phys. Solid State 20, 616 (1978)].

K. E. Gray and H. W. Willemsen, Bull. Am. Phys. Soc. 24, 328 (1979).

K. E. Gray and H. W. Willemsen, J. Phys. Colloq. 39, C6/513 (1979).

K. H. Gundlach, J. Appl. Phys. 44, 5005 (1973).

W. A. Harrison, Phys. Rev. 123, 85 (1961).

T. E. Hartman, J. Appl. Phys. 35, 3283 (1964).

D. F. Heidel and J. C. Garland, Bull. Am. Phys. Soc. 25, 411 (1980).

P. Hu, R. C. Dynes, and V. Narayanamurti, Phys. Rev. B 10, 2786 (1974).

S. B. Kaplan, J. Low Temp. Phys. 37, 343 (1979).

S. B. Kaplan, D. D. Chi, D. N. Langenberg, J. J. Chang, S. Jafarey, and D. J. Scalapino, Phys. Rev. B 14, 4854 (1976).

S. B. Kaplan, J. R. Kirtley, and D. N. Langenberg, Phys. Rev. Lett. 39, 291 (1977).

J. R. Kirtley, D. S. Kent, S. B. Kaplan, and D. N. Langenberg, J. Phys. Colloq. 39, C6/511 (1978).

M. K. Konkin and J. G. Adler, J. Appl. Phys. 50, 8125 (1979).

D. N. Langenberg, Proc. Low Temp. Phys. LT-14 5, 223, (North-Holland Publ. Co., Amsterdam, 1975).

D. N. Langenberg, in Feskorperprobleme XIV, 67, H. J. Queisser (ed.), (F. Vieweg and Sohn, Braunschwieg, Germany, 1974).

A. A. J. Matsinger, R. de Bruyn Ouboter, and H. van Beelen, Physica 93B, 63 (1978).

R. G. Melton, J. L. Paterson, and S. B. Kaplan, Phys. Rev. B 21, 1858 (1980).

C. S. Owen and D. J. Scalapino, Phys. Rev. Lett. 28, 1559 (1972).

W. H. Parker, Phys. Rev. B 12, 1667 (1975).

W. H. Parker and W. D. Williams, Phys. Rev. Lett. 29, 924 (1972).

W. H. Parker, Phys. Rev. B 12, 3667 (1975).

C. J. Pethick and H. Smith, Phys. Rev. Lett. 43, 640 (1979).

A. Rothwarf and B. N. Taylor, Phys. Rev. Lett. 19, 27 (1967).

A. Schmid and G. Schön, Phys. Rev. Lett. 43, 973 (1979).

I. K. Schuller and C. M. Falco, Fiz. Nizk. Temp.. 4, 939 (1978) [Sov. J.

Low Temp. Phys. 4, 446 (1978)].

A. D. Smith, W. J. Skocpol, and M. Tinkham, Phys. Rev. B 21, 3879 (1980).

L. N. Smith, Ph. D. thesis, unpublished (1975).

M. Tinkham, Phys. Rev. B 6, 1747 (1972).

D. J. Van Harlingen, Bull. Am. Phys. Soc. 25, 411 (1980).

D. J. Van Harlingen and J. C. Garland, Solid State Commun. 25, 419 (1978).

N. K. Welker and F. D. Bedard, in SQUID: Superconducting Quantum Interference Devices and Their Applications, H. D. Hahlbohm and H. Lübbig (eds.), (Walter de Gruyter, New York, 1977), 200.

H. W. Willemsen and K. E. Gray, Phys. Rev. Lett. 41, 812 (1978).

H. W. Willemsen and K. E. Gray, Bull. Am. Phys. Soc. 24, 329 (1979).

ACKNOWLEDGEMENTS

It is a pleasure to thank Profs. M. Tinkham and W. Skocpol for their support and encouragement throughout the course of these experiments. Their criticisms and suggestions during manuscript preparation have been both incisive and numerous. Discussions with Drs. T. Klapwijk and L. Smith were invaluable in separating wheat from chaff in theoretical models to explain observations.

I am grateful to the Gordon McKay graduate students and staff without whose technical and moral support this project would have been impossible. G. Blonder and D. Frank deserve credit for construction of the data acquisition computer. I would also like to thank L. DeFeo, whose ability to build the experimental equipment far exceeded my ability to draw it.

This work was supported in part by the National Science Foundation and the Joint Services Electronics Program.

[illegible] DISTRIBUTION LIST

[illegible]

DEPARTMENT OF DEFENSE

Director
National Security Agency
ATTN: Dr. T. J. Beahn, R-5
Fort George G. Meade, MD 20755

Defense Documentation Center (12 copies)
ATTN: DDC-TCA
Cameron Station
Alexandria, VA 22314

Dr. George Gamota
Assistant for Research
Deputy Under Secretary of Defense for Research
and Engineering (Research & Advanced Technology)
Room 3E1067, The Pentagon
Washington, DC 20301

Defense Advanced Research Projects Agency
ATTN: Dir. R. Reynolds
1400 Wilson Boulevard
Arlington, VA 22209

DEPARTMENT OF THE ARMY

Commander
US Army Armament R&D Command
ATTN: DRDAR-SC
Dover, NJ 07801

Commander
US Army Ballistic Research Laboratory
ATTN: DRDAR-BAD
Aberdeen Proving Ground
Aberdeen, MD 21005

Commander
US Army Communication Command
ATTN: CC-OPS-PT
Fort Huachuca, AZ 85613

Commander
US Army Natick Research and Development Center
ATTN: Tech. Applied Sciences Division
Natick, MA 01760

Commander
US Army Material Development
and Readiness Command
ATTN: Technical Library, Dr. [illegible]
5001 Eisenhower Avenue
Alexandria, VA 22333

Commander
US Army Missile R&D Command
ATTN: Chief, Development Section
Redstone Arsenal, AL 35809

Commander
US Army Satellite Communications Agency
Fort Monmouth, NJ 07703

Commander
US Army Electronics, Technology Laboratory
ATTN: DELSD-L (Tech Reports Lib.)
White Sands Missile Range, NM 88002

Commander
US Army Communications R&D Command
ATTN: DRDCO-COM-RN (Dr. John Pasier)
Fort Monmouth, NJ 07703

Director
TRADOC
ATTN: TT-AD (Mrs. Bailey)
Fort Monmouth, NJ 07703

Commander
US Army Electronics R&D Command
Night Vision & Electro-Optics Lab
ATTN: DELEV (Dr. Rudolf G. Buser)
Fort Belvoir, VA 22060

Director
US Army Electronics R&D Command
ATTN: DELEW-D (Electronic Warfare Laboratory)
White Sands Missile Range, NM 88002

Executive Secretary, ECAC, FASP
US Army Research Office
P. O. Box 12211
Research Triangle Park, NC 27709

Commander
Harry Diamond Laboratories
ATTN: Dr. John E. Rosenthal
2800 Powder Mill Road
Adelphi, MD 20783

AMSA (DAMA-ARS-D)
Washington, DC 20310

Director
US Army Electronics Technology & Devices Lab
(ERADCOM)
ATTN: DELET-DT (Dr. [illegible])
Fort Monmouth, NJ 07703

Director
US Army Electronics Technology & Devices Lab
(ERADCOM)
ATTN: DELET-DS (Dr. E. Sternheim)
Fort Monmouth, NJ 07703

Director
US Army Electronics R&D Command
Night Vision & Electro-Optics Lab
ATTN: DR. Ray Bellcoran
Fort Belvoir, VA 22060

Commander
US Army Research Office
ATTN: DRXRO-PH (Dr. Paul Boggs)
P. O. Box 12211
Research Triangle Park, NC 27709

Commander
US Army Missile R&D Command
Research Directorate
ATTN: AMSMI-RRR (Dr. Charles Bowman)
Redstone Arsenal, AL 35809

Commander
US Army Missile R&D Command
Advanced Concepts Technology
ATTN: DRDMI-TEM (Dr. Jon Bridges)
Redstone Arsenal, AL 35809

Librarian
US Army Electronics R&D Command
Night Vision & Electro-Optics Lab
ATTN: DR. Judy Tedoro
Fort Belvoir, VA 22060

Director
US Army Electronics R&D Command
Night Vision & Electro-Optics Lab
ATTN: Dr. William Daly
Fort Belvoir, VA 22060

Commander
US Army Missile R&D Command
Physical Sciences Directorate
ATTN: DRDMI-TEM (Dr. Michael S. Fahey)
Redstone Arsenal, AL 35809

Commander
US Army Missile R&D Command
Physical Research Intelligence
ATTN: DRDMI-TBD (Dr. William J. Gamble)
Redstone Arsenal, AL 35809

Commander
White Sands Missile Range
ATTN: STEWA-TD-RB (Dr. Al L. Gilbert)
White Sands Missile Range, NM 88002

Commander
US Army Communications R&D Command
ATTN: DRDCO-PCS-RB (Dr. David Reese)
Fort Monmouth, NJ 07703

Director
US Army Communications R&D Command
ATTN: DRDCO-TCD-RM (Dr. A. A. Sobinski)
Fort Monmouth, NJ 07703

Commander
US Army Communications R&D Command
ATTN: DRDCO-PCS-RA (Dr. F. Blankenship)
Fort Monmouth, NJ 07703

Director
US Army Electronics Technology and Devices Lab
ATTN: DELET-DD (Dr. J. Pinkerton)
Fort Monmouth, NJ 07703

Commander
US Army Electronics R&D Command
ATTN: DELET-DR (Dr. H. Bennett)
Fort Monmouth, NJ 07703

Director
US Army Electronics Technology and Devices Lab
ATTN: DELET-DI (Dr. E. Belohoubek)
Fort Monmouth, NJ 07703

Commander
US Army Electronics R&D Command
ATTN: DRDEL-CG (Dr. John Pellegrini)
Fort Monmouth, NJ 07703

Director
US Army Electronics R&D Command
Night Vision & Electro-Optics Lab
ATTN: DELEV-D (Dr. Paul Kruse)
Fort Belvoir, VA 22060

Commander
US Army Research Office
ATTN: DRXRO-IP (Dr. William E. Mendrin)
P. O. Box 12211
Research Triangle Park, NC 27709

Director
Division of Neurology Physiology
Walter Reed Army Institute of Research
Washington, DC 20012

Commander
AMC Headquarters
ATTN: DRCDMA-ST (Dr. M. Stroman)
Dover, NJ 07801

Director
US Army Signals Warfare Lab
ATTN: DELSW-D
Vint Hill Farms Station
Warrenton, VA 22186

Director
US Army Electronics Technology & Devices Lab
ATTN: DELET-DC (Dr. F. Bertrand)
Fort Monmouth, NJ 07703

Director
US Army Electronics Technology & Devices Lab
ATTN: DELET-DQ (Dr. J. Carroll)
Fort Monmouth, NJ 07703

U.S. Army Research Office - Durham
ATTN: Library
P. O. Box 12211
Research Triangle Park, NC 27709

Commander
U.S. Army Communications R&D Command
ATTN: DRDCO-COM-RN (Mr. [illegible])
Fort Monmouth, NJ 07703

Mr. Sidney Soo
Bld. 315 Picatinny
Dover, NJ 07801

DEPARTMENT OF THE AIR FORCE

Mr. Robert Barrett
AFAL/DT
Wright-Patterson AFB, OH 45433

Dr. Art E. Bond
AFML (ASD)
Wright-Patterson AFB, OH 45433

Dr. R. Thorpington
AFAL/TA
Wright-Patterson AFB, OH 45433

Dr. R. D. Brown
RADC/ESR
Hanscom AFB, MA 01731

Mr. W. Edwards
AFAL/DH
Wright-Patterson AFB, OH 45433

Professor W. E. Portnoy
Head Dept. of Electrical Eng
AFIT EN
Wright-Patterson AFB, OH 45433

Dr. Alan Jacobsohn
AFAL/PO
Wright-Patterson AFB, OH 45433

Major Engineer, Office of Aerospace Research & Development
ATTN: Captain A. P. Nordquist
Bld. 410, POI, Wpn. Lab. (NTD)
Kirtland AFB, NM 87117

Mr. Harry Fassnacht (TSTB)
Rome Air Development Center
Griffiss AFB, NY 13441

Lt. R. P. Young
Air Force Member, DCC
Air Force Office of Scientific Research
(AFSC) AFO 757
Holloman Air Force Base, NM 88330

Chief, Electronic Research Branch
AFAL, WP
Wright-Patterson AFB, OH 45433

Lt. Edward Kiersten
Code 7702
Dept. of AFR, NM 87117

Mr. John Hall, Chief (TSTP)
HQ ESC (AF)
Hanscom AFB, MA 01731

Dr. Richard Durbeck
RADC/ETSL
Hanscom AFB, MA 01731

Dr. J. Bajus
Chief Scientist
AFAL/A
Wright-Patterson AFB, OH 45433

Dr. Allen Schell
AFIT EN
Hanscom AFB, MA 01731

Rome Air Development Center
Griffiss AFB, NY 13441

Lt. Howard Schrumpf
Air Force Office of Scientific Research
Bolling Air Force Base, DC 20332

Lt. Col. Robert Mikkola
Air Force Office of Scientific Research
(AFSC) AFOSR/NP
Bolling Air Force Base, DC 20332

Major Clarence A. Rappleye
Air Force Office of Scientific Research
(AFSC) AFOSR/NE
Bolling Air Force Base, DC 20332

DEPARTMENT OF THE NAVY

Office of Naval Research
800 North Quincy Street
Arlington, VA 22217
Attn: Code 427
427
427

Commanding Officer
Naval Research Laboratory
Washington, DC 20375
ATTN: Code 1409 - Dr. A. Brodzinski
5227 - Mr. H. Pusey
5227 - Dr. A. Brodzinski
5227 - Mr. W. B. Jones
5227 - Mr. J. C. Marsden
5227 - Mr. J. L. Davis
5227 - Mr. J. D. Davis
5227 - Mr. J. C. Fraser
5227 - Mr. E. Foster
5227 - Mr. J. L. Hook

Director
Office of Naval Research Area 5 Office
495 Summer Street
Boston, MA 02210

Director
Office of Naval Research
New York Area Office
715 Broadway, 5th Floor
New York, NY 10003

Director
Office of Naval Research Branch Office
536 South Clark Street
Chicago, IL 60605

Director
Office of Naval Research Branch Office
1030 East Green Street
Pasadena, CA 91106

Naval Surface Weapons Center
ATTN: Technical Library
Code CX-21
Dahlgren, VA 22448

Dr. J. M. Hills, Jr.
Naval Surface Weapons Center
Code DF
Dahlgren, VA 22448

Naval Air Development Center
Warminster, PA 18974
ATTN: Code 301 - Dr. [illegible]
Dr. Frederick Lofsky

Dr. Arthur W. R. Goldstein
Code 1021P
Naval Oceanography
U.S. Naval Observatory
Mass. Avenue at 34th Street, NW
Washington, DC 20390

Dr. Gerald J. Iafrate
Electronics Technology Division
Electronics Technology & Devices Laboratory
ATTN: DELET-DE
Fort Monmouth, NJ 07703

Dr. Arthur Lind
Office of Research Development, Test & Evaluation
OP-987
The Pentagon, Room 5D760
Washington, DC 20350

Dr. A. L. Slafkosky
Code RD-1
Headquarters, U.S. Marine Corps
Washington, DC 20380

Dr. A. J. Mueller
Naval Air Systems Command
AIR-310
Washington, DC 20361

Mr. Warren D. Peterson
Naval Electronics Systems Command
Code 0-28
NC #1
2511 Jefferson Davis Hwy
Arlington, VA 20360

Naval Sea Systems Command
NC #3
2531 Jefferson Davis Hwy
Washington, DC 20362
ATTN: Code 03A - J. W. Burn

David Taylor Naval Ship Research & Development Center
Bethesda, MD 20084
ATTN: Code 5211 - Technical Library
Code 18 - W. M. Ingebretsen

Naval Surface Weapons Center
White Oak
Silver Spring, MD 20910
ATTN: Codes WX-21, Technical Library
WX-43, R. C. Allen

Dr. Edward C. Eby
Code 3210
Naval Underwater Systems Center
New London Laboratory
New London, CT 06320

Dr. Martin Goldshlager
Code 36
Naval Underwater Systems Center
New London Laboratory
New London, CT 06320

Dr. J. F. Draus
Code 36
Naval Underwater Systems Center
New London Laboratory
New London, CT 06320

OTHER GOVERNMENT AGENCIES

Dr. Herbert J. Bennett
Director
Division of Materials Research
National Science Foundation
1800 G Street
Washington, DC 20550

Dr. Jay Harris
Program Director
Devices and Waves Program
National Science Foundation
1800 G Street
Washington, DC 20550

Los Alamos Scientific Laboratory
ATTN: Main Library
P. O. Box 1663
Los Alamos, NM 87545

Dr. Leon Goldstein
Program Director, Solid-State Physics
Division of Materials Research
National Science Foundation
1800 G Street
Washington, DC 20550

R. Jane Thurston
Deputy Director Institute for
Computer Sciences & Technology
National Bureau of Standards
Washington, DC 20234

Chief, Electronic Sciences & Analysis Section
National Science Foundation
1800 G Street, NW
Washington, DC 20550

Deputy Director for Research
Research and Technology Division
Office of Aeronautics and Space Tech
NASA
Washington, DC 20546

Lawton J. Prysock, Director
Center for Electronics and Electrical Engineering
A361 Technology Bldg
National Bureau of Standards
Washington, DC 20234

Dr. Ken Galil
Chief, Research & Detection
Electronics Division, Code 5E
NASA HQ
Mail Stop 5E
600 Independence Avenue, SW
Washington, DC 20546

Mr. Herbert Zeiner
Manager, Data Management Program, Code 621-3
NASA HQ
600 Independence Avenue, SW
Washington, DC 20546

Mr. John Lee
Assistant Chief, Information Processing Division
Code 500
Goddard Space Flight Center
Greenbelt, MD 20771

Dr. Charles Knight
Aerospace Technologist
Langley Research Center
Langley Station
Hampton, VA 23665

Mr. John Gould
Chief, Design Technologies Branch
George C. Marshall Space Flight Center
National Space Flight Center, AL 35812

NON-GOVERNMENT AGENCIES

Director
Columbia Radiation Laboratory
Columbia University
538 West 120th Street
New York, NY 10027

Director
Coordinated Science Laboratory
University of Illinois
Urbana, IL 61801

Director
Division of Applied Sciences
Harvard University
Pierce Hall
Cambridge, MA 02138

Director
Electronics Research Center
The University of Texas
P. O. Box 7728
Austin, TX 78712

Director
Electronics Research Laboratory
University of California
Berkeley, CA 94720

Director
Electronics Sciences Laboratory
University of Southern California
Los Angeles, CA 90007

Director
Microwave Research Institute
Polytechnic Institute of New York
333 Jay Street
Brooklyn, NY 11201

Director
Research Laboratory of Electronics
Massachusetts Institute of Technology
Cambridge, MA 02139

Director
Stanford Electronics Laboratory
Stanford University
Stanford, CA 94305

Director
Edward L. Ginzton Laboratory
Stanford University
Stanford, CA 94305

Dr. Lester Eastman
School of Electrical Engineering
Cornell University
118 Phillips Hall
Ithaca, NY 14851

Dr. Carlton Walter
Electrodynamics Laboratory
The Ohio State University
[illegible], OH 43212

Dr. Richard Sorbo
Department of Electrical Engineering
Texas Tech University
Lubbock, TX 79409

Dr. Roy Gould
Theoretical Phys - Int Applied Physics
California Institute of Technology
Pasadena, CA 91125

Director
School of Electrical Engineering
Georgia Institute of Technology
Atlanta, GA 30332

Prof. J. F. Gaitng
Department of Electrical Engineering
Texas Tech University
Lubbock, TX 79409

DISTRIBUTION LIST FOR ONR ELECTRONIC AND SOLID STATE SCIENCES

Director
Advanced Research Projects Agency
Attn: Technical Library
1400 Wilson Boulevard
Arlington, Virginia 22209

Office of Naval Research
Electronics Program Office (Code 427)
800 North Quincy Street
Arlington, Virginia 22217

Office of Naval Research
Code 105
800 North Quincy Street
Arlington, Virginia 22217

Director
Naval Research Laboratory
4555 Overlook Avenua, S.W.
Washington, D.C. 20375
Attn: Technical Library (6 cps)
Code 5200 (1 copy)
5210 (1 copy)
5270 (1 copy)
6400 (1 copy)

Office of the Director of Defense
Research and Engineering
Office of the Assistant Director
Electronics & Physical Sciences
The Pentagon, Room 3D1079
Washington, DC 20301

Defense Documentation Center (12 cps)
Cameron Station
Alexandria, Virginia 22314

Commanding Officer
Office of Naval Research Branch Office
536 South Clark Street
Chicago, Illinois 60605

San Francisco Area Office
Office of Naval Research
50 Fell Street
San Francisco, California 94102

Commanding Officer
Office of Naval Research Branch Office
1030 East Green Street
Pasadena, California 91101

Commanding Officer
Office of Naval Research Branch Office
495 Summer Street
Boston, Massachusetts 02210

New York Area Office
Office of Naval Research
115 Broadway 5th Floor
New York, New York 10003

ODDR&E Advisory Group on Electron Devices
201 Varick Street
New York, New York 10014

Naval Air Development Center
Attn: Technical Library
Johnsville
Warminster, Pennsylvania 18974

Naval Weapons Center
China Lake, California 93555
Attn: Technical Library (1 copy)
Code 6010 (1 copy)

Naval Research Laboratory
Underwater Sound Reference Division
Technical Library
P.O. Box 8337
Orlando, Florida 32806

Navy Underwater Sound Laboratory
Technical Library
Fort Trumbull
New London, Connecticut 06320

Commandant, Marine Corps
Scientific Advisor (Code AX)
Washington, D.C. 20380

Naval Ordnance Station
Technical Library
Indian Head, Maryland 20640

Naval Postgraduate School
Monterey, California 93940
Attn: Technical Library (1 copy)
Elect. Engin. Depart. (1 copy)

Naval Missile Center
Technical Library (Code 5632.2)
Point Mugu, California 93010

Naval Electronics Laboratory Center
San Diego, California
Attn: Technical Library (1 copy)
Code 2300 (1 copy)
2600 (1 copy)
4800 (1 copy)

Naval Undersea Center
Technical Library
San Diego, California 92132

Naval Weapons Laboratory
Technical Library
Dahlgren, Virginia 22448

Naval Ship Research and Development Center
Central Library (Codes L42 and L43)
Washington, D.C. 20007

Naval Surface Weapons Center
White Oak Laboratory
Silver Spring, Maryland 20910
Attn: Technical Library (1 copy)
Code 200 (1 copy)
212 (1 copy)

Deputy Chief of Naval Operations
(Development)
Technical Analysis and Advisory Group
(Code NOP-077D)
Washington, D.C. 20350

Commander
Naval Air Systems Command
Washington, D.C.
ATTN: Code 310 (1 copy)
360 (1 copy)

Commander
Naval Electronics Systems Command
Washington, D.C. 20360
Attn: Code 304 (1 copy)
310 (1 copy)

Commander
Naval Sea Systems Command
Washington, D.C. 20360

Naval Surface Weapons Center
Attn: Library
Dahlgren, Virginia 22448

Air Force Office of Scientific Research
Attn: Electronic and Solid State
Sciences Division
Department of the Air Force
Washington, D.C. 20333

Air Force Weapon Laboratory
Technical Library
Kirtland Air Force Base
Albuquerque, New Mexico 87117

Air Force Avionics Laboratory
Air Force Systems Command
Technical Library
Wright-Patterson Air Force Base
Dayton, Ohio 45433

Air Force Cambridge Research Laboratory
L.G. Hanscom Field
Technical Library
Cambridge, Massachusetts 02138

Harry Diamond Laboratories
Technical Library
Connecticut Avenue at Van Ness, N.W.
Washington, D.C. 20438

U.S. Army Research Office
Box CM, Duke Station
Durham, North Carolina 27706

Director
U.S. Army Engineering Research
and Development Laboratories
Fort Belvoir, Virginia 22060
Attn: Technical Documents Center

Director National Bureau of Standards
Attn: Technical Library
Washington, D.C. 20234

Naval Research Laboratory
4555 Overlook Avenue, S.W.
Washington, D.C. 20375
Attn: Code 5300 (1 copy)
7100 (1 copy)
7900 (1 copy)

Naval Electronics Laboratory Center
San Diego, California 92152
Attn: Code 2100 (1 copy)
2200 (1 copy)

C.C. Klick
Superintendent
Materials Sciences Division
Naval Research Laboratory
4555 Overlook Avenue, S.W.
Washington, D.C. 20375

Naval Research Laboratory
4555 Oberlook Avenue, S.W.
Washington, D.C. 20375
Attn: Code 5220 (1 copy)
5230 (1 copy)
5250 (1 copy)
5260 (1 copy)
5270 (1 copy)
5500 (1 copy)

Naval Electronics Laboratory Center
San Diego, California 92152
Attn: Code 2500 (1 copy)
4000 (1 copy)

Office of Naval Research (2 cps)
800 N. Quincy Street
Arlington, Virginia 22217
Attn: Code 430 (2 copies)

Naval Research Laboratory
4555 Overlook Avenue, S.W.
Washington, D.C. 20375
Attn: Code 5400

Naval Electronics Laboratory Center
San Diego, California 92152
Attn: Code 3000 (1 copy)
5000 (1 copy)
5600 (1 copy)

Air Force Office of Scientific Research
Mathematical and Information Sciences
Directorate
1400 Wilson Blvd.
Washington, D.C. 20333